CORA Cork Open Research Archive
Cartlann Taighde Oscailte Chorcaí

Title	Site-controlled quantum dots as sources of quantum light
Authors	Moroni, Stefano T.
Publication date	2018
Original Citation	Moroni, S. 2018. Site-controlled quantum dots as sources of quantum light. PhD Thesis, University College Cork.
Type of publication	Doctoral thesis
Rights	© 2018, Stefano Moroni. - http://creativecommons.org/licenses/by-nc-nd/3.0/
Download date	2026-11-15 13:32:46
Item downloaded from	https://hdl.handle.net/10468/7389

UCC
University College Cork, Ireland
Coláiste na hOllscoile Corcaigh

SITE-CONTROLLED QUANTUM DOTS AS SOURCES OF QUANTUM LIGHT

BY

STEFANO MORONI

A THESIS SUBMITTED TO
THE NATIONAL UNIVERSITY OF IRELAND, CORK
FOR THE DEGREE OF

DOCTOR OF PHILOSOPHY

EPITAXY AND PHYSICS OF NANOSTRUCTURES GROUP
TYNDALL NATIONAL INSTITUTE, DEPARTMENT OF PHYSICS
NATIONAL UNIVERSITY OF IRELAND, CORK
IRELAND



ucc
Coláiste na hOllscoile Corcaigh, Éire
University College Cork, Ireland

OCTOBER 2018
RESEARCH SUPERVISOR: Dr. EMANUELE PELUCCHI
HEAD OF THE DEPARTMENT: PROF. JOHN McINERNEY

Contents

Declaration v

Publication list vi

Abstract xi

Chapter 1 Introduction 1

1.1. Photonic qubits and quantum computation 1

1.2. Single-photon sources 6

1.3. Indistinguishable photons 8

1.4. Entangled photons 10

1.5. Sources of quantum light 11

1.5.1. Single atoms 13

1.5.2. Spontaneous parametric down conversion (SPDC) 14

1.5.3. Nitrogen-vacancies 15

1.6. Semiconductor quantum dots 17

1.6.1. Fine structure in a quantum dot and entangled photon emission 18

1.6.2. QD systems and achievements 21

1.6.3. Pyramidal quantum dots and thesis outline 24

Chapter 2 Pyramidal quantum dot fabrication and experimental techniques 33

2.1 Substrate preparation-patterning 34

2.2 MOVPE deposition 36

2.3 Bonding techniques 39

2.1.1. Au-AuSn-Au reflow bonding 40
2.1.2. SU8 bonding 41
2.4 Mechanical thinning and back-etching 41
2.5 LED fabrication 42
2.6 Lift-off techniques for Pyramidal Quantum Dots 44
2.7 Cryogenic MicroPL measurements 44
2.8 Correlating system 46
Chapter 3 Indium segregation during III-V quantum wire and quantum dot formation on patterned substrates 49
3.1 Introduction 51
3.2 Theory 52
3.3 Experiment 56
3.4 Results and discussion 58
3.4.1. Determination of kinetic parameters 58
3.4.2. LQWRs and pyramidal QDs 61
3.5 Morphology of pyramidal recesses 66
3.6 Conclusions 69
Chapter 4 Selective carrier injection into patterned arrays of pyramidal quantum dots for entangled photon light-emitting diodes 75
4.1 Introduction 77
4.2 Pyramidal quantum dot system 78
4.3 Selective current injection 80
4.4 Electroluminescence 82

4.5 Polarization-entangled photon emission 85

4.6 Conclusions and outlook 88

4.7 Supplementary Material 90

4.7.1. Sample growth and structure 90

4.7.2. Micro-LED fabrication 93

4.7.3. Measurements 94

4.7.4. Fidelity and Bell parameters calculation 96

4.7.5. Current density simulations 97

Chapter 5 On-demand single-photons from electrically-injected site-controlled Pyramidal Quantum Dots 103

5.1. Introduction 104

5.2. Fabrication and characterization methods 105

5.3. Results and discussion 107

5.4. Conclusion 111

5.5. Supplementary material: Sample structure 112

Chapter 6 Statistical study of stacked/coupled site-controlled pyramidal quantum dots and their excitonic properties 119

Supplementary material 130

Chapter 7 Vanishing biexciton binding energy from stacked, MOVPE grown, site-controlled pyramidal quantum dots for twin photon generation 137

7.1. Introduction 138

7.2. Experimental 140

7.3. Results and discussion 141

Supplementary material 146

Chapter 8 On the tuning of the optical properties and integration of pyramidal quantum dots 153

8.1. Application of piezoelectric stress to PQDs 153

8.1.1 Fabrication of piezoelectric tunable PQDs 154

8.1.2 Tuning of the emission of PQDs 155

8.2. Manipulation and integration of PQDs by “lift-off” 157

Conclusion and outlook 163

Acknowledgements 167

Declaration

This dissertation is the result of work carried out in the Epitaxy and Physics of Nanostructures Group at Tyndall National Institute from January 2015 to October 2018.

Except where otherwise stated this dissertation is the result of my own work and is not substantially the same as any I have already submitted, or that I am in the process of submitting, for any degree either at University College Cork or elsewhere.

Stefano Moroni

Tyndall National Institute,

University College of Cork,

October 2018

Publication list

Publications and proceedings

1. G. Juska, E. Murray, V. Dimastrodonato, T. H. Chung, S. T. Moroni, A. Gocalinska, and E. Pelucchi, “Conditions for entangled photon emission from (111)B site-controlled pyramidal quantum dots,” J. Appl. Phys., vol. 117, no. 13, 2015.

2. S. T. Moroni, V. Dimastrodonato, T. H. Chung, G. Juska, A. Gocalinska, D. D. Vvedensky, and E. Pelucchi, “Indium segregation during III-V quantum wire and quantum dot formation on patterned substrates,” J. Appl. Phys., vol. 117, no. 16, 2015.

3. D. V. Lebedev, A. M. Mintairov, M. M. Kulagina, S. I. Troshkov, J. Kapaldo, J. L. Merz, S Rouvimov, G. Juska, A. Gocalinska, S. T. Moroni and E. Pelucchi, “Lasing of InP/AlInAs quantum dots in AlInAs microdisk cavity”, Journal of Physics: Conference Series 690, 012023 (2016).

4. T. H. Chung, G. Juska, S. T. Moroni, A. Pescaglini, A. Gocalinska, and E. Pelucchi, “Selective carrier injection into patterned arrays of pyramidal quantum dots for entangled photon light-emitting diodes,” Nat. Photonics, vol. 10, no. 12, pp. 782–787, Oct. 2016.

5. Küster, C. Heyn, A. Ungeheuer, G. Juska, S. T. Moroni, E. Pelucchi, and W. Hansen, “Droplet etching of deep nanoholes for filling with self-aligned complex quantum structures,” Nanoscale Res. Lett., vol. 11, 2016.

6. E. E. Mura, A. Gocalinska, G. Juska, S. T. Moroni, A. Pescaglini, and E. Pelucchi, “Tuning InP self-assembled quantum structures to telecom wavelength: A versatile original InP(As) nanostructure ‘workshop,’” Appl. Phys. Lett., vol. 110, no. 11, p. 113101, Mar. 2017.

7. D. V. Lebedev, M. M. Kulagina, S. I. Troshkov, A. S. Vlasov, V. Y. Davydov, A. N. Smirnov, A. A. Bogdanov, J. L. Merz, J. Kapaldo, A. Gocalinska, G. Juska, S. T. Moroni, E. Pelucchi, D. Barettin, S. Rouvimov, and A. M. Mintairov, “Excitonic

lasing of strain-free InP(As) quantum dots in AlInAs microdisk," Appl. Phys. Lett., vol. 110, no. 12, p. 121101, Mar. 2017.

8. S. T. Moroni, T. H. Chung, G. Juska, A. Gocalinska, and E. Pelucchi, "Statistical study of stacked/coupled site-controlled pyramidal quantum dots and their excitonic properties," Appl. Phys. Lett., vol. 111, no. 8, p. 083103, Aug. 2017.

9. E. Pelucchi, S. T. Moroni (corresp. auth.), V. Dimastrodonato, and D. D. Vvedensky, "Self-ordered nanostructures on patterned substrates," J. Mater. Sci. Mater. Electron., Oct. 2017.

10. S. T. Moroni, S. Varo, G. Juska, T. H. Chung, A. Gocalinska, and E. Pelucchi, "Vanishing biexciton binding energy from stacked, MOVPE grown, site-controlled pyramidal quantum dots for twin photon generation", J. Cryst. Growth, vol. 506, pp. 36–39, Jan. 2019.

11. S. T. Moroni, T. H. Chung, G. Juska, A. Gocalinska, and E. Pelucchi, "On-demand single-photons from electrically-injected site-controlled Pyramidal Quantum Dots", submitted to Journal of Physics D: Applied Physics. Oct. 2018

Conferences (poster/oral presentation)

1. S. T. Moroni, V. Dimastrodonato, T. H. Chung, G. Juska, A. Gocalinska, D. D. Vvedensky, and E. Pelucchi, EWMOVPE 2015, June 7-10 2015,Lund, Sweden.

2. S. T. Moroni, V. Dimastrodonato, T. H. Chung, G. Juska, D. Vvedensky and E. Pelucchi, Photonics Ireland 2015 Cork, 2-4 September 2015.

3. S. T. Moroni (oral, presenting author), T. H. Chung, G. Juska, A. Pescaglini, A. Gocalinska and E. Pelucchi (invited talk), 3rd International Workshop on "Engineering of Quantum Emitter Properties, Johannes Kepler University Linz, 17-18 December 2015.

4. S. T. Moroni, V. Dimastrodonato, T. H. Chung, G. Juska, A. Gocalinska, D. Vvedensky, and E. Pelucchi, Compound Semiconductor Week 2016, June 26-30, 2016, Toyama International Conference Center, Toyama, Japan.

5. S. T. Moroni (oral), V. Dimastrodonato, T.-H. Chung , G. Juska , A. Gocalinska , D. Vvedensky and E. Pelucchi, 18th International Conference on Metal Organic Vapor Phase Epitaxy, July 10-15, 2016, Sheraton San Diego Hotel & Marina San Diego, California, USA.

6. S. T. Moroni (invited talk), "Entangled Photons Diodes", Shortcuts to Adiabaticity 2016 in Cork, Monday 25th and Tuesday 26th July 2016, University College Cork, Kane Building, Cork.

7. S. T. Moroni (oral), G. Juska , T. H. Chung, J. Martín-Sánchez, R. Trotta , A. Rastelli, A. Gocalinska and E. Pelucchi, Compound Semiconductor Week 2017 May 14–18, 2017 Berlin, Germany. Best student paper award

8. S. T. Moroni (oral), T. H. Chung, G. Juska, A. Pescaglini, A. Gocalinska and E. Pelucchi, “A site-controlled quantum dot entangled-light-emitting diode” Photonics Ireland 2017, Radisson Blu Hotel, Galway, September 13 – 15th 2017, Ireland.

9. S. T. Moroni (oral), T. H. Chung, G. Juska, A. Gocalinska, R. Trotta, J. Martín-Sánchez, A. Rastelli and E. Pelucchi, Quantum Dot Day 2018, 24th January 2018, Sheffield

10. S. T. Moroni (oral), G. Juska, S. Varo, T.H. Chung, A. Gocalinska, R. Trotta, J. Martín-Sánchez (Spain),H. Huang, A. Rastelli, E. Pelucchi, “A unique tuneable, scalable and easily integrable source of quantum light based on pyramidal quantum dots” ICPS 2018 - 34th International conference on the physics of semiconductors - Montpellier, on July 29 to August 3, 2018.

A mamma e papà.

Abstract

Quantum information is at its infancy. Though several different approaches are being pursued, the ability of manipulating a quantum state and make two quantum systems interact in a controlled way is still a great challenge, especially in terms of reproducibility and fidelity to the expected theoretical state. Among the possible implementations of quantum information, photonics seems to offer many technological advantages, the biggest challenge being the availability of a pure, scalable and integrable source of photons with all the required properties.

Epitaxial semiconductor quantum dots (QDs) have been exploited to deliver such quantum light, e.g. indistinguishable single-photons and polarization-entangled photon pairs, by both optical and electrical injection, generated on demand. However, conventional self-assembled QDs are necessarily characterized by random positioning and randomly distributed optical properties, which limit the feasibility of a technology based on this kind of system.

In this context, pyramidal quantum dots (PQDs) are one very valid alternative to conventional semiconductor QD-based quantum light sources. In fact, the precise control over the position of the PQDs, together with the uniformity of properties granted by the combination of lithographic methods and metalorganic vapor-phase epitaxy (MOVPE), make this source one of the few scalable systems which have been proven in recent years to emit photons with very interesting properties, polarization-entangled photons, for instance, upon optical excitation.

In this work, all the main relevant aspects regarding PQDs are addressed through the most recent results obtained studying the system, starting from fundamental aspects regarding the epitaxy step. A growth model is presented which was also employed in the past as a practical tool to predict the result of the MOVPE in terms of geometry and composition of AlGaAs and GaAs structures inside a pyramidal recess. Here the model is extended in its simulation capabilities in order to include also the epitaxy of InGaAs, the actual material of which the optically active QD layer is made. This is then employed to simulate and understand the physical reason for a previously observed experimental behavior, henceforth confirming the applicability of the extended model to the simulation of InGaAs.

Segregation, one fundamental epitaxy-related phenomenon which is predicted as well by the above-mentioned growth model, is the key element allowing selective injection of carriers into a PQD, when its structure is embedded into a PIN junction. The whole fabrication process is described, including a selective-contacting technique that allows the realization of the electrical excitation of PQDs, one of the requirements for an efficient integration of PQDs on a photonic platform. On-demand generation of both single photons and entangled photon pairs is demonstrated from this device, the latter also importantly reaching a record fidelity to the ideal entangled state of 0.82 (upon the application of an appropriate time-filtering technique) and violating Bell's inequalities.

Among the unique possibilities offered by the PQD system is the capability of precisely stacking one quantum dot over another, allowing the formation of interacting multiple-QD systems. A first study of the statistics resulting from the fabrication of multiple PQDs with different distance and number of QD is here presented, showing how the QDs affect each other and offer further "tuning-knobs" for controlling their optical properties. For example, stacking two PQDs at the right distance can result in the generation of two subsequent photons with the same energy, which was previously reported only in a specific case of self-assembled QDs.

However, limitations in the quality of the optical properties of PQDs are still in place for actual technological implementations. Among these is the distribution of emission energies and the residual fine structure splitting (FSS) affecting the quality of the entangled photon pairs. A piezoelectric stress-based tuning technique is used to tune both the emission energy of PQDs and their FSS, demonstrating also restoral of entanglement upon the application of the proper stress.

Finally, a new method for releasing PQDs is shown, which allows their manipulation on several substrates and opens up new possibilities for the integration of the QDs onto functional platforms. As an example, integration over a multimode fiber is demonstrated as well as the emission of single-photons directly through the fiber.

Chapter 1
Introduction

"Non-classical" light is the term generally employed when dealing with light that cannot be described solely by classical electromagnetism theory, but that requires considering the quantization of the electromagnetic field itself and, in general, quantum physics concepts. In fact, light can be described as discrete packets, *photons*, which hold the properties of a generic quantum particle. Therefore it is possible to talk about quantum states of the photon, superposition of states and manipulation of its wavefunction. In *light* of these properties, photons gain great importance for application in the field of quantum information. Although simple optical elements can be employed to build a "quantum circuit" and do not represent a huge technological challenge at this stage, the biggest struggle for quantum optics is still tackling an optimal source of quantum light.

In this chapter some of the general basic principles around quantum optics will be taken into consideration and put in perspective with the requirements for quantum information and quantum computation and with the available quantum light sources. Advantages and limits of quantum dot-based sources will be considered. Finally, the scope of this thesis will be outlined and a summary of the chapters and papers composing the thesis will be provided.

1.1. Photonic qubits and quantum computation

The quantum state of polarization of a single photon can be described by a linear combination of states in either linear or circular basis employing the bra/ket formalism:

$$|\varphi\rangle = \alpha|H\rangle + \beta|V\rangle = \gamma|D\rangle + \delta|A\rangle = \eta|R\rangle + \nu|L\rangle$$

where H and V are horizontal and vertical linear polarizations, D and A are diagonal and anti-diagonal linear polarizations, R and L are right and left circular polarizations, and $\alpha, \beta, \gamma, \delta, \eta, \nu$ are complex coefficients fulfilling the normalization condition $\langle\varphi|\varphi\rangle$ =1. We can arbitrarily choose two perpendicular polarizations and assign them the state "0" or "1" (e.g. H as 0 and V as 1) and write this state in the form of:

$$|\varphi\rangle = \alpha|0\rangle + \beta|1\rangle$$

and treat the photon as the carrier of a *qubit.*

A qubit is the generalization of a classical bit, where the 1 and 0 logical values are substituted by a quantum superposition of the states of a two-level system. The advance from a discrete two-value variable to a one continuous complex variable

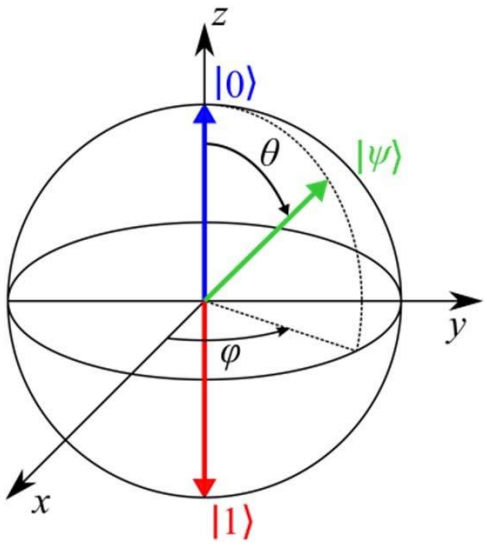


Fig.1: The "Bloch sphere" used to represent all the possible states a qubit can assume; two continuous real variable (or the two components of a complex variable) are enough to define any point on the sphere, therefore all the possible superposition of states between $|0\rangle$ and $|1\rangle$.

(which is enough to describe a qubit given normalization conditions of the quantum state, Fig.1) opens up enormous potential to improve computation capabilities of what would be called a *quantum computer* [1]. In such a machine, classical gates also have a quantum counterpart, needed to manipulate the state and make two qubits interact with each other. The application of a quantum gate to a superposition of states rather than on one single discrete variable allows for the parallel processing of each element composing the superposition, while the quantum nature of the qubit makes it possible to have new types of gates, not conceivable in the classical case. Among these, special attention is deserved by *entangling* gates, which make the qubits interact with each other in such a way that they cannot be described independently anymore, but as a whole, and a measurement operation on one qubit affects the entangled counterpart, whatever the distance.

The computational power of a quantum computer lies in principle in the combination of the parallel processing and entangling operations applied to a multi-qubit superposition of states. It will allow outperforming a classical computer, not in classical terms of performance, but meaning that it will allow to tackle higher-complexity problems with new algorithms lowering the overall complexity of the problem. One very renowned example is Shor's quantum algorithm for factoring large numbers [2], which would allow modestly sized quantum computers to outperform the largest classical supercomputers in solving some specific problems important for data encryption. A quantum computer will enable a number of new applications related to the quantum phenomena, which for the moment cannot find a classical counterpart. For example it is most likely that among the first application of a quantum computer will be the simulation of quantum systems themselves [3].

Although several different implementations of a quantum computer have been proposed and currently tackled, from superconducting qubits to trapped ions, photons seem to be among the most promising carriers of quantum information. For instance, simple optics elements can be employed to build quantum gates for

photons: polarizers and waveplates to manipulate/shift the polarization state and beamsplitters to make two photons interact. Moreover, photons have a very low chance of decoherence events arising from interactions with the environment. E. Knill et al. [4], have proposed a scheme to realize universal quantum computation with only linear optics, sources of single photons and single photon detectors, which takes the name of linear optics quantum computation scheme (LOQCS). Given that according to this scheme all the universal gates can be realized for a true universal quantum computer, its realization is still in principle extremely demanding. For instance, quantum memories could be necessary, as well as error correction methods.

Other computational schemes were proposed demanding less stringent requirements but allowing a non-universal quantum computation which could be employed to solve specific problem, especially ones which apply to the simulation of other quantum systems. Boson sampling [5] is the most remarkable example of this and it just requires single-photon sources, linear optics elements (typically in the form of an integrated photonic circuit) and single-photon detectors.

If from a technological point of view both integrated waveguides and detectors are available and well developed (though requiring further performance improvements), the real challenge in order to achieve a photonic implementation of quantum computing lies in the development of sources of photons which meet a list of strict requirements, as we will see in the following. In the meanwhile we will summarize by saying that the key elements needed for photonic quantum computation are: manipulation of superposition of polarization states to prepare a qubit in the needed initial state and/or perform single gate operation on them; indistinguishability of the photons (i.e. they have to have the same energy and be coherent) in order to make them interfere and interact with each other in two qubit gates; entanglement of the photons which interacted.

1.1.1. Quantum key distribution and entanglement

Other fields of quantum information could also be built on a photonic implementation, e.g. quantum cryptography. It is in this field that one can easily understand the potential of entangled qubits. For instance, quantum key distribution protocols have been proposed which make use of polarization entangled photon pairs.

An interesting example is protocol E91, which we will briefly explain in a simplified view. In this protocol, the two entities involved in the communication are typically referred to as Alice (the sender) and Bob (the receiver). Alice makes use of an entangled photon pair as a carrier of information: she sends one photon of the pair over to Bob, and then both Alice and Bob perform measurements on their photon. If the two photons are perfectly entangled and Alice and Bob measure in the same basis, then they will obtain correlated results. If an eavesdropper intercepts the photon sent from Alice to Bob and measures it, he will break the entanglement by making the two-photon-state collapse onto the specific basis he has used. It will be evident then to Bob that the communication with Alice has been interfered with, as confronting the statistics of his measurement with Alice's won't correspond to the expectation. This process has to be repeated a number of times and Alice and Bob will have to discard many measurements to allow a very secure communication and completely exclude that an eavesdropper is intercepting their photon. If the test passes, they can use the photons they have not discarded as their secret key and encode their messages using that.

Apart from this specific example of application, entangled photons would allow also to simplify the quantum computation scheme, reducing the need of entangling gates. The definition and properties of entangled photons will be explained in the following more in detail.

1.2. Single-photon sources

In order to observe a photon and practically employ its properties as a particle it is required to have a source of light that follows a sub-Poissonian distribution of generation of photons [1]. Photon statistics describe how the number of photons emitted by a light source fluctuates, how the properties of these photons vary, and how photons are correlated with each other. Because of the nature of the generation phenomenon, lasers always produce Poissonian light, where the probability of generating a certain number of photons is of the form:

$$P(n) = e^{-<n>} \frac{< n >^n}{n!}$$

with $P(n)$ the probability of emitting n photons in a determined time interval and $< n >$ the average number of photons emitted. The variance of the number of photons following a Poissonian statistic is equal to $< n >$ itself. The photon number statistics of common ("classical") light sources such as incandescent filaments, fluorescent gasses, light-emitting diodes, instead, follow a or super-Poissonian distribution (having variance greater than the mean number of photons generated). Sub-Poissonian distributed light can only be obtained through quantum mechanical related phenomena and presents a variance that is lower than the mean number of photons. It is only in the sub-Poissonian regime one can have emission of precisely one photon at a time.

For instance, the light generated by a laser can be attenuated so that, on average one photon arrives at a detector in a specified time interval [6][7]. However, for a classical light source, there will always be a finite probability of measuring n photons for any $n > 1$.

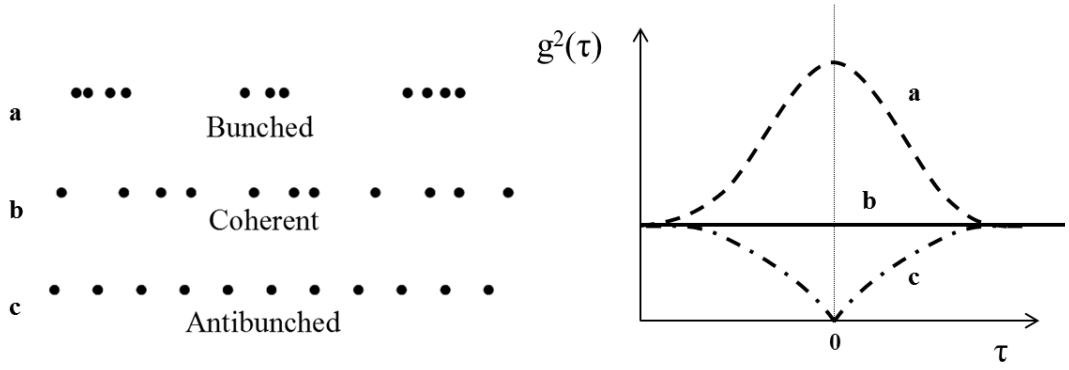


Fig.2: Representation of bunched, coherent and anti-bunched light in terms of photon arrival time (on the left) and autocorrelation function (on the right).

The statistic characterizing a specific source is directly reflected in the second order autocorrelation function:

$$g^2(\tau) = \frac{< n(t)n(t+\tau) >}{< n(t) >< n(t+\tau) >}$$

where $n(t)$ is the number of detected photons at the time t. If we have a perfectly Poissonian light source, $g^2(\tau)$ will be equal to 1 for any τ, representing the fact that photons come in between random time intervals and the probability of emitting a photon is the same for all values of τ. It can be proven [1] that super-Poissonian light sources show $g^2(0) > 1$, while sub-Poissonian sources have $g^2(0) < 1$ and it is exactly zero when we have a perfect single photon emitter. $g^2(0) < 0.5$ means that on average less than two photons are found at the same time and it can only be obtained through non-classical processes, which is why 0.5 is generally considered as the "classical limit". The second order autocorrelation function can be measured by employing a standard Hanbury-Brown and Twiss (HBT) setup. This is made of a simple 50:50 beamsplitter sending half of the photons to one detector and half of the

photons to another detector. The signal coming from these two is then correlated by using the signal of one detector as a "start" signal and the signal from the second detector as a "stop" signal of a correlator. One can then collect the histogram of the time differences measured at the two detectors which will mimic the $g^2(\tau)$ of the light source. Fig.2 shows the typical function one can obtain from different types of light sources. Super-Poissonian sources will show *bunching*, while sub-Poissonian will show *anti-bunching*.

1.3. Indistinguishable photons

Control over single photon generation is not enough to achieve a functioning two-photon gate, as the two photons need to be *indistinguishable* in order to interact with each other, meaning that the two photons must be identical in energy and coherent. The Hong-Ou-Mandel effect is the typical experiment revealing indistinguishability of photons.

Let us consider two identical photons impinging on a 50:50 beamsplitter (fig3): we can label the two entrances of the beamsplitter as a and b and the two exits as c and d, while the two photons will be labeled as 1 and 2.

The two-photon-state composed of two indistinguishable photons (1 and 2) impinging on the two entrances a and b of the beamsplitter can be expressed as a quantum state which is symmetrical for particle exchange (bosonic state):

$$|\varphi\rangle = \frac{1}{\sqrt{2}}(|a\rangle_1|b\rangle_2 + |b\rangle_1|a\rangle_2)$$

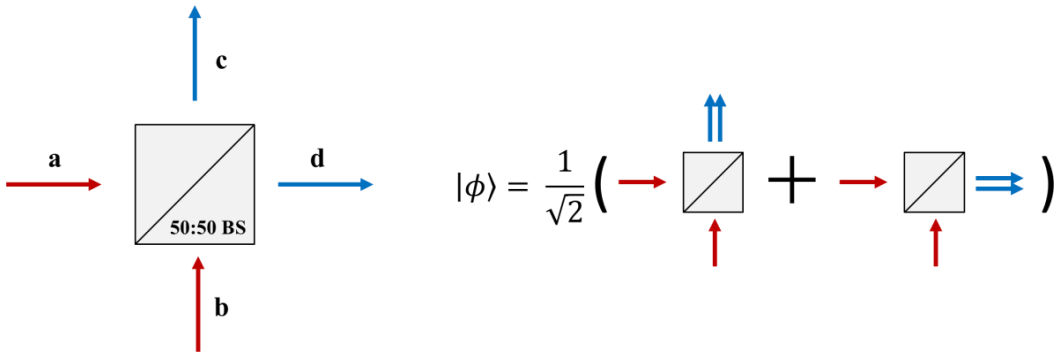


Fig.3: Reference scheme for the Hong-Ou-Mandel experiment explained in the text indicating the labeling for entrances and exits of the 50:50 beamsplitter (on the left) and symbolic representation of the resulting state (on the right).

The effect of the beamsplitter on each photon can be evaluated considering the unitary transformation associated with it. If we choose as a reference basis ($\hat{\boldsymbol{a}}$; $\hat{\boldsymbol{b}}$), where $\hat{\boldsymbol{a}}$ is the horizontal direction and $\hat{\boldsymbol{b}}$ the vertical direction (according to Fig.3), we can write the unitary transformation associated with the beamsplitter as:

$$U_{BS} = \frac{1}{\sqrt{2}}\begin{bmatrix} 1 & i \\ i & 1 \end{bmatrix}$$

where U_{BS} maps the input ($\hat{\boldsymbol{a}}$; $\hat{\boldsymbol{b}}$) to the output ($\hat{\boldsymbol{d}}$; $\hat{\boldsymbol{c}}$) of the beamsplitter. It is straightforward to show that the resulting state, written in terms of c and d is:

$$|\phi\rangle = \frac{i}{\sqrt{2}}(|c\rangle_1|c\rangle_2 + |d\rangle_1|d\rangle_2)$$

which means that the two photons will always exit the same side of the beamsplitter. If the two photons are not indistinguishable, coalescence of photons at the same exit will not appear. Experimentally the Hong-Ou-Mandel effect can be employed to determine whether the photons coming from two sources (or two photons generated

by the same source) are indistinguishable or not [8]. This is done by sending the two photons towards the two opposite entrances of the beamsplitter and varying the delay of the arrival between the two. If the photons are identical and have the same phase (controlled by varying the delay) then they will interfere and result in the coalescence of the photons at the same exit.

1.4. Entangled photons

Entanglement arises between pair or group of particles which interacted in such a way that they cannot be described independently anymore but they have to be described as a whole. Considering a two-level-system-based qubit, Bell states are among the most simple two-qubit entangled states, which can be written as:

$$|\psi^{\pm}\rangle = \frac{1}{\sqrt{2}}(|0\rangle_1|1\rangle_2 \pm |1\rangle_1|0\rangle_2)$$

$$|\phi^{\pm}\rangle = \frac{1}{\sqrt{2}}(|0\rangle_1|0\rangle_2 \pm |1\rangle_1|1\rangle_2)$$

where 1 and 2 labels the qubit and $|0\rangle$ and $|1\rangle$ are two levels of each qubit.

When two particles are entangled they exist as an inseparable system, as their wavefunction cannot be written in the form of a product of two independent qubit states by factorization. As a consequence, the measurement of an entangled single particle, according to quantum mechanics, makes its wavefunction collapse onto one of the two possible states and has an instantaneous effect on the state of the entangled counterpart, whatever the distance between the two particles.

As we have seen, this effect can be exploited in quantum key distribution protocols, but also entanglement of particles is one of the quantum properties that allows quantum computation to be more effective than classical one. Of course having

entangled pairs already available could simplify the computational scheme allowing to “skip” one entangling operation between particles.

Producing entangled particles always relies on a system in which identical particle states can be created, whose indistinguishability is then reflected in the symmetrization (or anti-symmetrization) of the two (or more) particle states, which can be an entangled state. For instance, two identical photons exiting at the same time from a beamsplitter according to the picture presented in the previous paragraph are entangled photons.

1.5. Sources of quantum light

The challenge for photonic quantum information lies in the ability of producing in a controlled way photons which present the above-mentioned properties. Although singularly these results can be achieved in different ways and were proven on a single-emitter scale, a proper source of photons needs to meet a list of quite strict requirements to be considered a technology on which to build quantum computation. If we restrict, for now, at the case of a quantum computer based on single-photons which would be employed in a LOQC scheme, these requirements would/could be:

- **Emission energy uniformity**, as different emitters would have to emit all at the very same energy (or to be able to be tuned to the same energy), and **spectral purity**, meaning generating radiation characterized by a transform-limited linewidth, also somehow reflecting the fact that consecutively emitted photons would have the very same energy as well;
- **Single-photon emission**, so that exactly one photon state is systematically generated in a controlled way [9];

- **On-demand generation**, to have one single photon at the required time, typically upon a pulse excitation of some nature;
- **Source brightness**, which means that for every excitation pulse one can obtain one photon out of the source, which is closely related to the ability of coupling the photons to waveguides/detectors;
- **Position control**, over the sources allowing to have a large number of emitters on a scalable platform that can be repeated as many times as necessary with the same properties;
- **Integrability,** which is the ability of integrating the quantum emitters onto a platform allowing easy and efficient coupling with waveguides, optical fibers and similar structures.

This qualitative list of requirements is in principle enough to guarantee the proper functioning of a quantum computer based on single-photons. **Entangled photon emission** can allow simplifying the quantum computational scheme, but also it is required for other applications in quantum information and quantum cryptography, as we had the chance to say beforehand.

From a technological point of view, instead, integrability can take several forms, of course, which need to take into account also the way the sources are addressed and stimulated to produce a photon. It would be extremely favorable to be able to address the emitters by means of an **electrical injection**, allowing easy control through “classical” channels.

Although several approaches have been proposed which could successfully be employed for this purpose, only a few are actually heavily investigated and promising on the long run. We will here briefly review some of the most studied or historically relevant.

1.5.1. Single atoms

Single atoms can interact with electromagnetic field, absorb or emit a photon with energy equal to that of an electronic transition. When the atom is excited, one or more electronic transitions take place according to quantum mechanical selection rules, each having its characteristic lifetime which depends on the overlap between the wavefunctions of the initial and final state, and a photon is emitted carrying the energy difference between the two states. After an emission event, before the same transition can happen, the atom has to be excited again. The probability of two photons being emitted a short time after each other is therefore very small, which makes single atoms suitable for single photon generation. Antibunching was observed historically in photons obtained from the excitation of single Sodium atom beams [10][11], while trapped atoms were used to obtain single-photons [12][13]. The generation of polarization-entangled photon pairs was firstly demonstrated from single atoms[14][15][16]. This was achieved by preparing atoms in a singlet state, made of two indistinguishable electrons, so that the total two electron state is

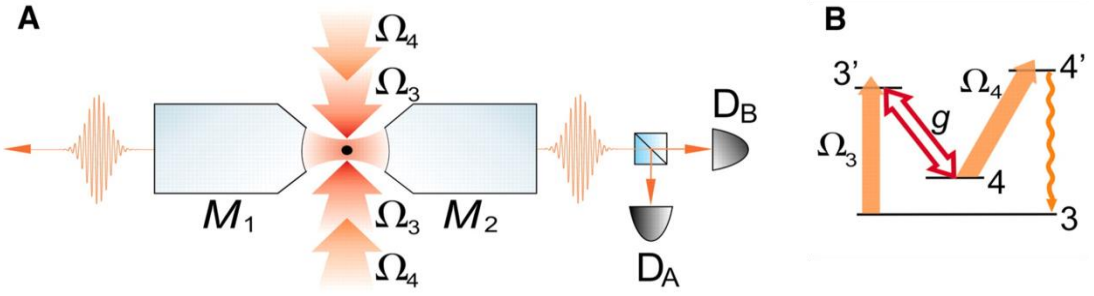


Fig.4: Illustration of the generation of single photons by one atom trapped in an optical cavity from [12]. (A) A single Cs atom is trapped in a cavity formed by the reflective surfaces of mirrors (M1, M2) and is pumped by the external fields (Ω3, Ω4) (25). (B) The relevant atomic levels of the Cs D2 line used to prove single photon generation. From J. McKeever et. al., Science, vol. 303, no. 5666, pp. 1992–1994, Mar. 2004. Reprinted with permission from AAAS.

entangled. The entanglement is transferred to the two photons emitted subsequently in the relaxation cascade. Of course it is not possible to obtain a scalable system based on neutral single atoms, as trapping and controlling them is extremely demanding.

1.5.2. Spontaneous parametric down conversion (SPDC)

SPDC is a nonlinear optical process from which a pair of signal–idler photons is generated when a pump laser beam is incident onto an optical nonlinear material. These two photons, in accordance with the laws of conservation of energy and momentum, have combined energies and momenta equal to the energy and momentum of the original photon and crystal lattice, they are phase-matched in the frequency domain, and they have correlated polarizations. The SPDC process is referred to as type-I if the signal and idler photons have identical polarizations and type-II if they have orthogonal polarization [17]. The two photons are single photon pairs, while the generation of higher number of photons is a process proportional to higher order susceptibility terms, which is low in low pumping power regimes.

In type-II processes, photons with orthogonal polarization are emitted in two cones one ordinarily polarized, the other extraordinarily polarized. In the case of degenerate emission, i.e. the idler and signal having the same energy, one can set the pump laser at an angle with respect to the crystal axis for which the two cones intercept (Fig.5) and therefore the (identical) photons collected from this intersection will be polarization entangled [18]. Moreover, a photon from the entangled pair can be employed to “herald” the arrival of the second photon and post-select it to improve the effective single-photon quality [19].

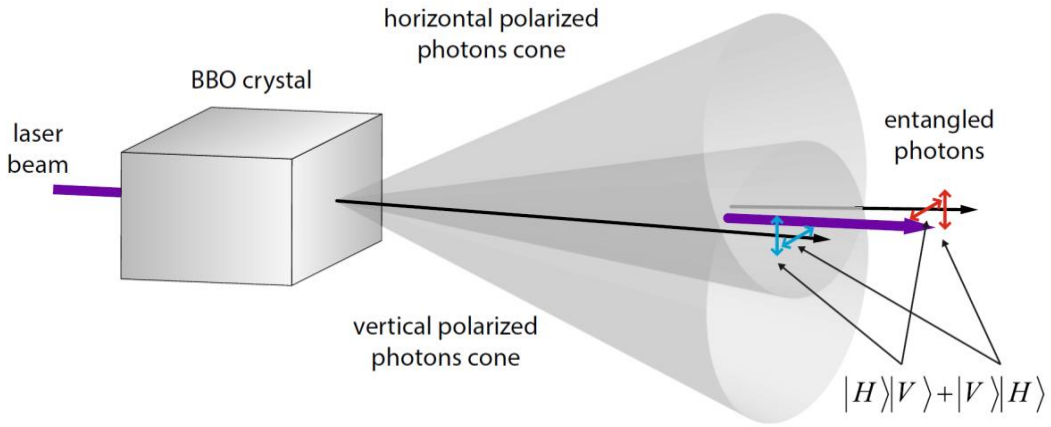


Fig.5: Generation of entangled photon pair by SPDC employing a birefringent, nonlinear crystal BBO; two conical photon beams are generated with opposite polarization (upper beam with vertical polarization and lower beam with horizontal polarization in the scheme); at the intersection of the cones the polarization is not determined, therefore photons collected from this cone (at specific angles) are indistinguishable and polarization entangled. From M. Jacak et. al., Opt. Quantum Electron., vol. 48, no. 7, p. 363, Jul. 2016.

SPDC has been an essential experimental resource for fundamental research as it was employed efficiently to prove violation of Bell's inequality [20][18][21], implementations of quantum cryptography protocols [22][23], long-haul quantum teleportation [24][25], multi-photon entanglement [26][27]. The probabilistic nature of the down-conversion process, though, represents the main issue of this source, which affects true on-demand generation. Moreover the system is hardly scalable and integrable due to its intrinsic "bulky" nature, although approaches for miniaturization are being studied.

1.5.3. Nitrogen-vacancies

Single nitrogen-vacancy (NV) centers in diamonds constitute another system which raised interest for quantum optics applications. They are formed by a substitutional

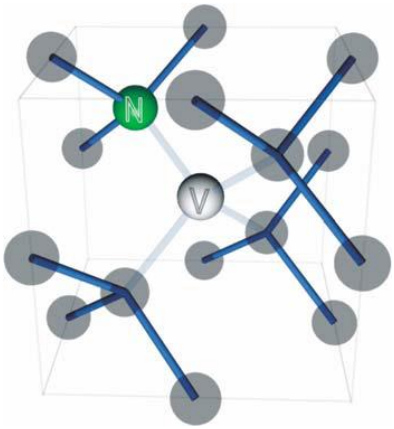


Fig.6: Schematic representation of the nitrogen vacancy (NV) centre structure. From F. Jelezkoet. al., Physica Status Solidi (A) Applications and Materials Science, vol. 203, no. 13., pp. 3207–3225, 01-Oct-2006.

nitrogen atom with a vacancy trapped at an adjacent lattice position (Fig.6), which are usually prepared in type Ib synthetic diamond, where single substitutional nitrogen impurities are homogeneously dispersed [28]. Alternatively, the NV centers can be created by electron or neutron irradiation [28][29] and by successively introducing nitrogen atoms via high temperature (~900C) annealing. Also, CVD deposition of diamond crystals was successfully employed to produce low-density NV-centers structures. Typically, fluorescence spectra show a sharp zero phonon line (ZPL) at 637 nm and a vibrationally-broadened emission peak (~ 620 to 740 nm) [28][30].

The high radiative quantum efficiency even at room temperature as well as a short decay time of the excited state makes them well-suited for single photon generation. In fact, samples can be obtained with a relatively low concentration of NV-centres which allow individual addressing of the emitter. Strong antibunching behavior has been observed from the zero phonon lines therefore demonstrating single photon emission [31]. NV-centres can also be placed in resonant cavities e.g. to improve linewidth [32] and electrically driven [33]. Other significant results obtained by

studying NV centers were spin-photon entanglement [34] and multipartite entanglement [35]. Site-control over the NV center is a challenging task, though, and a limit for practical application.

1.6. Semiconductor quantum dots

We will now concentrate our attention on the general properties of semiconductor quantum dots (QDs), which is the subject of this thesis. A semiconductor QD is a nanostructure in which carriers are confined in three dimensions in a region extended in the order of their de Broglie wavelength by means of energy gap engineering. Hence, electrons and holes are subject to quantum confinement effect and can occupy only discrete energy levels inside the QD, which is why they are generally referred to as “artificial atoms” and can have very interesting properties in terms of non-classical emission. QD properties can be easily engineered by varying their dimensions or composition to modify the energy and the nature of the transitions, making them a very versatile system.

Continuing the parallel with atoms, rather than electronic levels one can talk about excitonic complexes inside a QD: an exciton is a complex composed of a bound electron-hole pair, generated in the QD upon e.g. absorption of a photon with sufficient energy. Other complexes can be excited inside a QD which are composed of different number and types of carriers, such as positively charged exciton (two holes and one electron), negatively charged exciton (one hole and two electrons), and biexciton (two electron-hole pairs). According to Pauli Exclusion Principle, each level in the QD either in conduction or valence band can host respectively up to two electrons or holes with opposite spin. Upon the recombination of an electron and a hole of any excitonic complex a photon is emitted which carries characteristic energy for that transition. Typically, different transitions are not degenerate thanks to

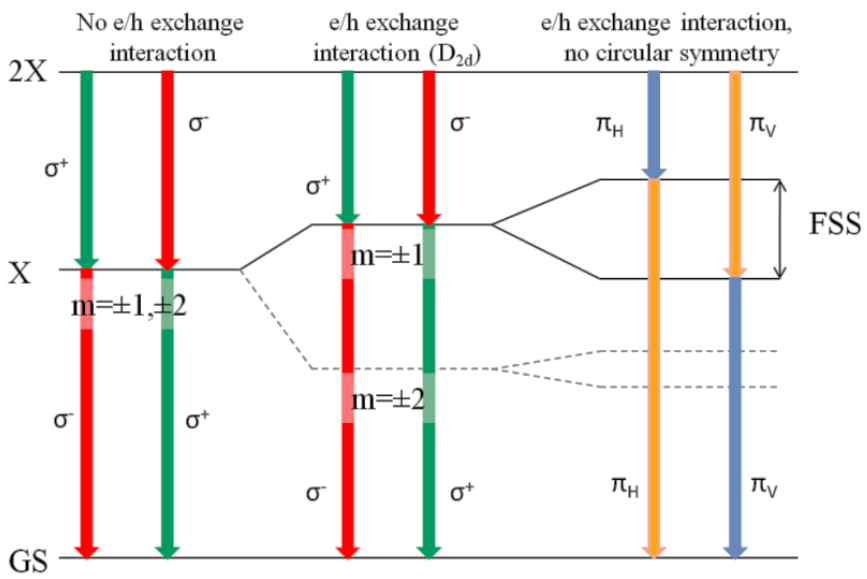


Fig.7: Sketch of the emission cascade 2X → X under no e/h exchange interaction (left),for circular symmetry (D_{2d}) (center) and with no circular symmetry (right). Bright and dark states are indicated with continuous and dashed trace respectively. A transition from circularly right/left circular polarization ($\sigma_{+/-}$) to linear polarization ($\pi_{H/V}$) occurs when circular symmetry is lost. From [75].

different Coulomb interaction and therefore correspond to a different energy of the photons emitted. Hence, the emission spectrum of a quantum dot contains the signature of the (optically active) complexes forming in it.

The transition between two complexes or with the fundamental state is therefore characterized by a lifetime: the average time between the generation of the complex and the recombination. This means that, just like for an atom, after a recombination event, a typical time has to pass before the QD is re-excited and emits the same photon again. This process can be exploited to generate high purity single-photons.

1.6.1. Fine structure in a quantum dot and entangled photon emission

The energetic configuration of the biexciton-exciton-ground state recombination cascade (Fig. 7) plays an important role in the generation of polarization-entangled

photon emission from a QD (Fig.7). Let us first consider a neutral exciton complex under the assumption that the separation between heavy-holes and light-holes levels is energetically large enough (a few meV) to allow neglecting the contribution of light-holes. An electron has a spin value of $S = 1/2$ while the total angular momentum of a hole is $J = 3/2$: to build the total angular momentum of an exciton, then, we need to combine the possible values of the eigenvalue of S_z and J_z , $M = S_z + J_z$. Thus there are four possible combinations: $-2, -1, 1, 2$. States with M=1 are said bright as they can interact radiatively with a photon, either directly absorbing or emitting it, while states with $M = 2$ are dark states and cannot be radiatively coupled directly to the ground state. Because of the exchange interaction between the spin of the electron and the total angular momentum of the hole, levels with different $|M|$ have different energy. The degeneracy between states $M = \pm 1$ can also be lifted depending on the symmetry of the QD: if it is symmetric, the natural basis on which one can express the eigenstates of the Hamiltonian representing the system are $M = \pm 1$. If its symmetry is less than D_{2d}, then the two levels are not degenerate anymore and the eigenstates of the Hamiltonian with eigenvalues corresponding to the energy of the split levels are $M = +1$ and $M = -1$. In the symmetric case, photons which have circular polarization (or linear combinations of it, respecting momentum conservation) can be emitted by the QD, while in the non-degenerate case photons with horizontal and vertical polarization are emitted with different energy, the energy difference being generally referred to as fine structure splitting (FSS) of the QD.

Polarization entangled photons can be produced through the recombination cascade biexciton-exciton-ground state. If the biexciton level of a QD is populated, the two electron-hole pairs are identical pairs with even total angular momentum, hence they will behave as bosons and their wavefunction needs to be totally symmetric for exchanges of particles. The two electron-hole pairs are therefore spin-entangled. After the first recombination event, one photon is produced and one exciton is left in

the quantum dot for a time equal to the lifetime of the excitonic transition. The two are in principle still entangled. Upon the exciton recombination, if the FSS is small enough then the final state of the two photons can be written as:

$$|\phi\rangle = \frac{1}{\sqrt{2}}(|R\rangle_{XX}|L\rangle_X + |L\rangle_{XX}|R\rangle_X)$$

which in linear basis is:

$$|\phi\rangle = \frac{1}{\sqrt{2}}(|H\rangle_{XX}|H\rangle_X + |V\rangle_{XX}|V\rangle_X)$$

If there is a significant FSS, instead, after the emission of the first photon, components of the exciton with different spin state will evolve differently in time, building a phase that is equal to $E_{FSS}\,\tau/\hbar$, where τ is the exciton lifetime. Therefore we have to write the following two-photon state:

$$|\phi\rangle = \frac{1}{\sqrt{2}}\left(|H\rangle_{XX}|H\rangle_{XX} + e^{\frac{i\,E_{FSS}\,\tau}{\hbar}}|V\rangle_{XX}|V\rangle_X\right)$$

the magnitude of the phase term depends on the product of τ and FSS. From it, it depends the ability of detecting entanglement from the pair. The two photons are still entangled in principle even with a large FSS but the distribution of lifetimes τ combined with a large FSS as a result scrambles the relative polarization of the entangled state and degrades the ability of detecting entanglement [36].

The asymmetry that gives rise to the FSS can have different sources: it can be simply a geometrical asymmetry of the QD itself, the presence of a non-biaxial piezoelectric strain or alloy disorder due to the random distribution of the elements composing the alloy the QD is made of.

1.6.2. QD systems and achievements

Several semiconductor QD-based systems have been proposed and employed in the field of quantum optics which allowed demonstrating important fundamental physics results and showed the potential of a quantum computer based on this type of source.

The most relevant and studied QDs are self-assembled QDs grown by molecular beam epitaxy (MBE) in an epitaxy regime called **Stranski-Krastanov** [37]: the driving force for the formation of these QDs is the lattice mismatch between the substrate and the natural "bulk" crystal organization of the layer grown on the top of it. An extremely important example is InAs QDs grown on a (100) oriented GaAs substrate: during the layer-by-layer deposition of the first few monolayers of InAs its structure follows that of the GaAs crystal underneath at the cost of building up strain, forming the so-called

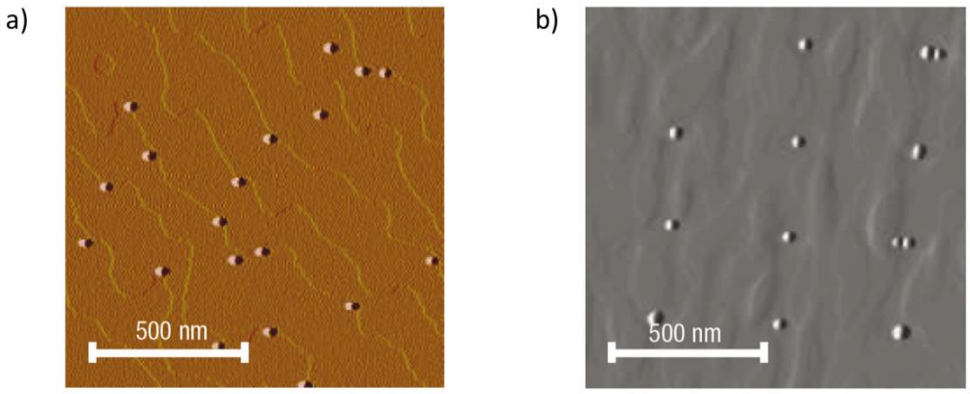


Fig.8: Atomic force microscopy images of (uncapped) Stransky Krastanov QDs; a) randomly positioned InAs QDs; b) a layer of InAs quantum dots whose locations have been seeded by a matrix of nanometer-sized pits patterned onto the wafer surface. From: A. J. Shields, *Nat. Photonics*, vol. 1, no. 4, pp. 215–223, Apr. 2007.

wetting layer; at some point as the deposition continues and the strain builds up, the structure “relaxes” and, rather than maintaining layer-by-layer growth, 3D structures start to form which minimize the strain + surface energy of the whole structure. The 3D growth typically happens spontaneously along the surface and takes the form of droplet-like structures, which are then capped with GaAs to allow for the confinement in InAs and therefore the formation of the QDs.

Another self-assembled QD deposition technique which gained increasing importance in recent years is **droplet epitaxy** [38]: group III elements (Ga, In or Al), deposited on the substrate at higher temperature than their melting point, segregate to droplets of nanometre-sized dimensions. During the following step, the droplets are exposed to the flux of group V elements and crystallization of the droplets into III-V QDs occurs. Such growth method can be exploited growing strain-free QDs (GaAs/AlGaAs), as well as strained (InAs/GaAs).

Based on droplet epitaxy, local droplet etching (LDE) [39][40] utilizes metal droplets during molecular beam epitaxy for the self-assembled drilling of nanoholes into III/V semiconductor surfaces. Instead of employing a flux of group V elements, the sample is annealed and the group III droplets drill nanoholes into the substrate. These are then filled with material composing the optically active region of the QDs and finally capped. Highly symmetric GaAs in AlGaAs QDs can be produced with this technique [41].

Self-assembled QDs were employed to demonstrate single photon emission [42], polarization-entangled photon pair emission upon both optical [43][44] and electrical injection [45], indistinguishable photon generation [46][41], high extraction efficiency [47], as well as fundamental physics results for which the versatility of the QD system is exploited (e.g. quantum dot molecules [48], exotic excitonic complexes [49]). Epitaxial growth conditions for which very symmetrical self-assembled QDs can be produced [50], together with the relatively simple structure of the system exploitable for producing more sophisticated devices [51][52] and the possibility of integrating

the QDs into a resonant cavity for enhancing the emission via Purcell effect [53] are the winning elements of this type of QDs.

The main limit of the self-assembled QD approach is the lack of a control over the position and dimensions of the emitters. The random distribution of their properties makes it necessary to investigate a large number of them in order to find a "champion" QD which allows demonstrating physics principles. It doesn't actually represent a technological viable option for the realization of quantum computation, unless sophisticated tuning [54] and post selection techniques [55] are employed.

Alternative approaches are based on site-controlled techniques. For example **seeded Stranski-Krastanov QDs** were obtained by creating nucleation sites on the surface of the growth substrate [56]: the GaAs substrate was patterned with shallow (~20 nm) holes with a diameter of ~100 nm then filled with GaAs buffer and InAs which act as preferential QD nucleation sites. Although it was possible to produce QDs emitting indistinguishable photons from this system, still the control over the QD formation was not perfect and FSS was large. Of great importance are also semiconductor systems based on **QD in nanowires** [57]. The most effective method for the fabrication of this system is the bottom-up approach, where the QDs are included in the NW structure during the growth process, just by changing the precursors. In general, bottom-up NW fabrication relies on the vapor–liquid–solid method: a nanoscale metal droplet, typically gold, initiates the one-dimensional growth and acts as a catalyst site. Ordered arrays of NWs can also be achieved after lithographic processing of deposited gold films. Single photons [58] as well as entangled photons [59] could be generated using QDs in nanowires. Other advantages are the ability of enhancing light extraction by engineering the shape of the nanowire [60] as well as the possibility of manipulating nanowires (although not in a scalable way) and place them in integrated circuits [61].

1.6.3. Pyramidal quantum dots and thesis outline

The pyramidal quantum dot (PQD) system is a naturally site-controlled system based on metalorganic vapour phase epitaxy (MOVPE). As it will be explained in more detail in the next chapter of this thesis, an ordered array of pyramidal recesses is defined in a GaAs substrate, on which then the InGaAs QD layer is deposited in between GaAs barriers. The geometry of the pyramid itself shapes the deposited layers in the form of a QD: each pyramidal recess hosts exactly one quantum dot at the very tip of the pyramid. Extraction efficiency is improved by a back-etching technique to remove the original growth substrate and reveal the tip of the pyramidal structure. PQDs have shown narrow distribution of emission energies and spectral purity [62], but most importantly they have been proven to emit single photons [63][64] and entangled photons [65] upon optical excitation.

In **chapter 2** the general fabrication process and photoluminescence measurement setup will be reviewed in detail. The MOVPE mechanisms involved in the formation of the nanostructures inside a pyramidal recess will be discussed as well. The work presented in the following chapters is based on these procedures and techniques.
Chapter 3 is based on the paper “Indium segregation during III–V quantum wire and quantum dot formation on patterned substrates” [66]. Here the attention focuses on the epitaxy mechanism: a reaction-diffusion kinetic equation-based model is employed to simulate and reproduce the evolution of the growth facets profile and composition of the InGaAs layer in pyramidal recesses. A noticeable case of MOVPE-grown nanostructure from the literature [67] is taken into consideration to obtain parameters to be used in the simulation of nanostructures forming inside the pyramidal recess. The successful application of the growth model not only proves to be a useful tool to guide the choice for growth parameters, but also provides important insight on the nature of MOVPE performed over non-planar substrates.

The achievement of the electrical injection of PQDs is an important milestone to prove integration capabilities of a non-classical light source. In **chapter 4**, based on the paper "Selective carrier injection into patterned arrays of pyramidal quantum dots for entangled photon light-emitting diodes" [68], the realization of a PQD-based LED is demonstrated. Here the QD is embedded in the intrinsic region of a PIN junction. Fabrication strategies are used to deal with the non-planar nature of the PQD, including the insertion of a growth-engineered vertical quantum wire. Entangled photon emission is proven from more than one quantum dot upon continuous and pulsed electrical excitation. Importantly, Bell's inequalities are violated, proving the real quantum nature of the emitted radiation.

In **chapter 5** the same kind of device from chapter 4 is studied and characterized in terms of single-photon emission upon both continuous and pulsed electrical injection. In the paper "On-demand single-photons from electrically-injected site-controlled Pyramidal Quantum Dots", a time-gating technique is employed to improve the quality of the single-photon emission and discard events that are related to electrical afterpulses exciting the PQD. Significantly, the comparison of this time-gating technique with the previous experiment demonstrating entangled photon emission gives insight about the possible different filtering methods that can be practically employed to improve quality of the resulting photon statistics.

A unique feature of PQDs is the ability of stacking two or more QDs precisely one on top of each other. This is explored extensively for the first time in "Statistical study of stacked/coupled site-controlled pyramidal quantum dots and their excitonic properties" [69], reported here as **chapter 6**. The effect of stacking QDs with the same thickness at different distances is investigated, based on the collection of a large statistics. A variation of the optical properties of the QDs is observed (e.g. emission energy and biexciton binding energy) which hints at a form of coupling between the QDs. The stacking of a higher number of QDs had a similar effect, showing also a clear change in the polarization plane of the emitted radiation for the

case of more than 2 stacked quantum dots. Finally, the effect of the inclusion of QDs has also proven to have a clear effect on the charging character and linewidth of the excitonic transitions. Apart for providing an extra “tuning knob” for the optical properties of PQDs, the possibility of producing coupled QDs ensembles could be exploited for example for generating and controlling cluster states [70][71].

Chapter 7, from the paper “Vanishing biexciton binding energy from stacked, MOVPE grown, site-controlled pyramidal quantum dots for twin photon generation” [72], explores a specific case of stacked PQDs which present biexciton binding energy close to zero - exciton and biexciton transitions almost perfectly overlapping. The unique auto-correlation signature from “twin” photons is observed.

In **chapter 8** recent preliminary results on the application of strain to PQDs are presented. Among the several strategies that have been suggested for tuning the optical properties of QDs, the application of piezoelectric strain has proven to be a very effective method not only to control the emission energy of the QD but also to manipulate the FSS and restore entangled photon emission quality from the biexciton-exciton-ground state cascade [73][74]. The application of a quasi-biaxial stress on PQDs is discussed and the possibility of tuning its properties is demonstrated. Also, important advances in the capability of manipulating a small number or single PQDs are presented in this chapter, realized thanks to new alternative methods for the processing of these structures, allowing for the easy transfer of PQDs on different types of substrates and opening future perspectives for integration.

Finally the conclusions are drawn and the future outlook for PQD system is discussed.

References

[1] M. Fox, *Quantum Optics : An Introduction*. Oxford University Press, 2006.

[2] P. W. Shor, *SIAM J. Comput.*, vol. 26, no. 5, pp. 1484–1509, Oct. 1997.

[3] R. P. Feynman, *Int. J. Theor. Phys.*, vol. 21, no. 6–7, pp. 467–488, Jun. 1982.

[4] E. Knill, R. Laflamme, and G. J. Milburn, *Nature*, vol. 409, no. 6816, pp. 46–52, Jan. 2001.

[5] B. T. Gard, K. R. Motes, J. P. Olson, P. P. Rohde, and J. P. Dowling, *An Introduction to Boson-Sampling*, Chapter 8. World scientific, 2015.

[6] M. D. Eisaman, J. Fan, A. Migdall, and S. V. Polyakov, *Rev. Sci. Instrum.*, vol. 82, no. 7, p. 071101, Jul. 2011.

[7] P. D. Townsend, J. G. Rarity, and P. R. Tapster, *Electron. Lett.*, vol. 29, no. 7, p. 634, 1993.

[8] S. Buckley, K. Rivoire, and J. Vučković, *Reports Prog. Phys.*, vol. 75, no. 12, p. 126503, Dec. 2012.

[9] M. Varnava, D. E. Browne, and T. Rudolph, *Phys. Rev. Lett.*, vol. 100, no. 6, p. 060502, Feb. 2008.

[10] H. J. Kimble, M. Dagenais, and L. Mandel, *Phys. Rev. Lett.*, vol. 39, no. 11, pp. 691–695, Sep. 1977.

[11] R. Short and L. Mandel, *Phys. Rev. Lett.*, vol. 51, no. 5, pp. 384–387, Aug. 1983.

[12] J. McKeever, A. Boca, A. D. Boozer, R. Miller, J. R. Buck, A. Kuzmich, and H. J. Kimble, *Science*, vol. 303, no. 5666, pp. 1992–1994, Mar. 2004.

[13] B. Darquié, M. Jones, J. Dingjan, J. Beugnon, S. Bergamini, Y. Sortais, G. Messin, A. Browaeys, and P. Grangier, *Science*, vol. 309, no. 5733, pp. 454–456, Jul. 2006.

[14] S. J. Freedman and J. F. Clauser, *Phys. Rev. Lett.*, vol. 28, no. 14, p. 938, Apr. 1972.

[15] E. S. Fry and R. C. Thompson, *Phys. Rev. Lett.*, vol. 37, no. 8, pp. 465–468, Aug.

1976.

[16] A. Aspect, P. Grangier, and G. Roger, *Phys. Rev. Lett.*, vol. 47, no. 7, pp. 460–463, Aug. 1981.

[17] Y. Shih, *Reports Prog. Phys.*, vol. 66, no. 6, pp. 1009–1044, Jun. 2003.

[18] P. G. Kwiat, K. Mattle, H. Weinfurter, A. Zeilinger, A. V. Sergienko, and Y. Shih, *Phys. Rev. Lett.*, vol. 75, no. 24, pp. 4337–4341, Dec. 1995.

[19] K. R. Motes, J. P. Dowling, and P. P. Rohde, *Phys. Rev. A - At. Mol. Opt. Phys.*, vol. 88, no. 6, p. 063822, Dec. 2013.

[20] Z. Y. Ou and L. Mandel, *Phys. Rev. Lett.*, vol. 61, no. 1, pp. 50–53, Jul. 1988.

[21] M. Giustina, A. Mech, S. Ramelow, B. Wittmann, J. Kofler, J. Beyer, A. Lita, B. Calkins, T. Gerrits, S. W. Nam, R. Ursin, and A. Zeilinger, *Nature*, vol. 497, no. 7448, pp. 227–230, Apr. 2013.

[22] A. V. Sergienko, M. Atatüre, Z. Walton, G. Jaeger, B. E. A. Saleh, and M. C. Teich, *Phys. Rev. A*, vol. 60, no. 4, pp. 2622–2625, Oct. 1999.

[23] D. S. Naik, C. G. Peterson, A. G. White, A. J. Berglund, and P. G. Kwiat, *Phys. Rev. Lett.*, vol. 84, no. 20, pp. 4733–4736, May 2000.

[24] D. Bouwmeester, J.-W. Pan, K. Mattle, M. Eibl, H. Weinfurter, and A. Zeilinger, *Nature*, vol. 390, no. 6660, pp. 575–579, Dec. 1997.

[25] X. S. Ma, T. Herbst, T. Scheidl, D. Wang, S. Kropatschek, W. Naylor, B. Wittmann, A. Mech, J. Kofler, E. Anisimova, V. Makarov, T. Jennewein, R. Ursin, and A. Zeilinger, *Nature*, vol. 489, no. 7415, pp. 269–273, Sep. 2012.

[26] W. Wieczorek, R. Krischek, N. Kiesel, P. Michelberger, G. Tóth, and H. Weinfurter, *Phys. Rev. Lett.*, vol. 103, no. 2, p. 020504, Jul. 2009.

[27] X.-C. Yao, T.-X. Wang, P. Xu, H. Lu, G.-S. Pan, X.-H. Bao, C.-Z. Peng, C.-Y. Lu, Y.-A. Chen, and J.-W. Pan, *Nat. Photonics*, vol. 6, no. 4, pp. 225–228, Apr. 2012.

[28] F. Jelezko and J. Wrachtrup, Single defect centres in diamond: A review, *Physica Status Solidi (A) Applications and Materials Science*, vol. 203, no. 13. pp. 3207–3225, Oct-2006.

[29] H. Hanzawa, N. Umemura, Y. Nisida, and H. Kanda, *Phys. Rev. B - Condens. Matter Mater. Phys.*, vol. 54, no. 6, pp. 3793–3799, Aug. 1996.

[30] R. Brouri, A. Beveratos, J.-P. Poizat, and P. Grangier, *Opt. Lett.*, vol. 25, no. 17, p. 1294, Sep. 2000.

[31] C. Kurtsiefer, S. Mayer, P. Zarda, and H. Weinfurter, *Phys. Rev. Lett.*, vol. 85, no. 2, pp. 290–293, Jul. 2000.

[32] P. R. Dolan, S. Adekanye, A. A. P. Trichet, S. Johnson, L. C. Flatten, Y. C. Chen, L. Weng, D. Hunger, H.-C. Chang, S. Castelletto, and J. M. Smith., *Opt. Express*, vol. 26, no. 6, p. 7056, Mar. 2018.

[33] N. Mizuochi, T. Makino, H. Kato, D. Takeuchi, M. Ogura, H. Okushi, M. Nothaft, P. Neumann, A. Gali, F. Jelezko, J. Wrachtrup, and S. Yamasaki, *Nat. Photonics*, vol. 6, no. 5, pp. 299–303, May 2012.

[34] E. Togan, Y. Chu, A. S. Trifonov, L. Jiang, J. Maze, L. Childress, M. V. G. Dutt, A. S. Sørensen, P. R. Hemmer, A. S. Zibrov, and M. D. Lukin, *Nature*, vol. 466, no. 7307, pp. 730–734, Aug. 2010.

[35] P. Neumann, N. Mizuochi, F. Rempp, P. Hemmer, H. Watanabe, S. Yamasaki, V. Jacques, T. Gaebel, F. Jelezko, and J. Wrachtrup, *Science*, vol. 320, no. 5881, pp. 1326–1329, Jun. 2008.

[36] G. Juska, E. Murray, V. Dimastrodonato, T. H. Chung, S. T. Moroni, A. Gocalinska, and E. Pelucchi, *J. Appl. Phys.*, vol. 117, no. 13, p. 134302, Apr. 2015.

[37] D. Leonard, M. Krishnamurthy, C. M. Reaves, S. P. Denbaars, and P. M. Petroff, *Appl. Phys. Lett.*, vol. 63, no. 23, pp. 3203–3205, Dec. 1993.

[38] T. Mano, K. Watanabe, S. Tsukamoto, N. Koguchi, H. Fujioka, M. Oshima, C.-D. Lee, J.-Y. Leem, H. J. Lee, and S. K. Noh, *Appl. Phys. Lett.*, vol. 76, no. 24, p. 3543, Jun. 2000.

[39] C. Heyn, A. Stemmann, M. Klingbeil, C. Strelow, T. Köppen, S. Mendach, and W. Hansen, *J. Cryst. Growth*, vol. 323, no. 1, pp. 263–266, May 2011.

[40] C. Heyn, T. Bartsch, S. Sanguinetti, D. Jesson, and W. Hansen, *Nanoscale Res. Lett.*, vol. 10, no. 1, p. 67, Dec. 2015.

[41] D. Huber, M. Reindl, Y. Huo, H. Huang, J. S. Wildmann, O. G. Schmidt, A. Rastelli, and R. Trotta, *Nat. Commun.*, vol. 8, p. 15506, May 2017.

[42] P. Michler, A. Kiraz, C. Becher, W. V Schoenfeld, P. M. Petroff, L. Zhang, E. Hu, and A. Imamoglu, *Science*, vol. 290, no. 5500, pp. 2282–5, Dec. 2000.

[43] N. Akopian, N. H. Lindner, E. Poem, Y. Berlatzky, J. Avron, D. Gershoni, B. D. Gerardot, and P. M. Petroff, *Phys. Rev. Lett.*, vol. 96, no. 13, p. 130501, Apr. 2006.

[44] R. J. Young, R. M. Stevenson, P. Atkinson, K. Cooper, D. A. Ritchie, and A. J. Shields, *New J. Phys.*, vol. 8, no. 2, pp. 29–29, Feb. 2006.

[45] C. L. Salter, R. M. Stevenson, I. Farrer, C. A. Nicoll, D. A. Ritchie, and A. J. Shields, *Nature*, vol. 465, no. 7298, pp. 594–597, 2010.

[46] C. Santori, D. Fattal, J. Vučković, G. S. Solomon, and Y. Yamamoto, *Nature*, vol. 419, no. 6907, pp. 594–597, Oct. 2002.

[47] N. Somaschi, V. Giesz, L. De Santis, J. C. Loredo, M. P. Almeida, G. Hornecker, S. L. Portalupi, T. Grange, C. Antón, J. Demory, C. Gómez, I. Sagnes, N. D. Lanzillotti-Kimura, A. Lemaítre, A. Auffeves, A. G. White, L. Lanco, and P. Senellart, *Nat. Photonics*, vol. 10, no. 5, pp. 340–345, May 2016.

[48] H. J. Krenner, M. Sabathil, E. C. Clark, A. Kress, D. Schuh, M. Bichler, G. Abstreiter, and J. J. Finley, *Phys. Rev. Lett.*, vol. 94, no. 5, p. 057402, Feb. 2005.

[49] Y. H. Huo, B. J. Witek, S. Kumar, J. R. Cardenas, J. X. Zhang, N. Akopian, R. Singh, E. Zallo, R. Grifone, D. Kriegner, R. Trotta, F. Ding, J. Stangl, V. Zwiller, G. Bester, A. Rastelli, and O. G. Schmidt, *Nat Phys*, vol. 10, no. 1, pp. 46–51, Jan. 2014.

[50] R. J. Young, R. M. Stevenson, A. J. Shields, P. Atkinson, K. Cooper, D. A. Ritchie, K. M. Groom, A. I. Tartakovskii, and M. S. Skolnick, *Phys. Rev. B - Condens. Matter Mater. Phys.*, vol. 72, no. 11, p. 113305, Sep. 2005.

[51] A. Boretti, L. Rosa, A. Mackie, and S. Castelletto, *Adv. Opt. Mater.*, vol. 3, no. 8,

pp. 1012–1033, Aug. 2015.

[52] C. L. Salter, R. M. Stevenson, I. Farrer, C. A. Nicoll, D. A. Ritchie, and A. J. Shields, *Nature*, vol. 465, no. 7298, pp. 594–597, Jun. 2010.

[53] G. S. Solomon, M. Pelton, and Y. Yamamoto, *Phys. Rev. Lett.*, vol. 86, no. 17, pp. 3903–3906, Apr. 2001.

[54] R. Trotta, E. Zallo, C. Ortix, P. Atkinson, J. D. Plumhof, J. Van Den Brink, A. Rastelli, and O. G. Schmidt, *Phys. Rev. Lett.*, vol. 109, no. 14, p. 147401, Oct. 2012.

[55] W. Unrau, D. Quandt, J.-H. Schulze, T. Heindel, T. D. Germann, O. Hitzemann, A. Strittmatter, S. Reitzenstein, U. W. Pohl, and D. Bimberg, *Appl. Phys. Lett.*, vol. 101, no. 21, p. 211119, Nov. 2012.

[56] A. J. Shields, *Nat. Photonics*, vol. 1, no. 4, pp. 215–223, Apr. 2007.

[57] L. Francaviglia, Y. Fontana, and A. Fontcuberta i Morral, Quantum Dots in Nanowires, in *Semiconductors and Semimetals*, vol. 94, Elsevier, 2016, pp. 159–184.

[58] J. Claudon, J. Bleuse, N. S. Malik, M. Bazin, P. Jaffrennou, N. Gregersen, C. Sauvan, P. Lalanne, and J. M. Gérard, *Nat. Photonics*, vol. 4, no. 3, pp. 174–177, Mar. 2010.

[59] M. A. M. Versteegh, M. E. Reimer, K. D. Jöns, D. Dalacu, P. J. Poole, A. Gulinatti, A. Giudice, and V. Zwiller, *Nat. Commun.*, vol. 5, no. 1, p. 5298, Dec. 2014.

[60] J. Claudon, N. Gregersen, P. Lalanne, and J.-M. Gérard, *ChemPhysChem*, vol. 14, no. 11, pp. 2393–2402, Aug. 2013.

[61] A. W. Elshaari, I. E. Zadeh, A. Fognini, M. E. Reimer, D. Dalacu, P. J. Poole, V. Zwiller, and K. D. Jöns, *Nat. Commun.*, vol. 8, no. 1, p. 379, Dec. 2017.

[62] L. O. Mereni, V. Dimastrodonato, R. J. Young, and E. Pelucchi, *Appl. Phys. Lett.*, vol. 94, no. 22, p. 223121, Jun. 2009.

[63] M. H. Baier, E. Pelucchi, E. Kapon, S. Varoutsis, M. Gallart, I. Robert-Philip, and I. Abram, *Appl. Phys. Lett.*, vol. 84, no. 5, pp. 648–650, Feb. 2004.

[64] G. Juska, Pyramidal Quantum Dots: single and entangled photon sources and correlation studies, Thesis, University College Cork, 2013.

[65] G. Juska, V. Dimastrodonato, L. O. Mereni, A. Gocalinska, and E. Pelucchi, *Nat. Photonics*, vol. 7, no. 7, pp. 527–531, May 2013.

[66] S. T. Moroni, V. Dimastrodonato, T.-H. Chung, G. Juska, A. Gocalinska, D. D. Vvedensky, and E. Pelucchi, *J. Appl. Phys.*, vol. 117, no. 16, p. 164313, Apr. 2015.

[67] F. Lelarge, C. Constantin, K. Leifer, A. Condo, V. Iakovlev, E. Martinet, A. Rudra, and E. Kapon, *Appl. Phys. Lett.*, vol. 75, no. 21, pp. 3300–3302, 1999.

[68] T. H. Chung, G. Juska, S. T. Moroni, A. Pescaglini, A. Gocalinska, and E. Pelucchi, *Nat. Photonics*, vol. 10, no. 12, pp. 782–787, Oct. 2016.

[69] S. T. Moroni, T. H. Chung, G. Juska, A. Gocalinska, and E. Pelucchi, *Appl. Phys. Lett.*, vol. 111, no. 8, p. 083103, Aug. 2017.

[70] N. H. Lindner and T. Rudolph, *Phys. Rev. Lett.*, vol. 103, no. 11, p. 113602, Sep. 2009.

[71] I. Schwartz, D. Cogan, E. R. Schmidgall, Y. Don, L. Gantz, O. Kenneth, N. H. Lindner, and D. Gershoni, *Science*, vol. 354, no. 6311, pp. 434–437, Oct. 2016.

[72] S. T. Moroni, S. Varo, G. Juska, T. H. Chung, A. Gocalinska, and E. Pelucchi, *J. Cryst. Growth*, vol. 506, pp. 36–39, Jan. 2019.

[73] J. Zhang, J. S. Wildmann, F. Ding, R. Trotta, Y. Huo, E. Zallo, D. Huber, A. Rastelli, and O. G. Schmidt, *Nat. Commun.*, vol. 6, p. 10067, Dec. 2015.

[74] R. Trotta, J. Martín-Sánchez, J. S. Wildmann, G. Piredda, M. Reindl, C. Schimpf, E. Zallo, S. Stroj, J. Edlinger, and A. Rastelli, *Nat. Commun.*, vol. 7, p. 10375, Jan. 2016.

[75] V. Dimastrodonato, Epitaxy and growth mechanisms of site-controlled nanostructures, Thesis, University College Cork, 2011.

Chapter 2
Pyramidal quantum dot fabrication and experimental techniques

Pyramidal quantum dots (PQDs) are a site-controlled system where each micron-sized pyramid can contain exactly one quantum dot layer (or one multi-quantum dot structure intentionally designed for). This property and its technological advantage, compared to other quantum dot systems, come at a price in terms of complexity in the fabrication and processing of devices. Different types of PQD-based devices require different fabrication steps, depending on the purpose of the specific sample. In all cases, PQDs are fabricated starting from a (111)B-oriented GaAs substrate, which is patterned to form an ordered array of pyramidal recesses. A quantum-well-like multilayer structure is then deposited by means of Metalorganic Vapour-Phase Epitaxy (MOVPE), the whole process granting a uniform result in terms of PQD structural properties across the substrate. After the growth, different types of processing can be employed, the most "basic" and most often employed being the *back-etching* of the original GaAs substrate, typically used for samples meant for optical characterization only. Other procedures depend on the application: PIN diode devices require selective area contacting strategies; piezoelectric-cells-based devices need to be bonded using a polymer; lift-off techniques for the full pyramidal structure allow for its manipulation and transfer. All these processing and fabrication techniques will be reviewed in this chapter.

The PQD optical characterization was performed by means of well-established techniques in the study of quantum dots, auto- and cross-correlations being the key methods to unveil the quantum nature of the emitted light. A low-temperature

micro-photoluminescence setup was employed to carry out all the optical characterization of the samples presented in the thesis. The specifications of the cryostat, excitation and spectroscopy system will be summarized in the following. The cross-correlation system will also be briefly described together with the analysis techniques allowed by the integrated system and software.

2.1 Substrate preparation-patterning

First we will detail the steps of the pre-patterning of the GaAs substrate to form the inverted pyramidal recesses, which can be realized by conventional photolithography and chemical wet etching [1] (Fig.1). The pyramidal recesses are organized in an ordered array where the pitch and side lengths can take different measures. This is defined in the first place by the mask used for the photolithography. Initially a layer of SiO_2 is sputtered on a semi-insulating (SI) GaAs (111)B substrate. Hexamethyldisilazane (HMDS, adhesion promoter for the resist) and S1805 positive photoresist (PR) (Dow Electronic Materials) are spun in sequence on top of the SiO_2-coated GaAs, which will act as photo-sensitive layer. UV exposure is carried out by a Karl Süss MA6 mask aligner, followed by development by means of MF 319 (Dow Electronic Materials), which removes the resist exposed to UV only, defining a hexagonally-arranged array of triangles with the selected pitch and size. Exposure and development times are typically around 4 s and 25 s respectively, depending on the lamp condition. To prevent the residual PR from interfering with the following pattern-transfer step and from contaminating the GaAs surface which will be exposed, the procedure includes a 2-minute treatment in an oxygen plasma chamber. Subsequently, the triangular pattern is transferred to the SiO_2 layer by etching in buffered oxide etchant (BOE) for 10 s, followed by PR stripping by acetone and isopropanol (IPA) warm bath.

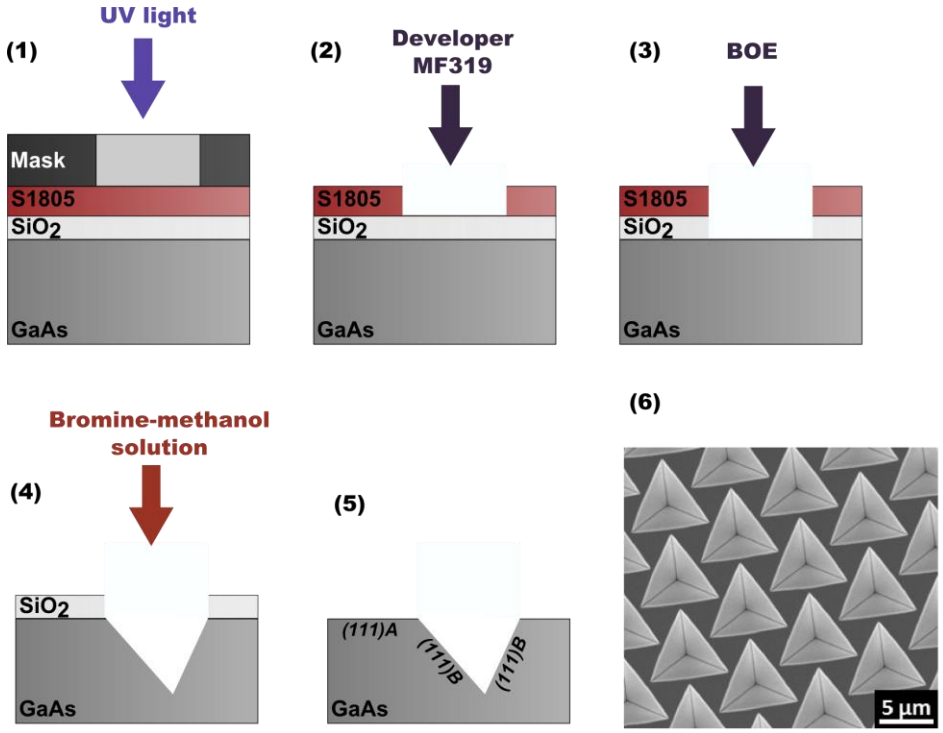


Fig.1: Processing steps for the pre-patterning of GaAs substrates (1-5) and final result (6, SEM image)

The following step determines the formation of the recesses by chemical etching: a 5% Br in methanol solution is prepared and the SiO_2-masked GaAs is dipped into it for a time which depends on the required size of the recesses. This etchant solution selectively etches along three (111)A-oriented surfaces, naturally turning the triangle-shaped mask into a tetrahedron-shaped recess. As a reference example, we report the case of the 7.5 µm pitch, for which the typical etching time is ~8 s. After further cleaning of the residual PR in acetone and IPA, SiO_2 removal is performed by etching in BOE for 5 minutes. Finally, the pre-patterned substrates are cleaned by oxygen plasma, followed by the removal of the residual native oxide from the processed GaAs surface by means of exposure to a 48 % Hydroflouric (HF) acid solution until the surface becomes "hydrophobic", typically for 3 minutes (note that here "hydrophobic" simply relates to a change in apparent water adhesion, with a strong tendency to "slide away") [2].

2.2 MOVPE deposition

The critical step in the fabrication of PQDs is the MOVPE deposition. MOVPE makes use of metalorganic precursors for group-III and of gaseous hydrides for group-V species (respectively trimethylgallium, trimethylaluminium, trimethylindium for group-III and arsine or phosphine for group-V) which are carried by a carrier gas (here nitrogen) into the deposition reactor through a laminar flow, necessary for a uniform and reproducible deposition. The rotation speed of the satellite (~70rpm) establishes a uniform boundary layer over the substrate, through which the precursors diffuse. The overall MOVPE process is relatively intricate: the precursors interact with the surface of the substrate in a complex mechanism of adsorption and migration, decomposing and finally releasing the single adatoms of the group-III and -V species. These diffuse on the surface and become adsorbed and migrate until incorporation. The growth is strongly dependent on the complex interplay between several parameters: among all, temperature and pressure are essential parameters, as well as the V/III precursor ratio. All samples presented in this work have been grown in a *mass-transport limited* regime, where the substrate temperature is kept between 550°C and 800°C at a pressure of 20 mbar and with a high V/III ratio (>500). In this regime the surface kinetics of the precursor decomposition is fast and the deposition rates are essentially determined by the amount of precursors that is sent on the surface of the substrate, while the high V/III ratio regulates the diffusion lengths of the group-III precursors as well, making their incorporation quicker. The growth conditions influence particularly the growth over non-planar substrates, where the competition between differently oriented facets in both terms of precursor decomposition and adatom diffusion causes a *growth rate anisotropy* (GRA), i.e. different growth rates on differently oriented facets. The GRA plays a critical role in the determination of the size and composition of the nanostructures grown on a non-planar substrate.

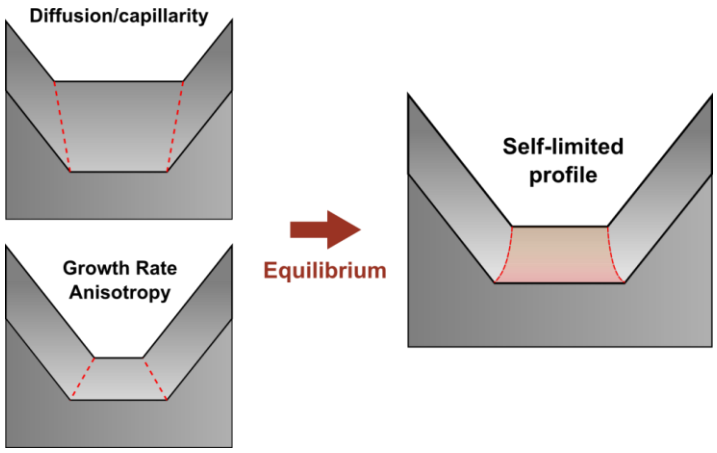


Fig.2: Schematic cross-section representation of the effect of the Growth Rate Anisotropy and of diffusion/capillarity on the evolution of the growth profile in PQDs and of the stationary regime where the self-limited profile is reached.

In the case of the growth on pyramidal recesses, the interplay between the (111)B top surface and the three lateral (111)A facets of the recess on the precursor decomposition causes the growth to happen only inside the recess [3] (in well-established temperature and pressure conditions). The bottom of a pyramidal recess is never perfectly sharp, as a small (less than 100nm) base (111)B facet is always present. During the growth the bottom profile of the pyramidal recess evolves, led mainly by two competing processes: the **GRA** and the **diffusion** of the adatoms after the decomposition of the precursors (Fig.2). The first tends to favor the growth on the sidewalls, therefore shrinking the bottom (111)B facet; the latter (usually referred to as *capillarity* effect, if seen from a thermodynamic point of view) leads to a net diffusion of adatoms towards the bottom facet therefore leading to an increase in its lateral size. After a transient phase, during which the profile of the surface evolves, a stationary regime is generally reached, the resulting profile being referred to in the literature as “self-limiting profile” (SLP). The self-limiting mechanism in principle allows to always obtain the same shape and dimensions of the growth profile, after

enough deposition time, for a given set of growth parameters, and therefore is a key element for reproducibility.

The geometry of the pyramidal recess gives rise to a number of nanostructures [4] (Fig.3): for instance, when InGaAs is deposited in between GaAs, it originates three lateral quantum wells (LQWs) along the faces of the pyramid, three lateral quantum wires (LQWRs) along the edges of the pyramid and a quantum dot at the tip. *Segregation* phenomena also take place during the deposition, resulting in more nanostructuring. Whenever an alloy is deposited on a non-planar substrate, the more diffusive specie diffuses towards (away from) concave (convex) regions with higher (lower) probability, forming a higher (lower) concentration region. Importantly, when AlGaAs is deposited in a pyramidal recess, a Ga-rich vertical quantum wire (VQWR) forms in the very centre of the structure due to Ga segregation effects. It should also be said that recently, newly reported corner QDs (CQDs) were observed, generated during the QD layer growth as independent nanostructures from the QD, and located

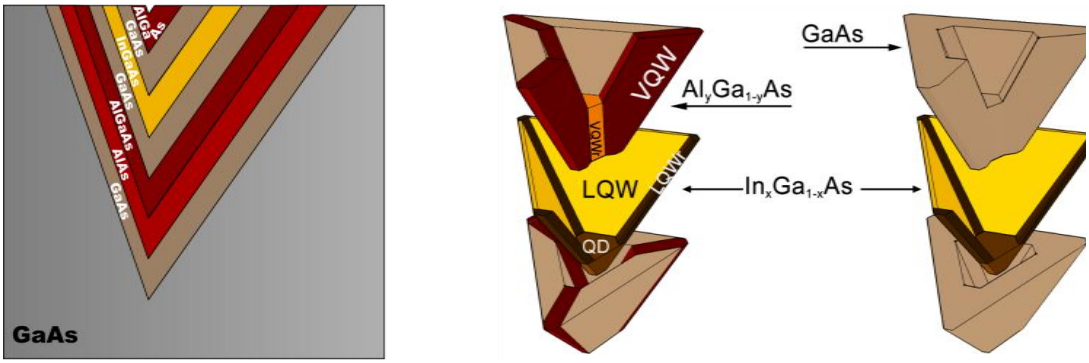


Fig.3: on the left, schematic representation (not in scale) of the sequence of layers in a typical PQD MOVPE deposition for optical excitation; the layer deposition sequence starts from the "bottom" layer, up to the closest to the surface; on the right, schematic representation of the nanostructures forming inside a pyramidal recess when a typical sequence of layers (as per the scheme on the left) is deposited on it: quantum dot (QD), lateral quantum wires (LQWRs), lateral quantum wells (LQWs), vertical quantum wires (VQWRs), vertical quantum wells (VQWs).

somewhere at the top of the corners of the pyramidal recesses, as reported in [5].

A typical structure for MOVPE-grown PQDs is made of several layers with different functionalities (Fig3). First, a buffer GaAs layer is grown on the top of the pyramidal recess: it acts as a "spacer" between the pyramidal structure and eventual defects forming at the etched surface because of the imperfect fabrication chemical processes, which might affect negatively the quality of the optical properties of the QD. Secondly, an etch-stop layer is needed in order to allow for the chemical removal of the original GaAs substrate and at the same time leave the pyramidal structure unharmed. An $Al_{0.8}Ga_{0.2}As$ layer is needed to apply back-etching techniques, while an AlAs layer is preferred for pyramid lift-off techniques (as it will be described later in this chapter). Then the actual structure of the PQDs is deposited. A few nm thick InGaAs QD layer is deposited in between GaAs barriers to allow for the confinement. Originally a pair of low-Al-content AlGaAs barriers was included in the structure in order to allow a better confinement of the carriers in the InGaAs/GaAs QD region. In more recent PQD growth this barrier was shown to have little effect on the quality of the QDs and removed for optically excited PQDs.

In the case of LED PIN devices, doped regions were defined by the introduction of doping: carbon as p-dopant and silicon as n-dopant. These are introduced in the reactor in the form of tetrabromomethane (CBr_4) and disilane (Si_2H_6), co-flowing with the other precursors.

2.3 Bonding techniques

In order to extract light from the backetched PQDs it is always necessary to transfer the substrate containing them onto a supportive/functional substrate, as light extraction in "as grown" geometry is very inefficient. Different bonding techniques need to be employed depending on the functionality of the substrate. The main

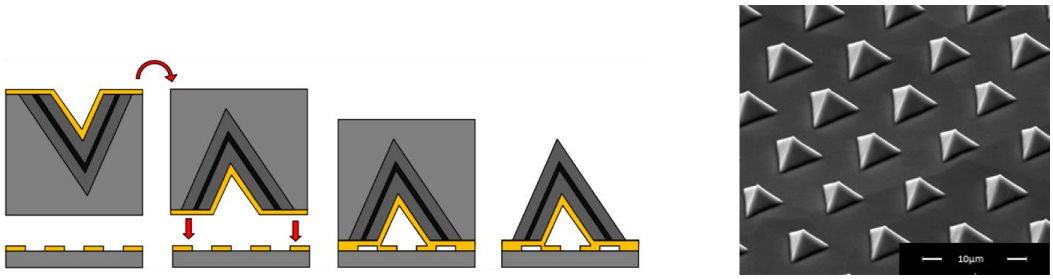


Fig.4: on the left, representation of the back-etching via bonding and chemical etching of the original GaAs substrate, revealing the pyramidal structure; on the right, SEM image of back-etched PQDs.

requirements for the bonding are generally two: being solid enough to sustain mechanical stress given by the following mechanical grinding step and being suitable for cooling to cryogenic temperatures, in terms of both mechanical stability and heat transfer capabilities (Fig.4).

2.1.1. Au-AuSn-Au reflow bonding

The most basic PQD device simply requires the as-grown sample to be bonded onto a supportive plain (100) GaAs substrate, which will permit to mechanically support and handle a thin layer containing the back-etched pyramids. This can be done by first evaporating a thick (200 nm) gold layer on both the supportive substrate and the top surface of the as-grown sample. Then a Au-to-SnAu reflow process is employed: the GaAs substrate is heated up to 250°C after a 10µm-thick Au-Sn foil is placed on it and finally the as-grown substrate is placed on the top of it on the Au-evaporated side and pressed while the temperature is raised above 280°C (320°C as a target) to allow for the melting and bonding of the gold and the AuSn foil. This type of bonding is used for samples that need standard optical characterization, due to the relatively simple and reliable bonding procedure, and samples which require electrical contacting for the back of the pyramidal structure

2.1.2. SU8 bonding

If a strain transfer from a piezoelectric substrate to the PQDs is required, the Au-AuSn-Au bonding would not be ideal. In fact it adds an over 10µm-thick layer between the piezoelectric cell and the sample, which is also always not perfectly flat after the bonding but typically shows a tilt, making the strain transfer less effective. A different approach, which has been originally proposed and applied for example in [6], is based on the use of a polymer, SU8, which can form extremely thin layers (down to 500nm) by spin-coating techniques and form a solid bond between the two substrates. SU8, which is mainly used in the form of a photo-resist (therefore mixed with solvents), needs to be spun over the bonding substrate at a speed of 4000rpm, then heated up to 90°C on a hotplate to evaporate solvents in the SU8-based solution. A Finetech flip-chip bonding machine is employed to bond the as-grown PQD sample onto the SU8-spun substrate, allowing for a very good parallelism between the sample and the bonding substrate. Once the membrane has been put in contact with the substrate and a pressure of the order of 10kPa is applied, it is heated up to 180 degrees for 15 minutes to cure the SU8 above the glass-transition temperature and ensure a mechanically stable bond.

2.4 Mechanical thinning and back-etching

Once the membrane containing the PQDs has been transferred onto a supporting/functional substrate, the pyramids need to be uncovered from the original GaAs growth substrate. This can be done by first employing a grinder (Logitech PM5) to mechanically thin down the sample from the back side and remove most of the GaAs down to a few tens of microns of total thickness. This will speed up

the process compared to an all-wet chemical etching process. Successively the residual GaAs covering the pyramids is removed by wet etching techniques. An ammonium hydroxide in hydrogen peroxide solution with a PH of 8.7 is used to slowly etch the residual GaAs. Thanks to the high etching selectivity of the solution, the integrity of the pyramidal structure is preserved by inserting an etch-stop layer, such as a high-Al AlGaAs or AlAs, which will be etched extremely slowly compared to GaAs [7]. Successive etching in hydrochloric acid (HCl, 30% solution in water) for a few seconds only can be employed to remove eventual residuals of oxide forming on the surface of the sample after the previous etching step.

2.5 LED fabrication

As it has been anticipated, the structure of a PQD-based LED is composed of doped layers, but also extra layers were included to allow selective injection of the quantum dot, as it will be shown later in the thesis. The typical structure of a PQD-LED in the apex-up configuration after the processing is completed is shown in Fig.5: first the usual GaAs buffer layer is grown, followed by an $Al_{0.45}GaAs$ to $Al_{0.8}GaAs$ graded layer and an $Al_{0.8}GaAs$ layer acting as etch-stop; these two layers are already p-doped and are followed by a further $Al_{0.55}GaAs$ p-doped layer; the intrinsic region is deposited afterwards, made of an $In_{0.25}GaAs$ QD layer embedded into GaAs barriers and $Al_{0.75}GaAs$ outer barriers; finally a n-doped $Al_{0.3}GaAs$ layer is deposited.

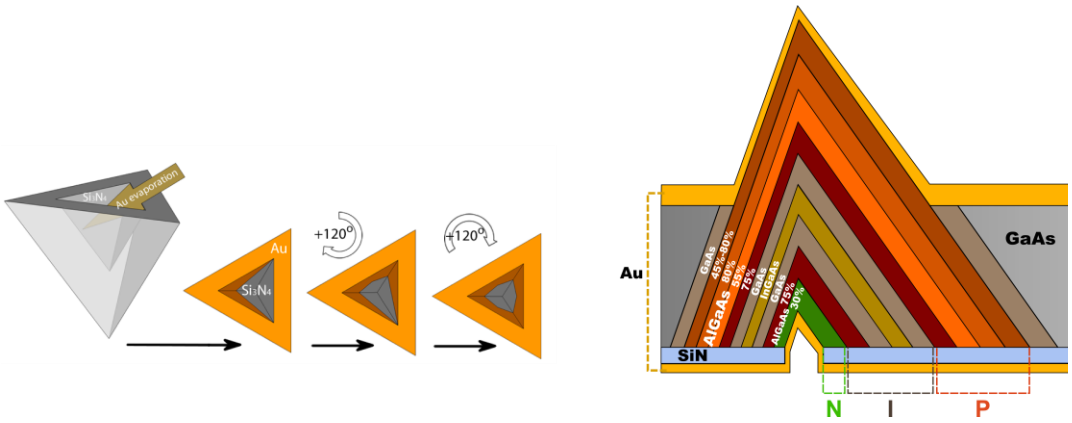


Fig.5: On the left: representation of the 3-times tilted Au evaporation to form a mask for the underlying Si_3N_4; on the right: sketch of the cross-section of a PQD-based LED, where the N-, I- and P-doped regions are highlighted in green, brown and orange respectively.

In the case of the fabrication of an LED device, additional fabrication steps are required. After MOVPE deposition a small recess is usually left on each pyramid. The recess can be a source of short-circuit of the device (for instance this happens at the ridges of the recess) but its geometry can be exploited to perform a proper insulation of the ridges and safe contacting of the n-doped layer. As a first step PECVD is performed to deposit 300nm of Si_3N_4 insulating layer. A three times thin Ti-Au (3nm-15nm) evaporation is then carried out in a thermal evaporator (Moorefield) keeping the sample tilted with an angle of 60°, in order to create a mask which covers the ridge of the pyramidal recess (Fig.5). Now the Si_3N_4 can be selectively removed from the bottom of the recess by CF_4 plasma, followed by a 20nm-200nm-thick Ti-Au evaporation (typically in a Moorefield e-beam evaporator) to contact the exposed n-doped layer only.

The next steps of the processing follow the procedure explained in the previous paragraph for the mechanical thinning and back-etching of the pyramids. The bonding of the sample onto a Au-coated supportive GaAs piece allows for the contacting of the n-side by connecting the exposed gold of the supportive GaAs with our power supply. The p-side still needs to be contacted; when the AlGaAs/AlAs etch-

stop layer is exposed after the back-etching, it is let in contact with air and partially oxidized, therefore the oxide layer is removed by means of HCl (30% solution in water). At this stage the p-doped layer is exposed and a contacting thin semi-transparent Ti-Au layer (typically 5nm-25nm) can be evaporated onto it. It is important to note that this relatively simple fabrication scheme results in a simultaneous contacting of all the pyramids at the same time in parallel. Both p- and n-side contacts are connected to the power supply by means of kapton-insulated wiring, fixed onto the sample with silverpaint.

2.6 Lift-off techniques for Pyramidal Quantum Dots

The insertion of an AlAs layer in place of the usual AlGaAs etch-stop layer can act as a sacrificial layer for the release of the pyramidal structure from the original growth substrate. In fact, hydrofluoric acid (HF) is strongly selective in the etching of AlAs versus GaAs and low-Al AlGaAs. An AlAs layer with a thickness of a few tens of nm can be selectively removed by exposing the sample to 30% concentrated HF for at least 1 minute. Rinse in DI water and Nitrogen blow following, the pyramids can be extracted from the substrate by means of a number of methods, which will be reviewed in Chap.9.

2.7 Cryogenic MicroPL measurements

The optical characterization of the samples is performed in a standard micro-photoluminescence set-up. A low vibration, helium-based semi-closed-cycle cryostat (cold finger) allows to reach a minimum temperature of 8K. The thermal contact of the sample onto the cooled copper stage is a critical step for the good outcome of the cooling process, implying the use of thermal paste (either Ag-based paint or silicone-

based paste). The chamber is evacuated by using a standard mechanical and turbo pump, down to a pressure of the order of 10^{-6}mbar while the cooling process is started.

A single objective (typically 50X magnification, with a numerical aperture of 0.42 and few mm working distance) is used to excite the QD and collect its emission in a confocal arrangement. The laser source for non-resonant excitation of the QDs is a laser diode (PicoQuant LDH-D-C-635M, λ=635nm) capable of operating in continuous-wave (cw) and pulsed mode (full width at half maximum of about 100 ps). The laser beam is focused on the sample to a spot smaller than the area of a single pyramid (1-2 μm), enabling the addressing of single PQDs, the typical laser excitation power focused on the sample being a few microwatts (50-200 nW/μm2). A cubic beamsplitter (70/30) introduced into the optical axis is the key element of the confocal configuration: 30% of the initial laser excitation power is sent and focused unto the sample, while 70% of the emission from a QD is sent to the spectrometer upon reflection at the beamsplitter; the remaining laser light is filtered by a long-pass filter. A Keithley 2410 1100V SourceMeter, instead, allowed performing electrical excitation of the LED devices, a feedthrough mount leading insulated cables into the cryostat. Higher DC voltage can be applied to piezoelectric devices through the same feedthrough, generated by an Iseg EBS 8030 high voltage (up to ±3kV) power supply.

A collimated beam of the emission is then focused to the entrance slit of the spectrometer equipped with a charge-coupled device (CCD). A red LED is used to illuminate the sample for the system aligning and imaging purposes, introduced in the optical axis by means of a removable glass beamsplitter before the main cubical beamsplitter. A second removable beamsplitter allows to send the image of the surface of the sample to a video capture device in order to achieve simultaneous live imaging of the surface and detection of the photoluminescence while looking for a possible candidate for the measurement. The objective is mounted onto an XYZ movable stage, operated by piezoelectric stepper motors, which are used to scan

over the surface of the sample and move from one PQD to the next. After finding the position of interest, the imaging beamsplitter can be removed to increase the collection efficiency and perform the actual measurement. Polarization resolved measurements of the spectra are performed to study the fine structure splitting (FSS): a half-wave retardation plate and a linear polarizer are placed sequentially in the optical axis of the system. The FSS can be typically recognized as a sinusoidal oscillation of the exciton and biexciton energies following a counter-phase oscillation while changing polarization angle. The value of the FSS can be obtained by subtracting the corresponding biexciton positions from the exciton therefore eliminating systematic errors, coming for example from misalignments of the optical axis or excitation-dependent effects under drifting of the sample due to residual vibrations or temperature instabilities. The amplitude of the resulting sinusoid corresponds to two times the FSS.

2.8 Correlating system

Time-correlation of the detection events from different transitions is an essential tool to understand the recombination dynamics and the relationship between different cascades, nonetheless to demonstrate the emission of non-classical light. Time-correlated single photon counting (TCSPC) is one of the most employed techniques to analyze photoluminescence kinetics, especially when the light level is very low and high resolution (on the order of picoseconds) is required. The set-up used in this work is based on our micro-photoluminescence set-up, where the light is sent to a monochromator which acts as a tunable, narrow band-pass filter: the light dispersed by one of the gratings is directed by a lateral mirror towards the side exit slit which selects a desirable wavelength and resolution. The light transmitted through each

monocrhomator is coupled to a multimode fiber attached to an avalanche photodiode, which is interfaced with the TCSPC module.

Firstly, TCSPC is employed for the measurement of lifetimes upon periodic pulsed excitation of the sample and subsequent emission of photons, each detection event being collected, the laser reference time subtracted to it and (upon multiple excitations) used to build the histogram representing the probability of detection vs time, i.e. the intensity decay profile of the observed transition. The minimum time resolution of our TCSPC system is a few picoseconds, which is the minimum achievable width of the time-bin. The electrical pulse generated by the photodetector (silicon avalanche photodiode in our case) is connected to the "START" channel of the correlating system while the reference electric TTL signal from the laser is used as a "STOP" signal: this reverse START-STOP configuration allows to discard excitation pulse events which do not correspond to a detection of the generated photon (caused mainly by a low extraction efficiency) and to avoid therefore "wasted" detector dead times.

In order to perform auto- and cross- correlations, a classical Hanbury Brown and Twiss (HBT) setup is employed: it is enough to introduce a 50:50 BS on the optical path which splits the signal from the sample in two beams which are sent to two identical monochromators. By selecting the same wavelength one can perform an auto-correlation: the light from each of the monochromators is sent to two APDs, one connected to the START and the other to the STOP channel of the TSCPS (Becker & Hickel SPC-134, four channels). By selecting different wavelength and therefore different transitions, one can perform cross-correlations, instead. The histogram, constructed from the measured time intervals between the start and stop signals, mimics the second order correlation function. If polarization-resolved measurements are required, a polarizer or polarizing beamsplitter can be placed in front of the APDs. The set-up is equipped with 4 APDs, thus four curves can be measured simultaneously.

References

[1] S. Watanabe, E. Pelucchi, B. Dwir, M. H. Baier, K. Leifer, and E. Kapon, *Appl. Phys. Lett.*, vol. 84, no. 15, pp. 2907–2909, Apr. 2004.

[2] A. Gocalinska, K. Gradkowski, V. Dimastrodonato, L. O. Mereni, G. Juska, G. Huyet, and E. Pelucchi, *J. Appl. Phys.*, vol. 110, no. 3, p. 034319, Aug. 2011.

[3] E. Pelucchi, V. Dimastrodonato, A. Rudra, K. Leifer, E. Kapon, L. Bethke, P. A. Zestanakis, and D. D. Vvedensky, *Phys. Rev. B*, vol. 83, no. 20, p. 205409, May 2011.

[4] Q. Zhu, E. Pelucchi, S. Dalessi, K. Leifer, M.-A. Dupertuis, and E. Kapon, *Nano Lett.*, vol. 6, no. 5, pp. 1036–1041, May 2006.

[5] G. Juska, V. Dimastrodonato, L. O. Mereni, T. H. Chung, A. Gocalinska, E. Pelucchi, B. Van Hattem, M. Ediger, and P. Corfdir, *Phys. Rev. B*, vol. 89, no. 20, p. 205430, May 2014.

[6] J. Martín-Sánchez, R. Trotta, A. Mariscal, R. Serna, G. Piredda, S. Stroj, J. Edlinger, C. Schimpf, J. Aberl, T. Lettner, J. Wildmann, H. Huang, X. Yuan, D. Ziss, J. Stangl, and A. Rastelli, *Semicond. Sci. Technol.*, vol. 33, no. 1, p. 013001, Jan. 2018.

[7] Y. Uenishi, H. Tanaka, and H. Ukita, *IEEE Trans. Electron Devices*, vol. 41, no. 10, pp. 1778–1783, 1994.

Chapter 3
Indium segregation during III-V quantum wire and quantum dot formation on patterned substrates

Chapter based on the published journal article:

Journal of Applied Physics 117, 164313 (2015)

Stefano T. Moroni[1], Valeria Dimastrodonato[1], Tung-Hsun Chung[1], Gediminas Juska[1], Agnieszka Gocalinska[1], Dimitri D. Vvedensky[2], and Emanuele Pelucchi[1]

[1]*Tyndall National Institute, "Lee Maltings", University College Cork, Cork, Ireland*

[2]*The Blackett Laboratory, Imperial College London, London SW7 2AZ, United Kingdom*

Abstract

We report a model for metalorganic vapor-phase epitaxy on non-planar substrates, specifically V-grooves and pyramidal recesses, which we apply to the growth of InGaAs nanostructures. This model, based on a set of coupled reaction-diffusion equations, one for each facet in the system, accounts for the facet-dependence of all kinetic processes (e.g. precursor decomposition, adatom diffusion, and adatom lifetimes), has been previously applied to account for the temperature-, concentration-, and temporal-dependence of AlGaAs nanostructures on GaAs (111)B surfaces with V-grooves and pyramidal recesses. In the present study, the growth of

$In_{0.12}Ga_{0.88}As$ quantum wires at the bottom of V-grooves is used to determine a set of optimized kinetic parameters. Based on these parameters, we have modeled the growth of $In_{0.25}Ga_{0.75}As$ nanostructures formed in pyramidal site-controlled quantum-dot systems, successfully producing a qualitative explanation for the temperature-dependence of their optical properties, which have been reported in previous studies. Finally, we present scanning electron and cross-sectional atomic force microscopy images which show previously unreported faceting at the bottom of the pyramidal recesses that allow quantum dot formation.

3.1 Introduction

Tuning the electrical and optical properties of advanced III-V quantum-effect-based nanostructures while controlling their position on a chip is crucial for quantum optic [1, 2] and optoelectronic [3, 4] applications. For example, coupling their optical emission to optical cavities or photonic crystal waveguides requires precise spectral and positional control [5]. Of the available growth techniques, epitaxy on patterned substrates exploits the different precursors and adatom kinetics on different facets, which influences local growth rates and local compositions, depending, e.g., on the substrate temperature, V/III ratio and overall deposition rate. Hence, as well as the seeding of the nanostructures, the patterning also allows control over their dimensions and, consequently, over their optical properties [6, 7].

Metal-organic vapor-phase epitaxy (MOVPE) on patterned substrates of V-grooves quantum wires and pyramidal quantum dots [8, 9] has made important contributions to this field in the last 20 years, because of the precise control over the dimensions and position of the nanostructures, together with high degree of uniformity of emission properties [10, 11]. A noteworthy advantage of this approach is the fabrication of arrays of devices, as recently demonstrated in Ref. [12], where entangled photon emission from an array of $In_{0.25}Ga_{0.75}As$ nanostructures was reported.

Some of us have recently presented a phenomenological model for MOVPE growth of (Al)GaAs on V-grooved substrates and pyramidal recesses [13]. The model is expressed as coupled rate equations, one for each facet, and takes into account the interplay between the precursor decomposition rate, adatom diffusion and incorporation, all of which are facet-dependent processes. By comparing with systematic experiments, this model produces quantitative agreement with the observed morphological evolution of the surfaces and the compositional dependence

on position for both transient and stationary growth regimes as a function of temperature [14, 15, 16].

In this work we extend the model to the simulation of the MOVPE of InGaAs, which is extensively employed as optically active layer in quantum dots and quantum wires. As a first step, the growth of $In_{0.12}Ga_{0.88}As$ quantum wires is studied to determine a set of optimized kinetic parameters for InGaAs epitaxy that, when used in our model, reproduce the experimental growth evolution. These optimized parameters are then used to model the growth of $In_{0.25}Ga_{0.75}As$ for nanostructures formed in the pyramidal quantum dot (QD) system. These include an $In_{0.25}Ga_{0.75}As$ quantum dot layer sandwiched in GaAs barrier layers at the bottom of the pyramidal recess and three lateral quantum wires (LQWRs) along its edges [17, 18]. We find that our model can qualitatively explain an unexpected experimental evidence reported in previous studies (see Ref. [19]) where, by diminishing the growth temperature, a blue-shift of the QD emission was observed, while the LQWRs surprisingly showed the opposite trend.

The facetting of the surfaces composing the profile of the pyramidal recess plays a major role in the evolution of the nanostructures grown on it. Several studies report the formation of high-index facets during MOVPE growth of III-V nanostructures [8, 20], which can considerably affect the growth result. In the final section we show experimental microscopy data showing that InGaAs QD formation in pyramidal recesses is accompanied by a more complex than expected facetting. We conclude with discussion of open issues.

3.2 Theory

Our growth model takes into account the following processes, which, in a simplified picture, are assumed to determine the main aspects of growth by MOVPE. Precursors

(trimethylgallium/aluminum/indium as group-III and arsine as group-V atom sources) arrive on the surface of the substrate and, after diffusing, decompose, releasing single atoms of the growing material while the remaining reactants desorb from the surface. The released atoms then diffuse on the surface until incorporation into the growth front. The high V/III precursor flows ratio employed experimentally (~600) enable us to consider the kinetics of only the group-III species and neglect the kinetics associated with the group-V species, as they are unlikely to be a rate-limiting. Analogous assumptions are made for modelling molecular-beam epitaxy of III-V systems [21]. For each of the group-III species comprising the alloy, the evolution of the free-atom density n_i on each facet (i) can be determined through the reaction-diffusion equation:

$$\frac{\partial n_i}{\partial t} = D_i \nabla^2 n_i + F_i - \frac{n_i}{\tau_i} \tag{1}$$

where D_i is the diffusion coefficient, F_i is the effective single atom deposition rate (which is affected by the anisotropy of the decomposition rate of the precursors), and τ_i is the average adatom lifetime prior to incorporation. The diffusion coefficient and adatom lifetime are taken to have Arrhenius forms: $D_i = D_0 e^{-\beta E_{D_i}}$ and $\tau_i^{-1} = \upsilon_0 e^{-\beta E_{\tau_i}}$, in which $\beta = 1/(k_B T)$, K_B is Boltzmann's constant, T the absolute temperature, and E_{D_i} and E_{τ_i} the energy barriers, respectively, for the diffusion and the incorporation processes. This form emerges directly from transition-state theory [22], but we treat the Arrhenius parameters (prefactors and barriers) as adjustable. We have used $D_0 = a^2 \nu$, where a is the lattice constant of the surface, with $\nu = 10^{15}\ Hz$ Hz, while $\nu_0 = 4.59\ Hz$ (Ref. [15]).

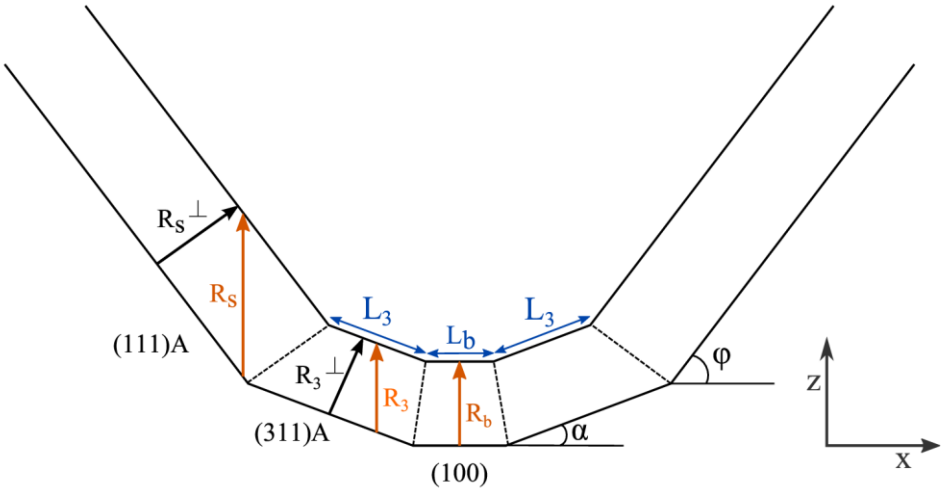


Fig.1: A two-dimensional section used to model the compositional and morphological evolution within a V-groove. The labels b, s, and 3 are used to indicate the base facet, the lateral facets and the intermediate (311)A facets, respectively.

The solution of (1) across all facets in the structure requires continuity conditions at each facet boundary for the adatom densities $n_i(x)$ and the corresponding diffusion currents, $\boldsymbol{J}_i(x) = -D_i \boldsymbol{\nabla} n_i$. Owing to the translational invariance of V-grooves along their axis, the kinetics will be modelled as the two-dimensional cross-section shown in Fig.1. This assumes that there are no processes along the V-groove that substantially affect the morphological and compositional evolutions. The quality of the fit between experiments and our theory will provide a *post hoc* justification of this assumption. For the growth of QDs in pyramidal recesses, we use the conical template in Fig.2, with the circular symmetry about the vertical axis used for simplicity in obtaining an analytic solution of (1). Although the validity of this approximation requires the side facets be much longer than the diffusion lengths of the adatoms, the kinetics exchange mechanisms between the bottom and the side

facets are accurately taken into account. When solutions $n_i(x)$ of (1) are obtained, the growth rate $R_i(x)$ on each facet is expressed as

$$R_i(x) = \frac{\Omega_0}{\tau_i} n_i(x) \tag{2}$$

where Ω_0 is the atomic volume.

To calculate the evolution of the facet dimensions during growth, we must solve (1) coupled to the following equations for the lengths of the facets:

$$\frac{dL_b}{\partial t} = 2\left(R_b - \frac{R_3^{\perp}}{\cos\alpha}\right)\cot\alpha \tag{3}$$

$$\frac{dL_3}{\partial t} = \frac{\frac{R_3^{\perp}}{\cos\alpha} - R_b}{\sin\alpha} + \frac{\cos\phi}{\sin(\phi-\alpha)}\left(\frac{R_3^{\perp}}{\cos\alpha} - \frac{R_s^{\perp}}{\cos\phi}\right)\cot\alpha \tag{4}$$

for V-grooves, or coupled with

$$\frac{dL_b}{\partial t} = 2\left(R_b - \frac{R_s}{\cos\theta}\right)\cot\theta \tag{5}$$

for pyramidal recesses, where R_i are the average growth rates on each facet, the symbol $\perp$ indicating the component orthogonal to the facet, and L_i are the lengths of the facets comprising the templates. We employ an incremental stationary solution based method to solve the system by choosing a time-step longer than the adatom concentration relaxation time and considering a starting surface profile. Under these

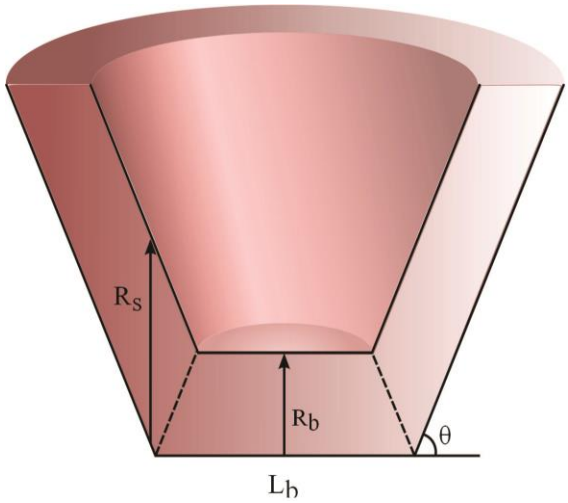


Fig.2: The template used to model a pyramidal recess, where growth rates, facets and angles are shown. The labels *b* and *s* indicate respectively the base facet and the lateral facets.

assumptions equation (1) is solved in the stationary regime ($dn_i/dt = 0$), then the resulting growth rate on each facet is calculated and the facet dimension variation for each step is found. The iteration of this procedure allows to calculate the time evolution of both surface profile and the relative concentration of the elements in the deposited layers, given by the ratio of the growth rate of each species for each facet. For long growth times, the vertical growth rates reach a common value, leading to a "self-limiting" growth determined by the balance between the diffusion currents and the growth rate anisotropy.

3.3 Experiment

The results obtained from the theoretical model were validated by comparison with published experimental work, as described in the text. In particular, the results of the computations with our model enable the prediction of energy gaps of the different

regions of the nanostructures based on their composition, together with a qualitative estimate of the quantum confinement effect, depending on their size. These were then compared with the photo-luminescence spectra obtained performing measurements on the actual samples.

For experiments carried out for the present study, four pyramidal quantum dot samples (A1-A4) were grown at different growth temperatures (640°C, 670°C, 700°C and 730°C) with the aim of exploring the changes in their optical properties [19]. A nominal 0.5-nm-thick $In_{0.25}Ga_{0.75}As$ layer was grown between two GaAs barriers (the lower being 100 nm thick and the upper 70 nm thick), obtaining a single dot and three lateral wires along the three edges of the pyramidal recess. In Fig.3 we summarize the photoluminescence spectra of each sample obtained by non-resonant photoexcitation at 8 K relevant to this work, where both the emission originating

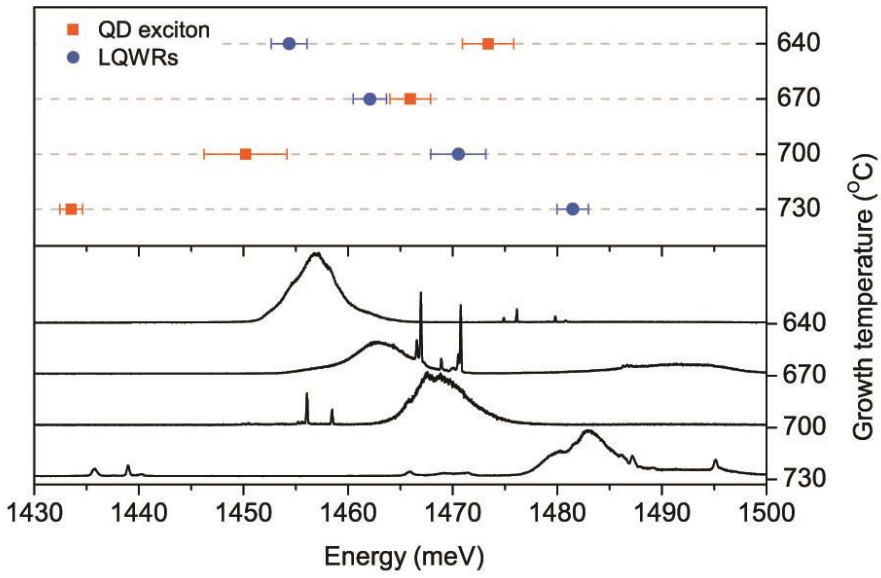


Fig.3: Photoluminescence spectra of four pyramidal QD samples grown at different temperatures. The temperature dependence of the emission energy of QD and LQWRs obtained from the statistics over a large number of pyramidal QDs is presented in the top graph, while the bottom graph shows four representative spectra.

from the exciton recombination in the QD and from the LQWR are visible, as reported in Ref. [19]. The red-shift of about 30 meV is observed for LQWRs emission, while a blue-shift of about 40 meV is obtained for the QDs as the temperature is decreased. More details relative to the growth of these samples can be found in Ref. [19].

The geometrical dependence on the growth temperature and the morphological similarities between V-grooved QWRs and pyramidal LQWRs were analyzed through scanning electron microscopy (SEM) and cross-sectional atomic force microscopy (CS-AFM) of two samples (B1-B2) grown at different temperatures. The structure was the same as for pyramidal QD samples A1-A4 from Ref. [19], but the growth was interrupted before the $In_{0.25}Ga_{0.75}As$ layer. A GaAs buffer layer was deposited on top of the GaAs pyramidal recess, then a series of AlGaAs layers of different composition followed by a 100-nm-thick GaAs barrier grown at 640°C for sample B1 and 730°C for sample B2. Another sample (B2') with the same structure as B2 was grown and capped with another 30 nm $Al_{0.55}Ga_{0.45}As$ layer to allow a better contrast CS-AFM imaging of the top GaAs layer. The results of our findings will be presented and discussed in the next section.

3.4 Results and discussion

3.4.1. Determination of kinetic parameters

As a first step, our model was employed to simulate the transient growth of $In_{0.12}Ga_{0.88}As$ V-grooves with GaAs barriers, using as reference model the growth as described in Ref. [23], which reports a transmission electron microscopy (TEM) image clearly showing the morphology and composition of the nanostructure for an alloy with a 12±2% concentration of In on the sidewalls of the V-groove. Noticeably, the authors report a higher concentration of In on the bottom of the groove measured

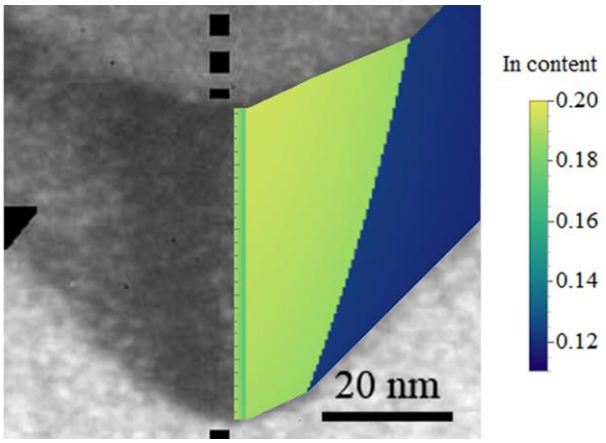


Fig.4: Result of the transient growth simulation compared to the actual TEM image from Ref. [23], showing good agreement for both dimensional and compositional evolution.

through electron energy-loss spectroscopy [23], specifically of about 22±2%, probably due to larger diffusion lengths of In adatoms compared to the Ga.

After imposing the dimensions and the orientation of the facets composing the initial profile (extrapolated from the reported TEM image, see our Fig.4) the transient

	Indium				Gallium			
Facet	E_D (eV)	E_τ (eV)	λ (nm)	r	E_D (eV)	E_τ (eV)	λ (nm)	r
(100)	1.25	0.100	100.7	1.00	1.80	0.114	2.07	1.00
(311)A	1.15	0.103	212.5	1.01	1.40	0.128	41.58	1.01
(111)A	1.12	0.167	420.1	1.01	1.35	0.159	74.79	1.10

Table1: Parameter set I for the barriers E_D and E_τ to diffusion and incorporation, respectively, for In and Ga on the indicated facets. For each facet, once these energy barriers are fixed, and the diffusion lengths k are determined ($\lambda = \sqrt{D\tau}$). The parameter r indicates the ratio of the adatom deposition rate on each facet to that relative to the (100) facet.

evolution of the $In_{0.12}Ga_{0.88}As$ quantum wire on the GaAs V-groove was modelled for a thickness of 45 nm at a "real" temperature of 530˚C (estimated by assuming, since the reactor in Ref. [23] is identical to ours, that a similar difference between thermocouple and real growth temperature can be assumed). The modelling was carried out as in previous work on the (Al)GaAs system, with Ga parameters temperature dependence set identical [15]. An iterative fitting of the free In kinetic parameters, i.e. the energy barriers for the diffusion and incorporation processes and the effective adatom deposition fluxes (Table 1), produced good agreement between the model and the experimental data for both the morphological and compositional evolution of the InGaAs layer (hence of the In segregation profile). We take this as an indication of the overall validity of the model when applied to InGaAs systems.

The comparison between the two species parameters in Table 1 suggests, not unexpectedly, that Indium is a more mobile species, which is consistent with its segregation on the bottom of the V-groove, and is indeed a prerequisite for reproducing the phenomenological findings. This is consistent with *ab initio* calculations of the diffusion of Ga and In on GaAs(001) surfaces [24, 25], which are attributed to the differences in the cation-As bond strength in the corresponding binary compounds (GaAs,InAs) and the larger ionic radius of indium. In effect, the potential energy surface is less corrugated for In than for Ga adatoms.

The long In diffusion lengths on the various facets appears to reduce the importance of the decomposition rate anisotropies between facets, as the results of the simulation are largely insensitive to changes in the In ratio for effective deposition fluxes on different facets. For example, varying the ratio of the effective deposition rate on the (111)A facet to that on the (100) facet in the range 0.5 to 2.0 resulted in a change of In concentration of about 1% only, with a rather small change in the facets dimensions (< 1 nm).

The nominal relative deposition flux for Indium being 12%, the segregation level resulting from our simulations is about 20%, in very good agreement with the

experimental values. Furthermore the concentration profile matches that seen in experimental, as evidenced from the TEM color trend in Fig.4. Moreover, in the dark-field TEM image from Ref. [23], it is possible to distinguish a vertical region in the center of the V-groove with a lower contrast, which was interpreted as a result of strain or other artifacts. Our simulations also show a central region above the (100) base facet with a lower In content (see Fig.4, the darker green stripe). Therefore, we suggest that the contrast difference reported in Ref. [23] would be simply originating from the morphology of the template and the kinetics during growth, relieving the localized strain factor as the main contribution to segregation effects.

The optimized parameters determined for V-grooves were then used to simulate the growth in pyramidal recesses [6] at different temperatures. The three edges (which share the same crystallographic facets and directions as V-grooves) give rise to LQWRs, while the QD forms at the bottom (111)B facet.

3.4.2. LQWRs and pyramidal QDs

In order to apply the model to the LQWR system grown in a pyramidal recess, we make the reasonable assumption that it can be modelled in the same way as the V-groove system in terms of facetting on the bottom of the groove. Moreover, the two systems within the pyramidal recess (LQWRs and QD) are assumed independent here in the hypothesis that the region we consider along the LQWR is distant enough from the bottom facet. This is consistent since the dimensions of the pyramid edges are far more extended in length (about 2-3 μ*m*) than the base facet (30-60 nm). In these simulations we only consider the last GaAs layer before the $In_{0.25}Ga_{0.75}As$ layer, and disregard the underlying layer structure under the assumption that the 100-nm-thick GaAs layer has reached its self-limited profile and therefore this profile depends only on the experimental conditions.

Using the parameters set in Table 1, our model was applied to the LQWRs in the pyramidal recesses by simulating the growth of 2 nm of $In_{0.25}Ga_{0.75}As$ over the GaAs self-limited profile (whose dimensions were calculated following Ref. [15]) at the four different growth temperatures of the samples (A1-A4) described in Sec. 3.3. Note that the nominal thickness of the dot layer is 0.5 nm. However, in our growth regime, an overall increase of the vertical growth rate at the bottom of the template occurs, leading to an increased vertical thickness of the deposited layer on the base facet. The chosen value for the simulations (2 nm) is a typical value, as estimated in previous theoretical works [26]. As a result of each simulation, both composition and

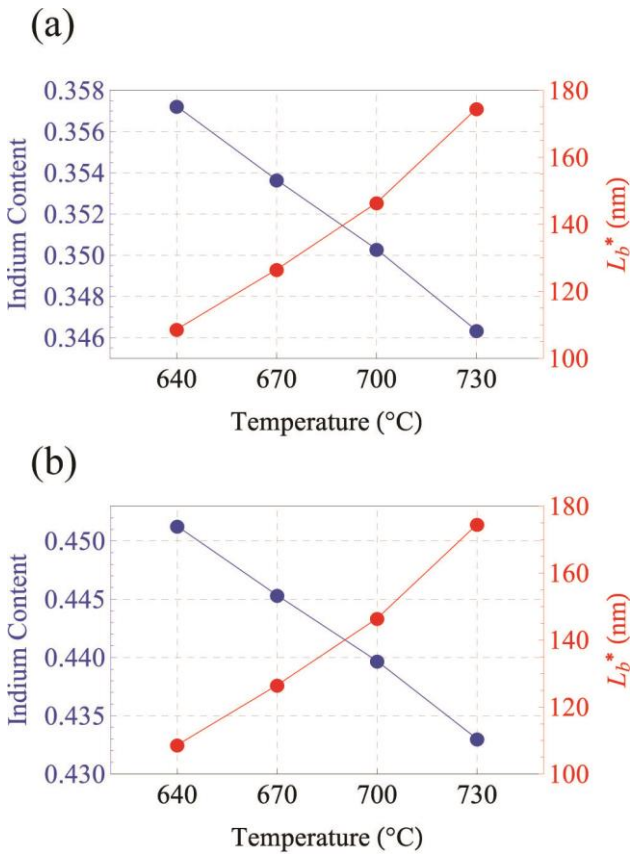


Fig.5: Temperature dependence of In relative content on the bottom facet and of the total length of the base facets ($L_b^* = L_b + 2L_3$) resulting from the simulations of LQWRs growth along the edges of a pyramidal recess. Results with (a) parameter set I (Table 1), and (b) parameter set 2 (Table 2).

lateral dimensions were found not to vary significantly over the vertical thickness of 2 nm during the transient evolution, so we show only an average value in Fig.5. The simulations indeed evidence an increase in In segregation at the bottom of the LQWR as the temperature is decreased, which in terms of the energy gap, leads to a decrease of about 11.7 meV at 8 K, without considering confinement effects. This is in line with the experimentally reported red-shift discussed earlier, even if the experimentally measured value is bigger (∼30 meV).

To predict the emission-energy-dependence on the growth temperature of the nanostructure we must take into account the change in the quantum confinement effect derived from the variation of the dimension. Nevertheless, in the case of these LQWRs, we may be able to assume that this is a small effect, since the total lateral dimensions ($L_b^* = L_b + 2L_3$) are far larger (from 108 nm to 175 nm, depending on the growth temperature) than the Bohr radius of the exciton (which can be estimated as about 20-30 nm), and only the vertical dimension should be affected. The morphological/geometrical similarity between the two systems (V-grooved quantum wires and LQWRs) will be discussed in the next section, in which a series of deviations from the ideal situation will be presented.

Keeping in mind the non-ideal nature of the actual samples, in order to verify that the segregation temperature dependence could have a major role in the red-shift, a further study was done. Another iterative procedure was carried out to determine a set of kinetic parameters for both Ga and In that would result in an even more pronounced shift of the spectrum along with the temperature without deviating too much from the parameters obtained from the previous fit. The resulting set of parameters (Table 2) resulted in the temperature dependence shown in Fig.5 (b), corresponding to an energy gap decrease of about 21.1 meV. Although this result was not obtained directly from the fitting of experimental data, it shows that the hypothesis of segregation temperature dependence could be a valid explanation for the observed red-shift and indeed a compatible physical process in this system.

Facet	Indium			Ga		
	E_D (eV)	E_τ (eV)	r	E_D (eV)	E_τ (eV)	r
(100)	1.27	0.090	1.00	1.85	0.122	1.00
(311)A	1.22	0.095	1.01	1.55	0.141	1.01
(111)A	1.20	0.187	1.01	1.25	0.159	1.10

Table2: Parameter set II for the barriers E_D and E_τ to diffusion and incorporation, respectively, for In and Ga on the indicated facets. The parameter r indicates the decomposition rate anisotropy relative to (100).

The next step was to apply the model to the growth of the InGaAs QD using the three-dimensional (3D) conical representation in Fig.2 to verify that the same temperature dependent mechanism does not significantly affect the QD (as expected from the blue shift reported, which was tentatively attributed in Ref. [19] to a change in the self-limited profile, and not to a change in In segregation). The kinetic parameters for the lateral (111)A facet were chosen to be equal to those relative to the same facet in the LQWR growth model. For the base (111)B facet, however, no

Optimized for set	Indium				Ga			
	E_D (eV)	E_τ (eV)	ν_0 (s^{-1})	r	E_D (eV)	E_τ (eV)	ν_0 (s^{-1})	r
1	1.45	0.059	5.81	1.01	1.52	0.031	4.13	1.10
2	1.50	0.066	5.71	1.01	1.55	0.020	4.00	1.10

Table3: Parameters for the (111)B facet optimized for parameter sets 1 (Table 1) and 2 (Table 2).

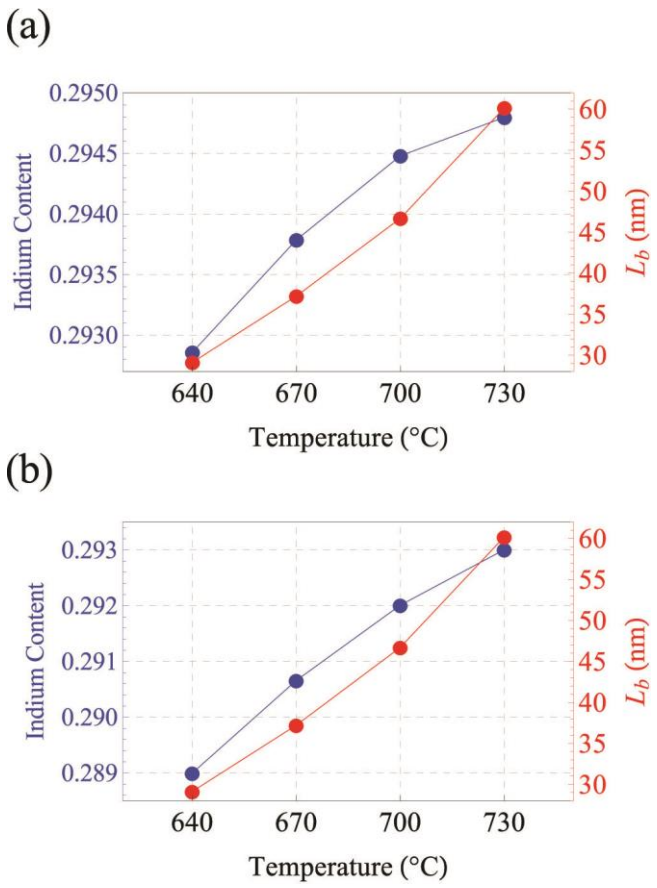


Fig.6: Temperature dependence of the length and In relative concentration on the base facet resulting from the simulations of the QD growth on the bottom of a pyramidal recess. Results obtained with (a) parameters set I (Table 1), and (b) parameters set II (Table 2).

detailed experimental data was available to fit the growth of $In_{0.25}Ga_{0.75}As$ on GaAs. A set of kinetic parameters was chosen that resulted in a segregation of In of about 4% on the bottom facet at a specific growth temperature, as suggested by other theoretical studies on pyramidal QD optical properties [26].

As pointed out elsewhere [14], the fitting of the parameters for the 3D case requires the optimization of the exponential prefactors ν_0 of the adatom lifetimes in order to get a consistent result. This was done for parameter sets 1 and 2 and for both Ga and In. For each set we found parameters for the (111)B bottom facet (Table 3) that resulted in around 4% segregation on that facet, interestingly, without presenting any

significant increase of In concentration as the temperature was increased (Fig.6), rather differently from the LQWR case. In this case the lateral dimension of the QDs are comparable to the exciton Bohr radius, leading to quantum-confinement influence on the emission. In particular the decrease in temperature implies a decrease in the lateral dimensions of the QD, and therefore to a blue-shift of the emission, as observed experimentally. Nevertheless, we caution the reader that more theoretical calculations need to be done in order to evaluate completely the origin of this effect in our case, taking into account the particular geometry of the QD.

3.5 Morphology of pyramidal recesses

To gain insight into the quantitative discrepancies between the experimental theoretical results, SEM and CS-AFM imaging was performed on representative samples, which revealed that the actual shape of a pyramidal recess is made of a more complex facetting than the simplified profile assumed in our and previous models. Samples B1 and B2, described in Sec. 3, were cleaved along the (110) direction in order to image the cross-section of both the LQWRs and QD positions, with the nanostructure which could be imaged depending on the point where the cleavage was actually done.

CS-AFM analysis performed on samples B1 and B2 showed that the lateral facet (111)A orientation evolves during the growth of the different layers (this is not in itself a new observation, but we recall it here for completeness). Therefore, the final GaAs facet is not a pure (111)A, but a *vicinal* facet. The reason for this phenomenon is not clear, but we notice that it holds similarity to what happens in the case of V-groove quantum wires [15]. Considering, for example, the sample shown in Fig.7, the angle between the vicinal facet (111)A and the base facet (111)B is 77°, and from basic trigonometry, the resulting angle between the lateral facet (111)A and the edge

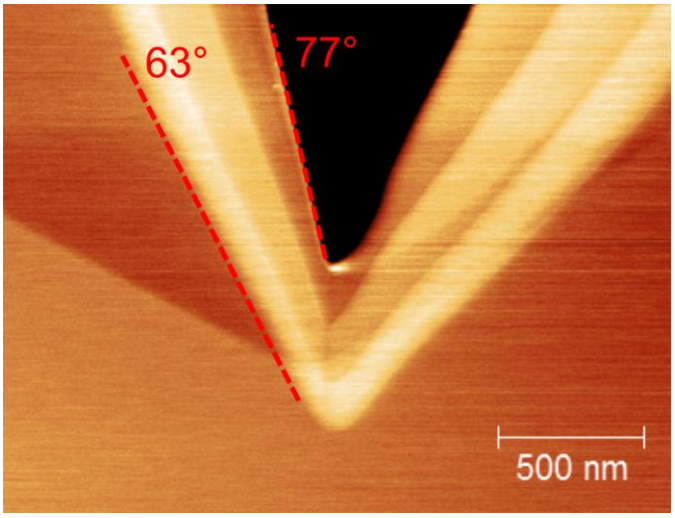


Fig.7: (Color online) CS-AFM image of the vertical section of a pyramidal recess from sample B2 showing the layer sequence and the evolution of the orientation of the lateral (111)A vicinal facets.

base facet (100) is about 33°, which significantly differs from the 45° angle that characterizes the V-groove. This suggests that the kinetic parameters for both Ga and In should be optimized for the particular vicinal facet, and could be one of the reasons for specific deviations between theory and experiment.

SEM imaging was also performed in both top-view and tilted view (in order to distinguish the cross-section of the pyramid). Particular care was taken in order to make sure that (or searching for regions where) the cleaving line passed through a precise point of the pyramidal recess to enable the edge of the pyramid and its center cross-section to be distinguished. Unless specified, the following considerations are valid for both samples B1 and B2, which showed very similar qualitative characteristics.

The top-view images in Fig.8 shows that each of the three lateral facets of the pyramid is formed by two vicinal facets, creating a sort of hexagonal inward-shaped top outline (Fig.8 (a)). This effect is more pronounced in the lower-temperature sample (B1), and less evident for high temperature growth (B2). The top-view images

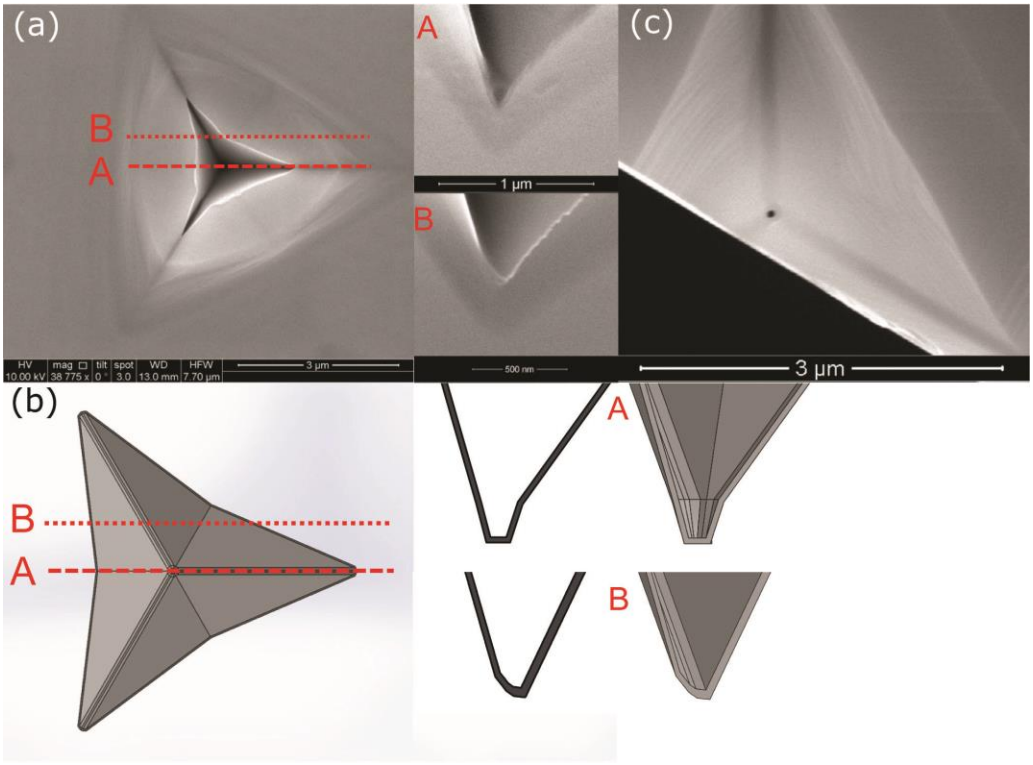


Fig.8: (a) Top-view SEM image of a pyramidal recess from sample B1, and cross-sectional views of recesses cleaved along different sections (cross-section A is relative to a cleavage cutting through the center of the pyramid, while cross section B to one along an axis cutting through one of the LQWRs). (b) 3D model of a pyramidal recess, reconstructed considering the experimental results of our analysis and qualitative comparison of the obtained cross-sections. A and B cross-sections correspond to the same labeled experimental cross-sections, and for each both the 3D cross-section (on the right) and the upper surface outline (on the left) are shown. (c) top-view SEM image of a pyramidal recess from sample B2 after cleavage; this particular shows the different depths of the edges and of the bottom.

also show a dark region corresponding to the edges and bottom of the pyramid, denoting deeper regions of the recess (we should remark that it not so evident at first, but this becomes clearer after a number of these analyses are performed). In particular the center of the recess was found to be the deepest feature, delimited by a quasi-circular outline (Fig.8 (c)), smaller in diameter than the lateral broadening of the wires. This suggests that the bottom facetting of the pyramid cannot be simply

related to the LQWRs and that it is likely more complicated than the facetting structure assumed in our model. For example, a steeper (vicinal) facet between the lateral vicinal (111)A and the bottom (111)B facets, resulting from the assembly of the three pyramid edges joined at the center of the recess, could lead to a more pronounced dip.

Using the foregoing observations and hypothesizing that that the facetting at the edges is similar to that of a V-groove, taking all into consideration, we built a qualitative graphical 3D model of the pyramidal recess, from which we obtained the corresponding cross-sectional view in different points of the recess (Fig.8 (a,b)). A comparison between the experimental and hypothesized cross-section shows that our 3D model is compatible with the observed experimental cross sectional morphology. Moreover, recent Monte Carlo growth simulations from Ref. [27] suggested a similar behavior of the facetting on the bottom recess of (low temperature grown) small pitch pyramidal recesses, and are therefore in agreement with our findings. Obviously more microscopy work (TEM) will be needed, both to clarify the exact morphological facetting at the bottom of the recesses, and to understand the exact implications in terms of optical properties.

3.6 Conclusions

In this work the growth model for MOVPE on patterned substrates we previously presented was extended to the growth of InGaAs nanostructures. The kinetic parameters resulting from an empirical fitting procedure to the experimental data of a V-grooved quantum wire from the literature produced good agreement between the simulated and the actual growth result in terms of morphology and composition, reproducing the segregation profile of In on the bottom of the V-groove. Therefore, on one hand, this result can be considered a validation of the model and, on the

other hand, enables simulations of the growth of other nanostructures to be carried out. Here, through simulations at different growth temperatures for pyramidal QDs and LQWRs a new explanation for the unexpected reported behavior of the LQWRs emission in pyramidal QDs was proposed.

The model will be employed in future work in order to guide the MOVPE growth parameters and provide a better control over nanostructure formation. As a first step, the analysis carried out through SEM and CS-AFM to understand the actual geometry of a LQWR and its compatibility with the V-groove picture revealed a complicated faceting on the bottom of the pyramid. Our findings will be important for the scientific community for correlating/describing pyramidal QD optical properties and will be further investigated to optimize the theoretical model and obtain more accurate simulations.

References

[1] P. Kok, W. J. Munro, K. Nemoto, T. C. Ralph, J. P. Dowling, and G. J. Milburn, *Rev. Mod. Phys.*, vol. 79, no. 1, pp. 135–174, 2007.

[2] A. Politi, J. C. F. Matthews, M. G. Thompson, and J. L. O'Brien, *Ieee J. Sel. Top. Quantum Electron.*, vol. 15, no. 6, pp. 1673–1684, 2009.

[3] S. Noda, *Science*, vol. 314, no. 5797, pp. 260–261, Oct. 2006.

[4] K. A. Atlasov, A. Rudra, B. Dwir, and E. Kapon, *Opt. Express*, vol. 19, no. 3, pp. 2619–2625, 2011.

[5] K. Hennessy, A. Badolato, M. Winger, D. Gerace, M. Atatüre, S. Gulde, S. Fält, E. L. Hu, and A. Imamoğlu, *Nature*, vol. 445, no. 7130, pp. 896–899, Feb. 2007.

[6] E. Kapon, E. Pelucchi, S. Watanabe, A. Malko, M. H. Baier, K. Leifer, B. Dwir, F. Michelini, and M.-A. Dupertuis, *Phys. E Low-dimensional Syst. Nanostructures*, vol. 25, no. 2–3, pp. 288–297, Nov. 2004.

[7] S. Kiravittaya, A. Rastelli, and O. G. Schmidt, *Reports Prog. Phys.*, vol. 72, no. 4, 2009.

[8] E. Martinet, F. Reinhardt, A. Gustafsson, G. Biasiol, and E. Kapon, *Appl. Phys. Lett.*, vol. 72, no. 6, pp. 701–703, 1998.

[9] A. Hartmann, L. Loubies, F. Reinhardt, and E. Kapon, *Appl. Phys. Lett.*, vol. 71, no. 10, pp. 1314–1316, 1997.

[10] L. O. Mereni, V. Dimastrodonato, R. J. Young, and E. Pelucchi, *Appl. Phys. Lett.*, vol. 94, no. 22, p. 223121, Jun. 2009.

[11] E. Pelucchi, M. Baier, Y. Ducommun, S. Watanabe, and E. Kapon, *Phys. Status Solidi B-Basic Solid State Phys.*, vol. 238, no. 2, pp. 233–236, 2003.

[12] G. Juska, V. Dimastrodonato, L. O. Mereni, A. Gocalinska, and E. Pelucchi, *Nat. Photonics*, vol. 7, no. 7, pp. 527–531, May 2013.

[13] E. Pelucchi, V. Dimastrodonato, A. Rudra, K. Leifer, E. Kapon, L. Bethke, P. A. Zestanakis, and D. D. Vvedensky, *Phys. Rev. B*, vol. 83, no. 20, p. 205409, May 2011.

[14] V. Dimastrodonato, E. Pelucchi, and D. D. Vvedensky, *Phys. Rev. Lett.*, vol. 108, no. 25, p. 256102, Jun. 2012.

[15] V. Dimastrodonato, E. Pelucchi, P. A. Zestanakis, and D. D. Vvedensky, *Appl. Phys. Lett.*, vol. 103, no. 4, p. 042103, Jul. 2013.

[16] V. Dimastrodonato, E. Pelucchi, P. A. Zestanakis, and D. D. Vvedensky, *Phys. Rev. B*, vol. 87, no. 20, p. 205422, May 2013.

[17] V. Dimastrodonato, L. O. Mereni, R. J. Young, and E. Pelucchi, *Phys. Status Solidi B-Basic Solid State Phys.*, vol. 247, no. 8, pp. 1862–1866, 2010.

[18] A. Hartmann, Y. Ducommun, K. Leifer, and E. Kapon, *J. Physics-Condensed Matter*, vol. 11, no. 31, pp. 5901–5915, 1999.

[19] G. Juska, V. Dimastrodonato, L. O. Mereni, T. H. Chung, A. Gocalinska, E. Pelucchi, B. Van Hattem, M. Ediger, and P. Corfdir, *Phys. Rev. B*, vol. 89, no. 20, p. 205430, May 2014.

[20] J. Yuan, H. Wang, P. J. Van Veldhoven, and R. Nötzel, *J. Appl. Phys. Appl. Phys. Lett. J. Appl. Phys.*, vol. 106, no. 101, pp. 124304–233101, 2009.

[21] T. Shitara, D. D. Vvedensky, M. R. Wilby, J. Zhang, J. H. Neave, and B. A. Joyce, *Phys. Rev. B*, vol. 46, no. 11, pp. 6815–6824, Sep. 1992.

[22] P. Hänggi, P. Talkner, and M. Borkovec, *Rev. Mod. Phys.*, vol. 62, no. 2, pp. 251–341, Apr. 1990.

[23] F. Lelarge, C. Constantin, K. Leifer, A. Condo, V. Iakovlev, E. Martinet, A. Rudra, and E.

Kapon, *Appl. Phys. Lett.*, vol. 75, no. 21, pp. 3300–3302, 1999.

[24] J. G. LePage, M. Alouani, D. L. Dorsey, J. W. Wilkins, and P. E. Blöchl, *Phys. Rev. B*, vol. 58, no. 3, pp. 1499–1505, Jul. 1998.

[25] E. Penev, P. Kratzer, and M. Scheffler, *Phys. Rev. B*, vol. 64, no. 8, p. 085401, Aug. 2001.

[26] S. B. Healy, R. J. Young, L. O. Mereni, V. Dimastrodonato, E. Pelucchi, and E. P. O'Reilly, *Phys. E-Low-Dimensional Syst. Nanostructures*, vol. 42, no. 10, pp. 2761–2764, 2010.

[27] A. Surrente, Epitaxial Growth and Optical Properties of Dense Arrays of Pyramidal Quantum Dots, Thesis, École polytechnique fédérale de Lausanne EPFL, 2013.

Chapter 4
Selective carrier injection into patterned arrays of pyramidal quantum dots for entangled photon light-emitting diodes

Chapter based on the published journal article:

Nat. Photonics, vol. 10, no. 12, pp. 782–787 (2016)

T. H. Chung, G. Juska, S. T. Moroni, A. Pescaglini, A. Gocalinska and E. Pelucchi

Tyndall National Institute, University College Cork, Lee Maltings, Cork, Ireland

Abstract

Scalability and foundry compatibility (as apply to conventional silicon-based integrated computer processors, for example) in developing quantum technologies are major challenges facing current research. Here we introduce a quantum photonic technology that has the potential to enable the large-scale fabrication of semiconductor-based, site-controlled, scalable arrays of electrically driven sources of polarization-entangled photons, with the potential to encode quantum information. The design of the sources is based on quantum dots grown in micrometre-sized pyramidal recesses along the crystallographic direction (111)B which theoretically ensures high symmetry of the quantum dots – the condition for actual bright entangled photon emission. A selective electric injection scheme in these non-planar structures allows obtaining a high density of light-emitting diodes,

with some producing entangled photon pairs also violating Bell's inequality. Compatibility with semiconductor fabrication technology, good reproducibility and control of the position make these devices attractive candidates for integrated photonic circuits for quantum information processing.

4.1 Introduction

To develop quantum technologies, the scientific community is looking into several alternative practical routes such as superconducting qubits, atoms on-chips, photonic integrated circuits, among others [1][2][3][4]. All the explored technologies have to solve the scalability and reproducibility problem if they are to deliver successful real-life applications. In the case of the photonic quantum technologies, scalability requires moving from discrete optical elements to integrated photonic circuits and to on-chip solid-state sources, allowing, for example, thousands of units operating in unison – a condition which is very hard to realize at the moment.

Semiconductor quantum dot technology is fundamentally compatible with modern fab/foundry processes, and on-demand identical, single and entangled photons have been all demonstrated by optical pumping [5][6][7][8][9][10][11][12][13][14]. Nevertheless, although the development of electrically pumped (EP) quantum light sources has advanced in general [15], the development of a particular resource, EP entangled photon sources, has proven more challenging. After the first report [16], the community had to wait several years before a similar result could be obtained by other groups [17]. Importantly, the few devices reported so far utilized epitaxial self-assembled QD structures, that is, these devices had no control on the source location, nor on the number of sources in a single device (typically hundreds or more, and not just one or, in the best case scenario, a few): a critical aspect for photonic integration scaling.

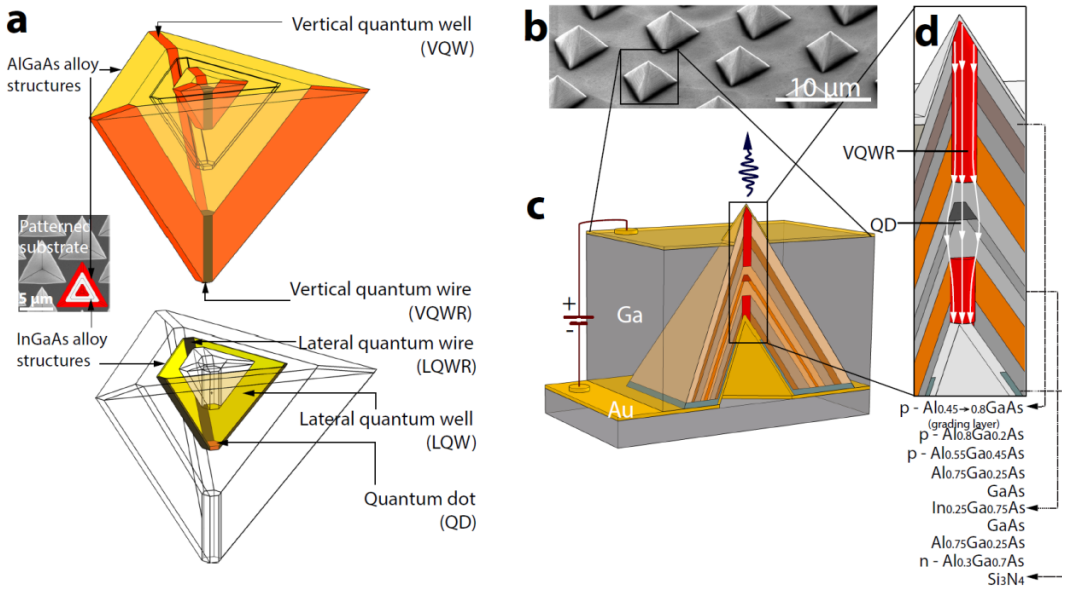


Fig.1: The internal structure of a device and the schematics of a µLED. a, The complex ensemble of nanostructures which self-forms within the pyramidal recesses pre etched in a GaAs substrate. AlGaAs alloys forms gallium enriched structures: a vertical quantum wire (VQWR) along the central axis of the pyramid, and 3 vertical quantum wells (VQW). A nominally thin (0.5 nm) InGaAs alloy forms a QD, 3 lateral quantum wires (LQWR) and 3 lateral quantum wells (LQW). b, The SEM image of a sample right after the chemical etching step showing exposed pyramidal structures in an apex-up geometry which enhances light extraction by a few orders of magnitude. c, A sketch of a p-i-n junction µLED in cross-section view. d, A magnified region of the central part of a pyramid with a QD. The shown epitaxial layers comprise a representative structure with dominant AlGaAs alloys which form a vertical quantum wire (VQWR). Arrows indicate injection current through the region of the VQWR.

4.2 Pyramidal quantum dot system

The technology presented herein is based on the Pyramidal QD system, recently highlighted for its capability of delivering arrays of highly symmetric and uniform QDs [11][18]. The system is, nevertheless, intrinsically non-planar, a feature which has so far impeded the development of efficient electrically driven light-emitting sources.

Before discussing the relevant quantum optics results, we need to highlight the complexity of the Pyramidal system as a key ingredient. In short, single QDs are epitaxially grown by metalorganic vapour phase epitaxy (MOVPE) inside inverted pyramidal recesses, lithographically patterned on a (111)B GaAs substrate (a fragment of such template is shown in Fig. 1a). The structure comprises a number of differently composed III-V (Al)GaAs layers and an InGaAs QD layer (see Supplementary Material for a detailed description of each layer, and the reasons for inserting them) – all obeying complex epitaxial dynamics as reported elsewhere [19][20][21][22]. The outcome is an ensemble of self-forming nanostructures inside each pyramidal recess, described by the generic sketches in Fig. 1a. During growth of an AlGaAs alloy, fast diffusing Ga tends to segregate in the regions of intersecting walls of the recess and in a narrow region at the centre of the Pyramidal structure, effectively forming three embedded low bandgap vertical quantum wells (VQW) and a vertical quantum wire (VQWR) of ~20 nm in diameter, respectively. In addition, a thin InGaAs layer forms a group of interconnecting nanostructures: a flat quantum dot at the central axis of the structure, three lateral quantum wires (LQWR) and three lateral quantum wells (LQW). Such apex-down geometry hinders light extraction, which can be efficiently enhanced by two or three orders of magnitude (typically achieving $6 \cdot 10^4$ – $15 \cdot 10^4$ photon/s detection rate under continuous-wave excitation in our system) selectively etching away the substrate (a process known as back-etching, see Supplementary Material) so to obtain apex-up pyramidal structures as shown in Fig. 1b – a typical configuration used for measurements [11][23]. To fabricate a single QD light-emitting diode, the lack of planarity on both sides of a sample, unfortunately, does not allow for simply contacting the back and the top of the Pyramid. The proposed schematic for a µLED device is depicted in Fig. 1c, emphasizing its 3D intrinsic nature, lateral dimensions «10µm, and drafting the presence of a nanowire like structure (VQWR) running through most of the structure,

and, as it will be discussed later, contributing importantly to a selective injection process feeding the single QD at the centre (the magnified region is shown in Fig. 1d).

4.3 Selective current injection

In order to fabricate a QD LED, there are number of hurdles to overcome, and we will here discuss the most relevant. Fig. 2a shows the cross-sectional SEM image of the Pyramidal structure, where the device is still contained inside the GaAs substrate (the different grey layers result from the various Al containing alloys and doping). The centre vertical path (blue arrow in Fig. 2a), where the single QD is located, is not the most electrically favourable path. Because of the geometry, the centre path is ~3 times longer than taking a short across the side (red arrow Fig. 2a), i.e. in a LED structure current will favourably go along the red path, resulting in a low (or no) probability of intercepting the single QD, and, in general, in an overly crowded LED (i.e. too many charges running) impeding good quality emission from the QD, due to spectral wandering/decoherence induced by random electric fields fluctuations. Moreover, the system is even more non-ideal in its nature, presenting strong faceting at the top (this happens because there is virtually no growth on the planar (111B) substrate, resulting in "facet crowding" – see Supplementary Material and the region circled in Fig. 2a). These lateral facets are the regions of potential current shortcut.

To effectively achieve selective injection to the single QD, one needs to exploit an extra feature of the Pyramidal system – the formation of vertical quantum wires (VQWR) during the high bandgap $Al_{0.75}Ga_{0.25}As$ growth (Fig. 1a). This low bandgap ($Al_xGa_{1-x}As$, $x \leq 0.3$) embedded nanowire is expected to act as a low resistivity path for electrical charges to reach the InGaAs QD (i.e. to introduce a low resistivity path for charges at the centre only, while effectively leaving a high bandgap barrier for transport in the form of, e.g., the $Al_{0.75}Ga_{0.25}As$/ $Al_{0.3}Ga_{0.7}As$ interface, on the sides).

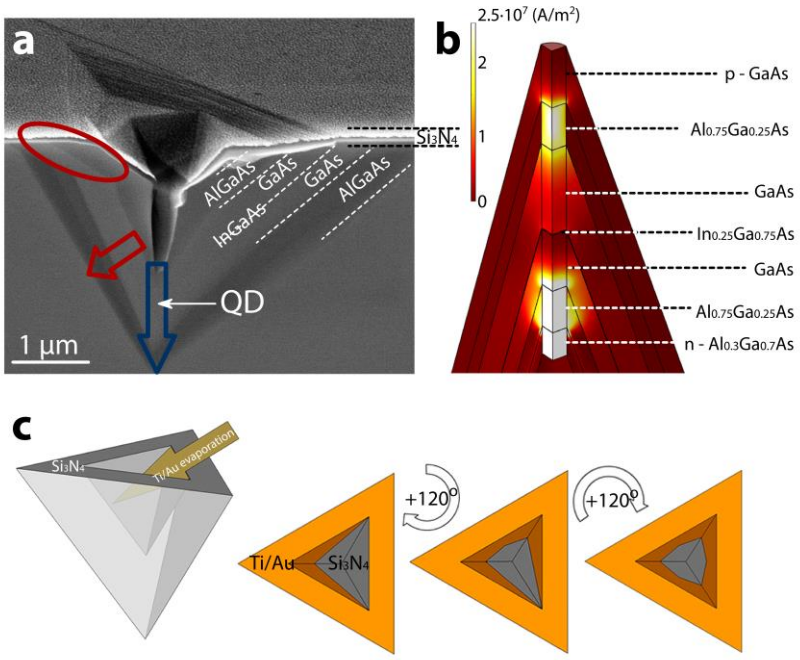


Fig.2: Selective injection scheme and its realisation. a, SEM image of cross-section view of a epitaxial layer structures grown within a pyramidal recess – the device is cleaved to half and still contained within the GaAs substrate in the initial, apex-down, geometry. The layer contrast is mostly due to different alloy compositions. A blue (red) arrow shows the preferential (most probable) direction of carrier injection as per discussion in our text. The region with irregular growth facets close to the surface, which potentially can lead to current leakage/shortcut, is encircled. The top of the sample is deposited with Si_3N_4 except the central part of the pyramid where the back contact of a µLED is formed. b, A colour-map representing current density in a simulated pyramidal structure (see Supplementary Material). The current density is concentrated in the regions of the vertical quantum wires (VQWRs). c, Processing steps to form an open aperture within Si_3N_4 at the central part of the pyramidal recess. Ti/Au (3/15 nm) is evaporated with an angle so that the edge of the recess would be partially shadowing gold deposition. By rotating the sample 120° in-plane twice more and repeating evaporation, an open Si_3N_4 area is left, which is etched away with CF_4 plasma exploiting gold as a protecting mask.

To test our initial intuition, we performed finite elements simulations (see also Supplementary Material): the current density distribution within the magnified region with VQWRs of a simplified device model is shown in Fig. 2a. The simulation coherently describes a preferential current path at the centre. We also observe that

the VQWR does not impede the current flow to other (quantum) structures, but nevertheless most of the current is restricted to the centre region. Based on the simulation results, we implemented this idea in a practical design of the device (Fig. 1c and 1d).

To force current injection at the centre of a Pyramid, a small Ti/Au contact has to be created in that region by a couple of processing steps. First, to prevent electrical short circuits outside the region of injection, a layer of Si_3N_4 is deposited onto the as-grown sample. Second, a tilted sample is evaporated 3 times by Ti/Au, rotating it by 120° in sample growth plane each time. The resulting metallic layer acts as a mask metal, so to leave a small aperture of Si_3N_4 at the centre of the recess (Fig. 2c). This is then opened by CF_4 plasma etching. Subsequently, a Ti/Au layer is evaporated as n-contact (and bonding) metal. The result is a small contact area (>100 nm^2) for the n/p region only at the centre of the Pyramid for the µLED, all simply exploiting self-aligning processes and no sophisticated high-resolution lithography. To prepare for the substrate removal the sample is bonded onto another Ti/Au-coated GaAs substrate with the assistance of a Sn-Au ribbon via a reflow soldering process, which provides a large area contact.

4.4 Electroluminescence

Once the section of the wafer patterned with pyramidal recesses had been fully processed, all pyramids were contacted by evaporating a thin semitransparent layer of titanium (1 nm) and gold (20 nm), and bonding a Kapton insulated wire to the whole structure. At this stage, for simplicity, all µLEDs are contacted, and all potentially turn on. An example (Sample A – see Supplementary Material for a detailed sample description) of gradually turning-on all (~1300) contacted µLEDs at 10 K is shown in Fig. 3c. The bright spots of spectrally unfiltered integrated

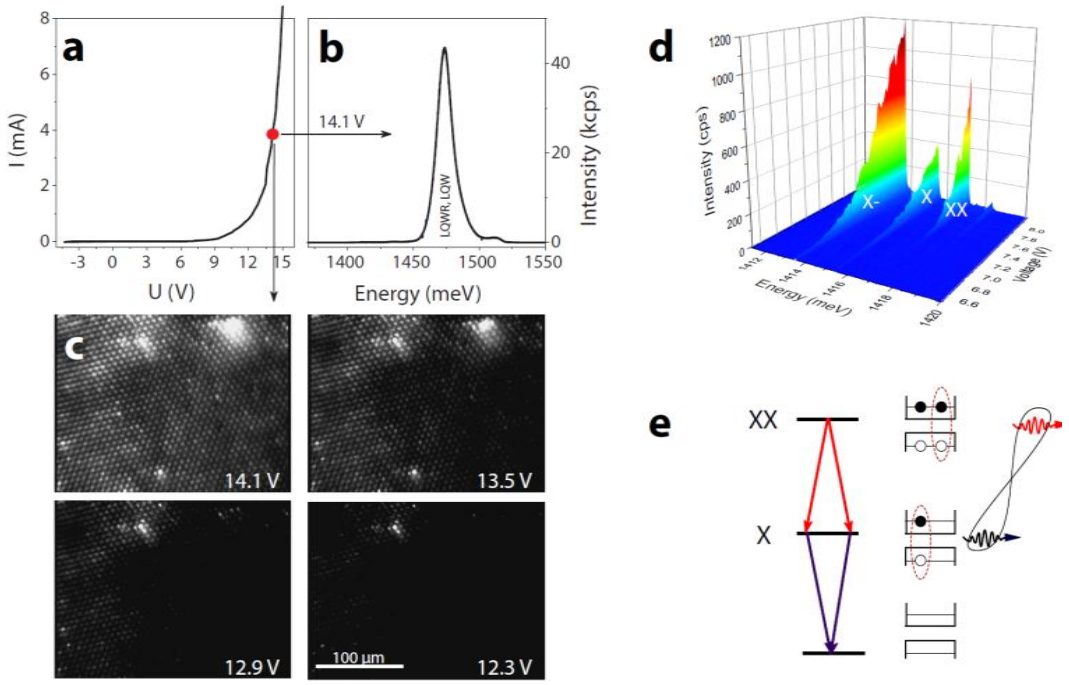


Fig.3: Electroluminescence of µLEDs. a, Current-voltage curve of the Sample A taken at 8 K. b, Macro electroluminescence spectrum taken under applied bias of 14.1 V. Dominant features are LQWRs and LQWs. c, Optical images of switching-on µLEDs with increasing applied bias. The light is not spectrally filtered. d, A single QD (Sample B1) electroluminescence intensity dependence on the applied voltage. Three dominant transitions are a negative trion (X-), exciton (X) and biexciton (XX). e, Polarization-entanglement realization scheme with XX and X transitions. The biexciton is composed of two electrons and two holes (two excitons) and is described by a singlet-like state. During the recombination cascade through the intermediate exciton state, a pair of polarization-entangled photons is emitted.

electroluminescence match the initial pyramidal recess pattern demonstrating that each individual pyramid turns on without significant leakage through the GaAs substrate. This is confirmed by a macro-electroluminescence spectrum in Fig. 3b, where the dominant luminescence features at high injection current of 4 mA are InGaAs lateral quantum wires and lateral quantum wells clearly exceeding the QD luminescence and easily observable using a regular CCD imaging camera. Non-uniformity of intensity regions reflects differences between individual µLEDs, as each

of them turns on at a slightly different voltage, and the I-V curve shown in Fig. 3a is rather the characteristic of the whole ensemble and not of a single device. However, we stress that obviously nothing impedes to be selective to individual or a specific subset of µLEDs in future developments to address or drive them independently, as this would not require any sophistication in the processing.

Several phenomena are possibly contributing to some inhomogeneity of electric injection properties: (1) an inhomogeneous etching profile during the BE step, (2) a complex non-planar surface profile of the back contact side due to slightly irregular MOVPE growth towards the centre of the pyramid, which tends to close the recess irregularly creating variable conditions for the back-contact formation, and (3) by the presence of resistance at the contact side (most probably the p-doped one). These phenomena somehow suggest why the turn-on voltage is unexpectedly high, around 7 V, as shown by a three-dimensional colour map (Fig. 3d) of a representative QD (Sample B1) electroluminescence dependence on the driving voltage, where the dominant transitions are a negative trion (X-), exciton (X) and biexciton (XX). We estimate overall extraction efficiency from these structures with a present design to be ~ 1% (see Supplementary Material for more details).

The average linewidth of exciton and biexciton transitions was found to be 138±34 µeV and 97±23 µeV, respectively. While practical applications will require, ideally, transform-limited linewidth photons, we argue that the broadening is not a fundamental issue here. The origin of it is mostly related to a “charged” vicinity of QDs inducing spectral wandering [24]. We observe that, at this scale of broadening, the external electric field which runs the device has no substantial effect. Ones of the clearly demonstrated sources of charge noise in this QD system are deep hole trapping levels in barriers [18]. The origin of the charge trapping states is most likely related to the processing-induced defects and MOVPE reactor state. We would like to stress that this can be overcome, and that we have a number of successfully

fabricated samples with a high density of QDs with resolution-limited (<18 μeV) linewidth transitions under optical excitation [25]. As we will show later, spectral wandering, being a relatively slow process comparing to the timescale of the biexciton-exciton recombination cascade, does not preclude high fidelity of entanglement.

4.5 Polarization-entangled photon emission

A QD initially populated by the electronic biexciton state (two electrons and two holes, a "singlet-like" configuration) fully recombines through the intermediate state exciton (one electron and one hole) emitting two successive photons which are polarization-entangled (Fig. 3e) [26][27]. Provided that the recombination process proceeds coherently, and a QD has symmetric carrier confinement potential, the emitted pair of photons is described by the Bell's state

$$|\psi\rangle = \frac{1}{\sqrt{2}}(|H_{XX}H_X\rangle + |V_{XX}V_X\rangle),$$

where $|H\rangle$ and $|V\rangle$ are horizontal and vertical polarization states. However, the QD symmetry condition is very rarely fulfilled in general [28][29][30] – electron-hole exchange interaction lifts degeneracy in the exciton level by the energy amount called the fine-structure splitting (FSS), which causes beating (coherent oscillations) of the exciton spin state [18][31][32], later transferred to the two-photon polarization state. Integration over many photon-pair emission-detection events degrades or completely eliminates entanglement if the events are not temporally resolved. Reduction of FSS to the needed sub-microelectronvolt level can be achieved either through various external tuning strategies [31][33][34][35] or exploiting intrinsic growth properties [11][36], like in this work.

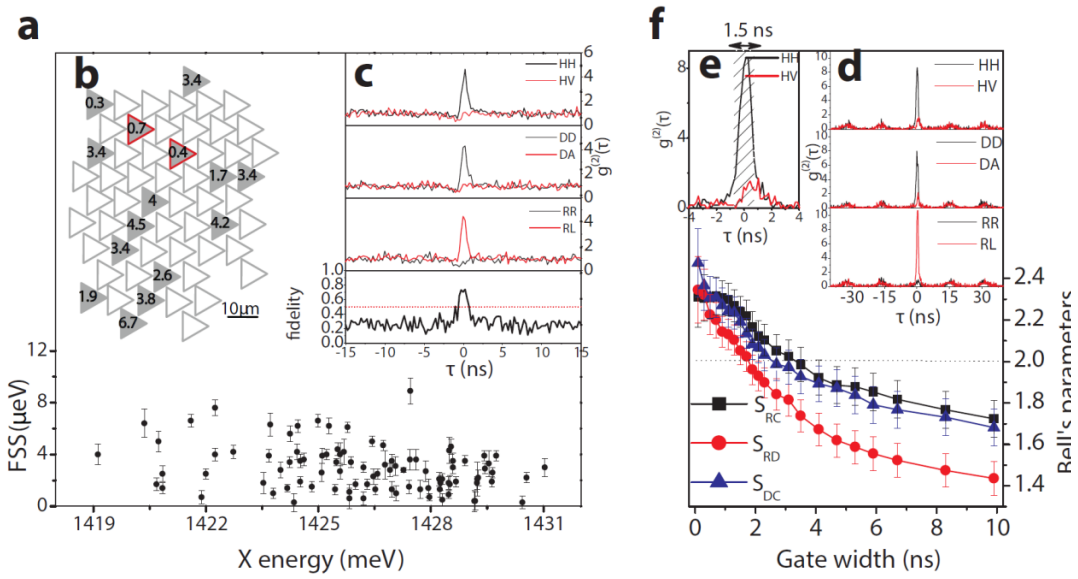


Fig.4: Two-photon polarization state entanglement measurements. a, Distribution of exciton fine-structure splitting values obtained from Sample B2. The error bars represent standard deviation of a fitted sinusoid curve, as described in the Supplementary Material. b, A map of μLEDs from a randomly selected area. Filled-in triangles represent working devices with unquestionable exciton-biexciton emission. The numbers inside the triangles are the FSS values. Two devices framed in red and with a FSS equal to 0.7 and 0.4 μeV emitted polarization-entangled photons. c, CW measurement results of fidelity to the expected maximally entangled state obtained from a device with a FSS value of 0.4 μeV. The classical limit of 0.5 is significantly exceeded around 0 ns delay. d, Polarization-resolved second order correlation curves taken in rectilinear, diagonal and circular polarization bases under pulsed μLED injection. f, 3 Bell's parameters calculated by a simplified procedure using the results shown in e. By selecting correlation events from a time-window of 1.5 ns and preserving 75% of the initial intensity, all 3 parameters violated the classical limit of 2, proving non-classical nature of the polarization-state. The error propagation to the values of all parameters has been estimated using Poissonian uncertainty.

Fig. 4b shows a map of a randomly selected area to measure the density of functional μLEDs with bright X and XX transitions and distribution of the FSS values, where filled-in triangles represent emitting μLEDs. Dysfunctional QDs represented by open triangles were either strongly charged or non-emitting due to possible defects in the vicinity of a QD. The numbers inside triangles are measured FSS values. Most of them

are smaller than 4 μeV – a good agreement between previously found values from optically excited samples [18]. The full distribution of FSS values obtained from 94 μLEDs is shown in Fig. 4b with an average value of 2.9±1.8 μeV, while the standard deviation of the exciton transition energy is 2.6 meV.

Two μLEDs with FSS values of 0.7 and 0.4 μeV (marked by a red border in the map in Fig. 4a), and, importantly, without strong background coming from adjacent device electroluminescence, were selected to test for polarization-entanglement. Six polarization-resolved biexciton-exciton continuous-wave injection (CW) intensity correlation curves measured in rectilinear, diagonal and circular bases are shown in Fig. 4c from a device with 0.4±0.8 μeV FSS. Clearly obtained correlations between co-polarized biexciton and exciton photons in rectilinear and diagonal, and anticorrelation in circular bases are expected for polarization-entangled photons with a state $1/\sqrt{2}(|HH\rangle + |VV\rangle)$ which is equivalent to $1/\sqrt{2}(|DD\rangle + |AA\rangle) = 1/\sqrt{2}(|RL\rangle + |LR\rangle)$, where $|R\rangle = 1/\sqrt{2}(|H\rangle + i|V\rangle)$, $|L\rangle = 1/\sqrt{2}(|H\rangle - i|V\rangle)$, $|D\rangle = 1/\sqrt{2}(|H\rangle + |V\rangle)$, $|A\rangle = 1/\sqrt{2}(|H\rangle - |V\rangle)$ are right/left-hand circular, diagonal and antidiagonal polarization states, respectively. The calculated fidelity curve (see Supplementary Material) is shown in the bottom graph of Fig. 4c. By selecting correlation events around 0 ns delay value from the time window of 0.5 ns, the fidelity value was found to be 0.73±0.06 exceeding the classical limit of 0.5. The fidelity to the expected maximally entangled state of photons emitted from a nearly adjacent μLED QD with FSS of 0.7±0.5 μeV was found to be 0.69±0.06. Practical applications will require a triggered source of photons, where ideally a single pair of polarization-entangled photons would be generated upon request. Therefore Sample B1 was injected with pulsed current with a 63 MHz repetition rate (see Supplementary Material). Polarization-resolved second-order correlation curves obtained from a QD with a FSS of 0.2±0.2 μeV are shown in Fig. 4d. Expected correlations and degree of entanglement quantified by the fidelity value f=

0.678±0.023 confirmed the non-classical state of the photons. While the FSS value of this representative QD is small enough to have a substantial effect on entanglement degradation, a number of other phenomena are contributing. Among them are (1) a finite pulse-width of the current (1.4 ns) which partially causes repopulation of a QD and (2) a small background emission coming from the adjacent μLEDs. By using a time-gating technique, which could be defined as a selection of correlation events from a specific time window, the contribution of these phenomena can be significantly reduced. For example, by selecting events from a 1.5 ns window (shown in the inset of Fig. 4e) and preserving 75% of the total two-photon detection events, the fidelity increased to 0.823±0.019 (with a shorter time window of 0.1 ns, fidelity goes as high as 0.881±0.042, but care needs to be taken, as the photon statistics is also decreased). The taken correlation measurements allow a simplified estimation of three Bell parameters [37] used in quantum communication protocols [38]. By selecting correlation events from 1.5 ns window, the parameters were measured to be SRD=2.053±0.070, SDC=2.191±0.075 and SRC=2.239±0.074, all violating Bell's inequalities.

4.6 Conclusions and outlook

In summary, we have introduced a quantum photonics technology which potentially enables fabrication of site-controlled, scalable arrays of electrically driven sources of polarization-entangled photons with high entanglement quality. Compatibility with semiconductor fabrication technology, good reproducibility and control of the position make these devices attractive candidates for integrated photonic circuits for quantum information processing.

Nevertheless, work is needed to further improve our sources to achieve full capability in the contest of quantum information processing: achieving photon

indistinguishability across all devices, external control of the remaining fine-structure splitting, and enhancing photon extraction efficiency are among the top priorities. Strain with a possible combination of electric field [12][39] is one of the most promising tuning strategies of the emission energy and fine-structure splitting, which, we anticipate, already proved to be efficient within the first prototypes based on the Pyramidal QD system. The typically observed emission energy distribution (standard deviation of 2.5-3 meV) as in our sample(s) could be easily corrected by these methods, delivering the same excitonic emission energies for each Pyramid. Our short-term ambition will be dedicated to improving source tuneability, for example, by implementing a six-legged semiconductor-piezoelectric device, as in Ref.[40], also to achieve full control of the FSS associated to each Pyramid. Another critical parameter, the transition linewidth, which ideally is expected to be transform-limited, is indeed subject to the electric (and magnetic) fields present in the vicinity of a QD [24], including the external electric field applied for device operation. However, this is not a fundamental limitation, as it was already demonstrated that electrically driven QD devices can emit photons with a linewidth close to the theoretical limit [41]. By optimizing growth, device and interface design and processing conditions to minimize defect density and charge accumulation, high spectral purity is expected to be achieved. Indeed, a linewidth of a few μeV (resolution limited) from non-resonantly optically excited Pyramidal QDs was already demonstrated [25]. Finally, photon collection efficiency can be increased with proper on-chip lensing and waveguiding strategies [42][43][44], which potentially allow photon extraction efficiency up to 80%.

4.7 Supplementary Material

4.7.1. Sample growth and structure

The results presented in this letter were obtained from three samples, which are referred to as Sample A, Sample B1 and Sample B2. The latter two are from an identical epitaxial structure, but processed in different runs. The samples were grown by metalorganic vapour phase epitaxy (MOVPE) on (111)B oriented GaAs substrates pre-patterned by 7.5µm (Sample A) or 10µm (Sample B1(B2)) pitch pyramidal recesses [25] at the temperature of 730°C (thermocouple reading). As the growth on non-planar surface is governed by a complex precursor and adatom dynamics [19][20], a rich ensemble of interconnecting nanostructures self-forms within the recess during the growth of a stack of different composition epitaxial alloys (In/Al)GaAs [36]. The stacks of epitaxial layers with nominal thickness and alloy composition values are shown in Fig. 5. The first 4 layers of Sample B1(B2) are p-doped, followed by 5 intrinsic doping and 2 n-doping layers:

Growth direction

Sample A		
Nominal thickness (nm)	Material	Dopant (cm^{-3})
50	GaAs	C:5x10^{17}
25	$Al_{0.45-0.8}Ga_{0.55-0.2}As$	
80	$Al_{0.8}Ga_{0..7}As$	
15	GaAs	
50	$Al_{0.55}Ga_{0.45}As$	
45	$Al_{0.75}Ga_{0..25}As$	Undoped
100	GaAs	
0.6	$In_{0.25}Ga_{0.75}As$:N	
10	GaAs	
0.7	$In_{0.25}Ga_{0.75}As$:N	
50	GaAs	
45	$Al_{0.75}Ga_{0..25}As$	
30	$Al_{0.3}Ga_{0..7}As$	Si:5x10^{17}
10	GaAs	

Sample B1/B2		
Nominal thickness (nm)	Material	Dopant (cm^{-3})
40	GaAs	C:5x10^{17}
45	$Al_{0.45-0.8}GaAs$	C:5x10^{17}
90	$Al_{0.8}GaAs$	C:1x10^{18}
60	GaAs	C:1x10^{18}
45	$Al_{0.75}GaAs$	Undoped
90	GaAs	Undoped
0.55	$In_{0.25}GaAs$	Undoped
60	GaAs	Undoped
45	$Al_{0.75}GaAs$	Undoped
30	$Al_{0.3}GAs$	Si:1x10^{18}
10	GaAs	Si:1x10^{18}

Fig.5: Epitaxial structures reported in the main text. Sample B1(B2) presents the structure of entangled photon emitters. All alloy composition and layer thickness values are nominal.

- The first GaAs layer is a buffer meant to minimize the density of defect states and bury contaminants possibly transferred from the etched surface to the grown structure.
- A graded $Al_{0.45\rightarrow0.8}Ga_{0.55\rightarrow0.2}As$ and $Al_{0.8}Ga_{0.2}As$ are so-called etch-stop layers with high aluminum content meant to protect the inner materials from being chemically etched away during the selective GaAs substrate removing – the process called backetching (BE).
- A p-doped GaAs layer is optional and was included to test conditions for the best metal-semiconductor interface formation. After the selective GaAs substrate etching, the BE stop layers were removed by HF (30 s), exposing the p-doped GaAs layer for the evaporation of the metallic (titanium-gold) top layer for better Ohmic contact.
- The intrinsic $Al_{0.75}Ga_{0.25}As$ layer is included to form a selective current injection channel along the central axis of the pyramid – a vertical quantum wire – formed due to alloy segregation, to obtain ~ aluminum content < 0.3.
- The intrinsic GaAs is the quantum dot confinement barrier. A thick enough layer (90 nm) is sufficient to achieve a self-limiting profile – a flat base (~70 nm) which determines the lateral dimensions of a QD grown on it.
- $In_{0.25}Ga_{0.75}As$ is the QD layer sandwiched by GaAs. The real QD thickness is ~2.5-3 times bigger than nominal.

In the main text we mention “facet crowding”. With this term we intended the tendency of the system to create several new facets at the top of the structure to compensate for the different growth rates of the various surfaces, here the zero growth top (111)B and the side (111)A. While this effect has not been modeled yet for the case of the pyramidal system, in the parent system of V-groove quantum wires, the vicinal side (111)A are known to change their effective angle to compensate for the difference of intrinsic growth rate between the centre (100), the side vicinal (111)A and the top ridge (100) (see also Ref. [45]). This allows to maintain

material continuity, and a flat (111)A vicinal facet. If no "solution" to facet continuity exists in certain growth conditions, an extra (311) facet is known to appear to compensate and maintain material continuity.

We believe here we are observing a similar effect, even if at a greater scale than in the case of V-groove quantum wires.

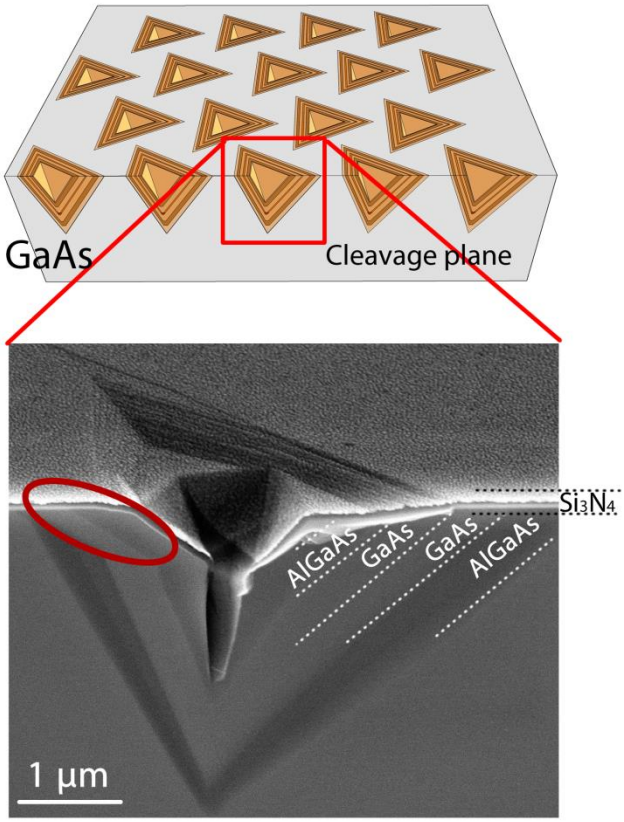


Figure 6: SEM image of a Pyramidal structure showing the epitaxial layers. It's a cross-section view of a single Pyramid cleaved to half. The encircled region shows the facet crowding region, i.e. a region were crystallographic facets form and quickly evolve deviating from the expected behavior, as also evidenced by the strong step bunching which developed visibly on the top region of the pyramidal recess.

4.7.2. Micro-LED fabrication

Fig.7 summarizes the µLED fabrication process, which requires a number of extra steps compared to the conventional case of LEDs based on self-assembled QDs. It should be anticipated that to increase the light extraction rate, the original substrate must be removed, and after the so-called back-etching (BE) the configuration of an LED will be an apex-up pyramid [46] (see Fig.7 step 6). The design of the sample structure and of the early processing steps had been done in consideration of this:

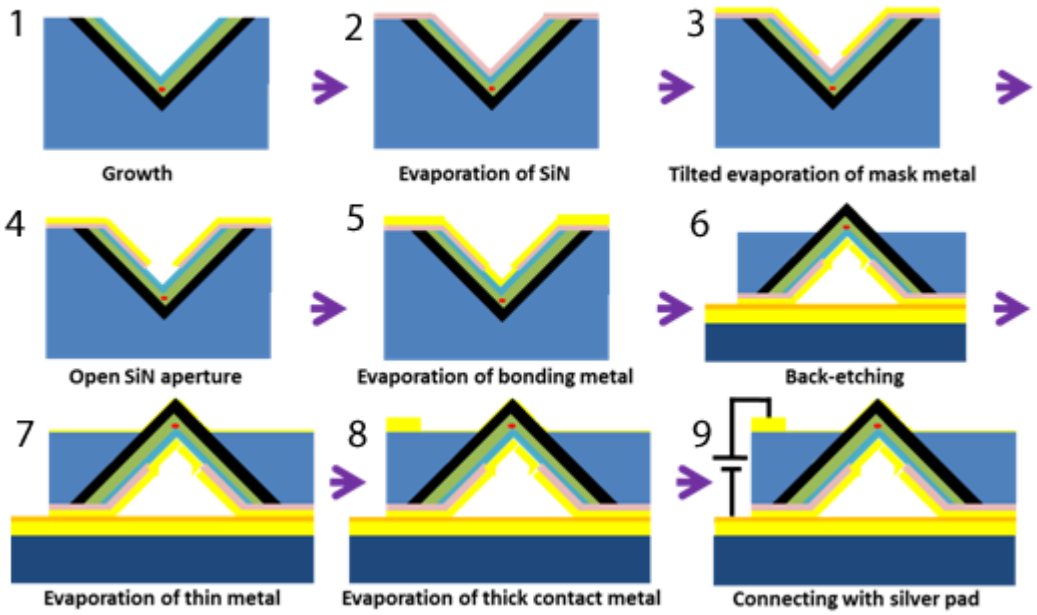


Figure 7: µLED fabrication steps.

1 After the pre-patterning of a semi-insulating GaAs (111)B substrates, a p-i-n structure was grown by MOVPE, with precursors and conditions similar to those reported elsewhere[23] , adding Si_2H_6 and CBr_4 as n-type and p-type dopants, respectively.

2 To prevent electrical shorts, first a layer of Si_3N_4 is deposited onto the as-grown sample.

3 Ti/Au layer of 3/15 nm is 3 times evaporated on a tilted sample, rotating it by 120° in growth plane each time. The final results is a mask metal leaving a small aperture of Si_3N_4 at the center of the recess.

4 This is then opened by CF_4 plasma etching.

5 Subsequently, a Ti/Au layer is evaporated as n-contact (and bonding) metal. To prepare for the BE, the sample is bonded onto another Ti/Au-coated GaAs substrate with the assistance of a SnAu ribbon via a reflow soldering process.

6 Apex-up pyramids appear after a subsequent conventional mechanical thinning and chemical etching (NH_4OH:H_2O_2) procedure [46] .

7 The contact metal for the diode p-side is a thin semi-transparent Ti/Au layer (1/20 nm), to maintain good light extraction efficiency.

8 A thick layer of Au is evaporated for a wire bonding.

9 A wire connection is made simply by using a Kapton coated wire connected to the connection region with silver paint.

4.7.3. Measurements

Measurements were taken at 10 K using a helium closed-cycle cryostat. Electroluminescence was collected in a standard micro-photoluminescence set-up, using 100x magnification, a 0.80 NA long-working-distance objective, which enabled probing a single device at a time.

The fine-structure splitting measurements were taken by using a combined multiple measurement and fitting procedure [37]. Linear polarization components were analysed by placing a polarizer in front of the monochromator and rotating a half-wave plate with a step of 1.5 deg. Exciton and biexciton transitions were fitted with Lorentzian fits; the corresponding peak centres were subtracted and the resulting data fitted by a sinusoid curve, where its amplitude is equal to the FSS value. The

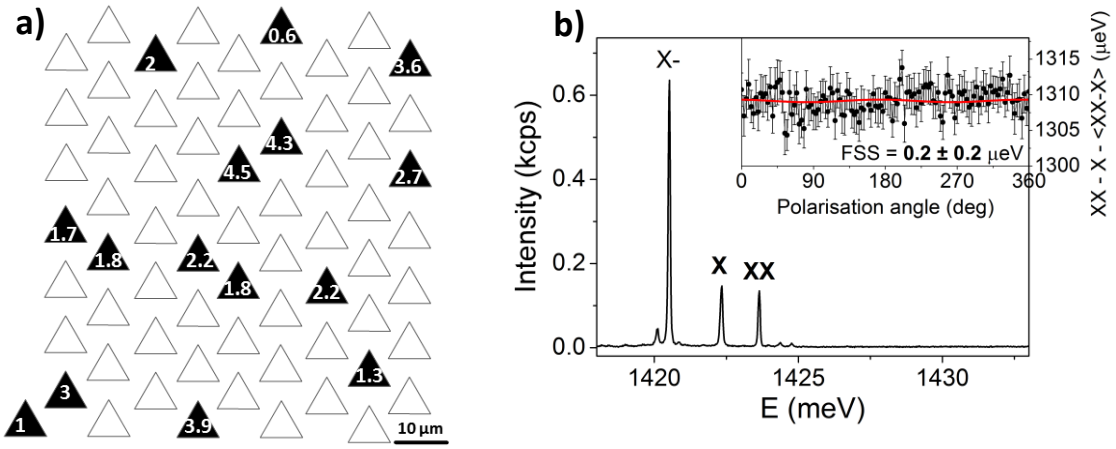


Figure 8: a) The map of functional LEDs and FSS distribution. b) A typical FSS measurement.

standard deviation was taken as an error. An extra map of functional (black triangles) µLEDs is shown in Fig.8a. The numbers are the fine-structure splitting (FSS) values. Fig.8b shows a typical FSS measurement

Polarization-entanglement was measured by discriminating exciton and biexciton transitions with two monochromators acting as narrow band-pass filters. Polarization projections were selected by an appropriate orientation of half-(quarter-)wave plates to the respect of polarizing beam-splitters placed after the monochromators equipped with 950 grooves/mm gratings (TE/TM diffracted intensity ratio ~1 at 877 nm). Fiber-coupled avalanche-photo diodes were used to detect intensity at a single photon level. In such configuration, two polarization-resolved, second-order correlation curves were measured simultaneously. The error propagation to g(2), fidelity values has been estimated by using a Poissonian uncertainty.

In pulsed excitation mode, samples were injected by pulses shaped with a positive DC offset set slightly below the µLED injection threshold (typically a few volts), with superimposed pulses of 1.4 ns width, reaching maximum voltage as high as 20 V and repetition rate between 63 MHz and 80 MHz. A typical polarization-entangled photon pair detection rate in these experimental conditions was ~1000 pairs/hour, with

overall estimated extraction efficiency from our structures ~ 1%. The final counts are also affected by the ~1.4% efficiency of our μPL set-up and a broad non-Gaussian μLED emission profile.

4.7.4. Fidelity and Bell parameters calculation

Typically the two-photon polarization state can be estimated by a quantum state tomography procedure [47] which allows reconstruction of a density matrix ρ from a set of 16 intensity measurements. Since the expected maximally entangled state $|\psi\rangle = 1/\sqrt{2}(|HH\rangle + |VV\rangle)$ is known, the procedure can be simplified by reducing the number of measurements, which allows obtaining only the density matrix elements necessary to calculate the fidelity $f = \langle\psi|\rho|\psi\rangle$ of the entangled state $|\psi\rangle$: $f = 1/4(1 + C_R + C_D - C_C)$, where C_R, C_D and C_C are degrees of correlations taken in rectilinear, diagonal and circular polarization bases [31][47]. The degree of correlation is defined as $C_{basis} = (g^2_{xx,x} - g^2_{xx,\bar{x}})/(g^2_{xx,x} + g^2_{xx,\bar{x}})$, where $g^2_{xx,x\,(\bar{x})}$ is the second-order correlation function with $xx(x)$ being polarization of a biexciton (exciton) and $\bar{x}$ being orthogonal polarization of an exciton. A fidelity value greater than 0.5 is a quick indicator of entanglement.

The degrees of correlation C_R, C_D and C_C are used to calculate the simplified Bell parameters [37]. Without the aim to rule-out local hidden-variable theories, the traditional CHSH form [49] of inequality obtained from the measurements with four different combinations of polarizers, can be simplified and expressed as $S_{RD} = \sqrt{2}(C_R + C_D) \leq 2$. Two more different Bell parameters are calculated and known as $S_{DC} = \sqrt{2}(C_D + C_C) \leq 2$ and $S_{RC} = \sqrt{2}(C_R - C_C) \leq 2$.

4.7.5. Current density simulations

Finite element method simulations were performed using COMSOL Multiphysics 5.0. The simulations were obtained by solving the Poisson's equation in conjunction with the continuity equations in order to calculate the voltage and carrier density (electrons and holes) in a 2D geometry (described below). Rotational symmetry along the vertical direction was applied to confer a 3D structure to the simulated geometry and improve the approximation to the real pyramidal structure. The 2D geometry consisted of half cross section of a regular triangular pyramid with side length of 7μm cut along the centre of a face. The vertical wire in the centre of the 3D geometry was approximated to a cylinder with diameter of 100 nm. The simulated structure has 7 internal layers which are (starting from the top layer in Fig. 1d): GaAs with thickness 60 nm, $Al_xGa_{1-x}As$ with $x = 0.75$ and thickness 45 nm, GaAs with thickness 90 nm, $In_{0.25}Ga_{0.75}As$ with thickness 1 nm, GaAs with thickness 60 nm, $Al_xGa_{1-x}As$ with $x = 0.75$ and thickness 45 nm and finally $Al_xGa_{1-x}As$ with $x = 0.3$ and thickness 30 nm. In the vertical quantum wire the Al concentrations in the different layers were reduced to include the segregation effects [19]: $x = 0.3$ were substituted with $x = 0.05$, and $x = 0.75$ were substituted with $x = 0.26$. The top layer was p-doped with concentration $1{\cdot}10^{18}$ cm^{-3} and the external surface was set at constant voltage of 1.5 V. The bottom layer was n-doped with concentration $1{\cdot}10^{18}$ cm^{-3} and set at ground. The current density values reported in Fig. 1d are the nodal value calculated from the electric field distribution E and the conductivity σ using the relation $J = \sigma E$.

References

[1] J. L. O'Brien, A. Furusawa, and J. Vučković, *Nat. Photonics*, vol. 3, no. 12, pp. 687–695, Dec. 2009.

[2] N. Gisin and R. Thew, *Nat. Photonics*, vol. 1, no. 3, pp. 165–171, Mar. 2007.

[3] A. Aspuru-Guzik and P. Walther, *Nat. Phys.*, vol. 8, no. 4, pp. 285–291, Apr. 2012.

[4] T. D. Ladd, F. Jelezko, R. Laflamme, Y. Nakamura, C. Monroe, and J. L. O'Brien, *Nature*, vol. 464, no. 7285, pp. 45–53, Mar. 2010.

[5] P. Michler, A. Kiraz, C. Becher, W. V Schoenfeld, P. M. Petroff, L. Zhang, E. Hu, and A. Imamoglu, *Science*, vol. 290, no. 5500, pp. 2282–5, Dec. 2000.

[6] C. Santori, D. Fattal, J. Vučković, G. S. Solomon, and Y. Yamamoto, *Nature*, vol. 419, no. 6907, pp. 594–597, Oct. 2002.

[7] N. Akopian, N. H. Lindner, E. Poem, Y. Berlatzky, J. Avron, D. Gershoni, B. D. Gerardot, and P. M. Petroff, *Phys. Rev. Lett.*, vol. 96, no. 13, p. 130501, Apr. 2006.

[8] R. J. Young, R. M. Stevenson, P. Atkinson, K. Cooper, D. A. Ritchie, and A. J. Shields, *New J. Phys.*, vol. 8, no. 2, pp. 29–29, Feb. 2006.

[9] R. Hafenbrak, S. M. Ulrich, P. Michler, L. Wang, A. Rastelli, and O. G. Schmidt, *New J. Phys.*, vol. 9, no. 9, pp. 315–315, Sep. 2007.

[10] A. Dousse, J. Suffczyński, A. Beveratos, O. Krebs, A. Lemaître, I. Sagnes, J. Bloch, P. Voisin, and P. Senellart, *Nature*, vol. 466, no. 7303, pp. 217–220, Jul. 2010.

[11] G. Juska, V. Dimastrodonato, L. O. Mereni, A. Gocalinska, and E. Pelucchi, *Nat. Photonics*, vol. 7, no. 7, pp. 527–531, May 2013.

[12] R. Trotta, J. S. Wildmann, E. Zallo, O. G. Schmidt, and A. Rastelli, *Nano Lett.*, vol. 14, no. 6, pp. 3439–3444, Jun. 2014.

[13] T. Kuroda, T. Mano, N. Ha, H. Nakajima, H. Kumano, B. Urbaszek, M. Jo, M. Abbarchi, Y. Sakuma, K. Sakoda, I. Suemune, X. Marie, and T. Amand, *Phys. Rev. B*, vol. 88, no. 4, p. 041306, Jul. 2013.

[14] M. A. M. Versteegh, M. E. Reimer, K. D. Jöns, D. Dalacu, P. J. Poole, A. Gulinatti, A. Giudice, and V. Zwiller, *Nat. Commun.*, vol. 5, no. 1, p. 5298, Dec. 2014.

[15] A. Boretti, L. Rosa, A. Mackie, and S. Castelletto, *Adv. Opt. Mater.*, vol. 3, no. 8, pp. 1012–1033, Aug. 2015.

[16] C. L. Salter, R. M. Stevenson, I. Farrer, C. A. Nicoll, D. A. Ritchie, and A. J. Shields, *Nature*, vol. 465, no. 7298, pp. 594–597, 2010.

[17] J. Zhang, J. S. Wildmann, F. Ding, R. Trotta, Y. Huo, E. Zallo, D. Huber, A. Rastelli, and O. G. Schmidt, *Nat. Commun.*, vol. 6, p. 10067, Dec. 2015.

[18] G. Juska, E. Murray, V. Dimastrodonato, T. H. Chung, S. T. Moroni, A. Gocalinska, and E. Pelucchi, *J. Appl. Phys.*, vol. 117, no. 13, p. 134302, Apr. 2015.

[19] E. Pelucchi, V. Dimastrodonato, A. Rudra, K. Leifer, E. Kapon, L. Bethke, P. A. Zestanakis, and D. D. Vvedensky, *Phys. Rev. B*, vol. 83, no. 20, p. 205409, May 2011.

[20] V. Dimastrodonato, E. Pelucchi, and D. D. Vvedensky, *Phys. Rev. Lett.*, vol. 108, no. 25, p. 256102, Jun. 2012.

[21] S. T. Moroni, V. Dimastrodonato, T.-H. Chung, G. Juska, A. Gocalinska, D. D. Vvedensky, and E. Pelucchi, *J. Appl. Phys.*, vol. 117, no. 16, p. 164313, Apr. 2015.

[22] Q. Zhu, E. Pelucchi, S. Dalessi, K. Leifer, M.-A. Dupertuis, and E. Kapon, *Nano Lett.*, vol. 6, no. 5, pp. 1036–1041, May 2006.

[23] V. Dimastrodonato, L. O. Mereni, R. J. Young, and E. Pelucchi, *Phys. Status Solidi B-Basic Solid State Phys.*, vol. 247, no. 8, pp. 1862–1866, 2010.

[24] A. V. Kuhlmann, J. Houel, A. Ludwig, L. Greuter, D. Reuter, A. D. Wieck, M. Poggio, and

R. J. Warburton, *Nat. Phys.*, vol. 9, no. 9, pp. 570–575, Jul. 2013.

[25] L. O. Mereni, V. Dimastrodonato, R. J. Young, and E. Pelucchi, *Appl. Phys. Lett.*, vol. 94, no. 22, p. 223121, Jun. 2009.

[26] O. Benson, C. Santori, M. Pelton, and Y. Yamamoto, *Phys. Rev. Lett.*, vol. 84, no. 11, pp. 2513–2516, Mar. 2000.

[27] E. Moreau, I. Robert, L. Manin, V. Thierry-Mieg, J. M. Gérard, and I. Abram, *Phys. Rev. Lett.*, vol. 87, no. 18, p. 183601, Oct. 2001.

[28] A. Schliwa, M. Winkelnkemper, and D. Bimberg, *Phys. Rev. B*, vol. 76, no. 20, p. 205324, Nov. 2007.

[29] R. Seguin, A. Schliwa, S. Rodt, K. Pötschke, U. W. Pohl, and D. Bimberg, *Phys. Rev. Lett.*, vol. 95, no. 25, p. 257402, Dec. 2005.

[30] M. Abbarchi, C. A. Mastrandrea, T. Kuroda, T. Mano, K. Sakoda, N. Koguchi, S. Sanguinetti, A. Vinattieri, and M. Gurioli, *Phys. Rev. B*, vol. 78, no. 12, p. 125321, Sep. 2008.

[31] W. Langbein, P. Borri, U. Woggon, V. Stavarache, D. Reuter, and A. D. Wieck, *Phys. Rev. B*, vol. 69, no. 16, p. 161301, Apr. 2004.

[32] A. J. Hudson, R. M. Stevenson, A. J. Bennett, R. J. Young, C. A. Nicoll, P. Atkinson, K. Cooper, D. A. Ritchie, and A. J. Shields, *Phys. Rev. Lett.*, vol. 99, no. 26, p. 266802, Dec. 2007.

[33] A. J. Bennett, M. A. Pooley, R. M. Stevenson, M. B. Ward, R. B. Patel, A. B. de la Giroday, N. Sköld, I. Farrer, C. A. Nicoll, D. A. Ritchie, and A. J. Shields, *Nat. Phys.*, vol. 6, no. 12, pp. 947–950, Dec. 2010.

[34] J. D. Plumhof, V. Křápek, F. Ding, K. D. Jöns, R. Hafenbrak, P. Klenovsk, A. Herklotz, K. Dörr, P. Michler, A. Rastelli, and O. G. Schmidt, *Phys. Rev. B*, vol. 83, no. 121302, 2011.

[35] R. Trotta, E. Zallo, C. Ortix, P. Atkinson, J. D. Plumhof, J. Van Den Brink, A. Rastelli, and O. G. Schmidt, *Phys. Rev. Lett.*, vol. 109, no. 14, p. 147401, Oct. 2012.

[36] K. F. Karlsson, M. A. Dupertuis, D. Y. Oberli, E. Pelucchi, A. Rudra, P. O. Holtz, and E. Kapon, *Phys. Rev. B*, vol. 81, no. 16, p. 161307, Apr. 2010.

[37] R. J. Young, R. M. Stevenson, A. J. Hudson, C. A. Nicoll, D. A. Ritchie, and A. J. Shields, *Phys. Rev. Lett.*, vol. 102, no. 3, p. 030406, Jan. 2009.

[38] A. K. Ekert, *Phys. Rev. Lett.*, vol. 67, no. 6, pp. 661–663, Aug. 1991.

[39] J. Zhang, E. Zallo, B. Höfer, Y. Chen, R. Keil, M. Zopf, S. Böttner, F. Ding, and O. G. Schmidt, *Nano Lett.*, vol. 17, no. 1, pp. 501–507, Jan. 2017.

[40] R. Trotta, J. Martín-Sánchez, J. S. Wildmann, G. Piredda, M. Reindl, C. Schimpf, E. Zallo, S. Stroj, J. Edlinger, and A. Rastelli, *Nat. Commun.*, vol. 7, p. 10375, Jan. 2016.

[41] R. M. Stevenson, C. L. Salter, J. Nilsson, A. J. Bennett, M. B. Ward, I. Farrer, D. A. Ritchie, and A. J. Shields, *Phys. Rev. Lett.*, vol. 108, no. 4, p. 040503, Jan. 2012.

[42] Y. Ma, P. E. Kremer, and B. D. Gerardot, *J. Appl. Phys.*, vol. 115, no. 2, p. 023106, Jan. 2014.

[43] M. Gschrey, A. Thoma, P. Schnauber, M. Seifried, R. Schmidt, B. Wohlfeil, L. Krüger, J.-H. Schulze, T. Heindel, S. Burger, F. Schmidt, A. Strittmatter, S. Rodt, and S. Reitzenstein, *Nat. Commun.*, vol. 6, no. 1, p. 7662, Dec. 2015.

[44] N. Lindenmann, G. Balthasar, D. Hillerkuss, R. Schmogrow, M. Jordan, J. Leuthold, W. Freude, and C. Koos, *Opt. Express*, vol. 20, no. 16, p. 17667, Jul. 2012.

[45] V. Dimastrodonato, E. Pelucchi, P. A. Zestanakis, and D. D. Vvedensky, *Appl. Phys. Lett.*, vol. 103, no. 4, p. 042103, Jul. 2013.

[46] M. H. Baier, E. Pelucchi, E. Kapon, S. Varoutsis, M. Gallart, I. Robert-Philip, and I. Abram, *Appl. Phys. Lett.*, vol. 84, no. 5, pp. 648–650, Feb. 2004.

[47] D. F. V. James, P. G. Kwiat, W. J. Munro, and A. G. White, *Phys. Rev. A*, vol. 64, no. 5, p. 052312, Oct. 2001.

[48] A. J. Shields, R. M. Stevenson, and R. J. Young, *Single Semicond. Quantum Dots*, pp. 227–265, 2009.

[49] J. F. Clauser, M. A. Horne, A. Shimony, and R. A. Holt, *Phys. Rev. Lett.*, vol. 23, no. 15, pp. 880–884, Oct. 1969.

Chapter 5
On-demand single-photons from electrically-injected site-controlled Pyramidal Quantum Dots

Chapter based on the journal article submitted to:

Journal of Physics D: Applied Physics

S. T. Moroni, T. H. Chung, G. Juska, A. Gocalinska, and E. Pelucchi

Tyndall National Institute, University College Cork, Dyke Parade, Cork, Ireland

Abstract

We report on the performance of electrically-injected Pyramidal Quantum Dots in terms of single-photon emission. We previously presented the generation of entangled photon pairs from similarly structured devices. Here we show that it is also possible to obtain single-photons upon continuous wave excitation as well as pulsed excitation, obtaining a low $g^2(0)$ *of 0.088±0.059, by discarding re-excitation events within a single excitation pulse by applying time-gating techniques.*

5.1. Introduction

Integration, scalability, reproducibility and high quantum state fidelities: these are some of the main technological challenges to be tackled in order to achieve a realistic source of photons to be employed in quantum computation [1][2]. Semiconductor quantum dot (QD)-based light sources have recently been gaining great relevance in this perspective, as they can be employed for the generation of quantum light while allowing for processing by means of standard semiconductor-based fabrication and integration techniques. Semiconductor QDs have been demonstrated as sources of single photons [3][4][5], highly indistinguishable photons [6][7], entangled photon pairs with high fidelity [8][9][10], time-bin entangled photons [11] and more, thanks to their versatility and tunability. In addition to this, among the requirements for a QD-based technology for quantum computation, efficient electrical injection would allow an extremely simplified excitation scheme and therefore easier QD integration.

Electroluminescence from semiconductor QDs has been reportedly achieved in the past [12], together with electrically driven single photon emission [13][14] and entangled photon emission [9][15], but only a few reported cases claimed to be site controlled as well [16][17]. Although, in most of these cases, it was generally about the possibility to statistically control the self-assembled QDs position, while the only instance of true deterministic site control of the electrically driven QDs was based on Pyramidal Quantum Dots (PQDs) [18][19], but without proof of single photon emission. Note also that references [18][19] discuss two different pyramidal site controlled material systems, each showing different challenges of their own, one based on AlGaAs barriers [20], the other on GaAs barriers.

Here we report for the first time on the possibility of generating single photons by embedding PQDs into a PIN-junction device, a structure largely similar to previous designs for entangled photon emission reported in [19], and therefore proving single photon electrically driven emission from a true site-controlled QD system. Besides

the statistic regarding directly single-photon emission quality, we find that our analysis also provides interesting insight on the ability of filtering photon detection events to improve the performance of our devices. Our findings suggest, after a comparison with previous work on entangled-photon emission through electrical injection, that a good entangled photon emitter from QDs is not necessarily also a good single photon emitter (and, obviously, vice versa). We address this point more in detail further in our contribution.

5.2. Fabrication and characterization methods

PQDs are fabricated starting from a (111)B GaAs wafer using a lithography based patterning technique to form an ordered array of inverted pyramidal recesses; Metalorganic Vapor Phase Epitaxy is then performed, allowing for the site control of the QDs, one for each recess. More recently we developed a more advanced type of device design for the realization of electrical injection. As detailed elsewhere [19], the QD is embedded into the intrinsic region of the PIN junction, whose detailed structure is reported in the supplementary material. The complex geometry and copiousness of nanostructure formation (e.g. lateral quantum wires formed along the edges of the pyramidal recess and lateral quantum wells formed along its sidewalls, see [21] and references therein) of the pyramidal system makes it necessary to perform a number of processing steps to achieve the proper electrical contacting of the devices: insulation of the corners of the pyramid, masking of the insulation through tilted Au evaporation, selective removal of the insulation, N-side contacting, back-etching [22], and P-side contacting. For simplicity of fabrication, the scheme relies on the simultaneous contacting of all the pyramidal QD devices, which share the same top and bottom contacts and therefore share the same applied electrical bias. Henceforth the electrical properties of the device we will refer to in this paper will be the total ensemble current vs. voltage characteristics. A typical I-V curve for

one of our devices is shown in Fig.1b (inset), where it can be seen that the exponential rise in the current is obtained at about 6 V.

It is worth underling at this point the possible origin of the high turn-on voltage in our devices, compared to similar LED devices [23][9]. On one hand, the metal used for the metallization of the GaAs P-doped layer is not ideal and might be causing a Schottky barrier [24]. On the other hand, the carriers have to be channeled through a Ga-rich AlGaAs vertical quantum wire with a very small cross-section (<40 nm diameter through the centre of the pyramid) [19], which might cause a high resistance,

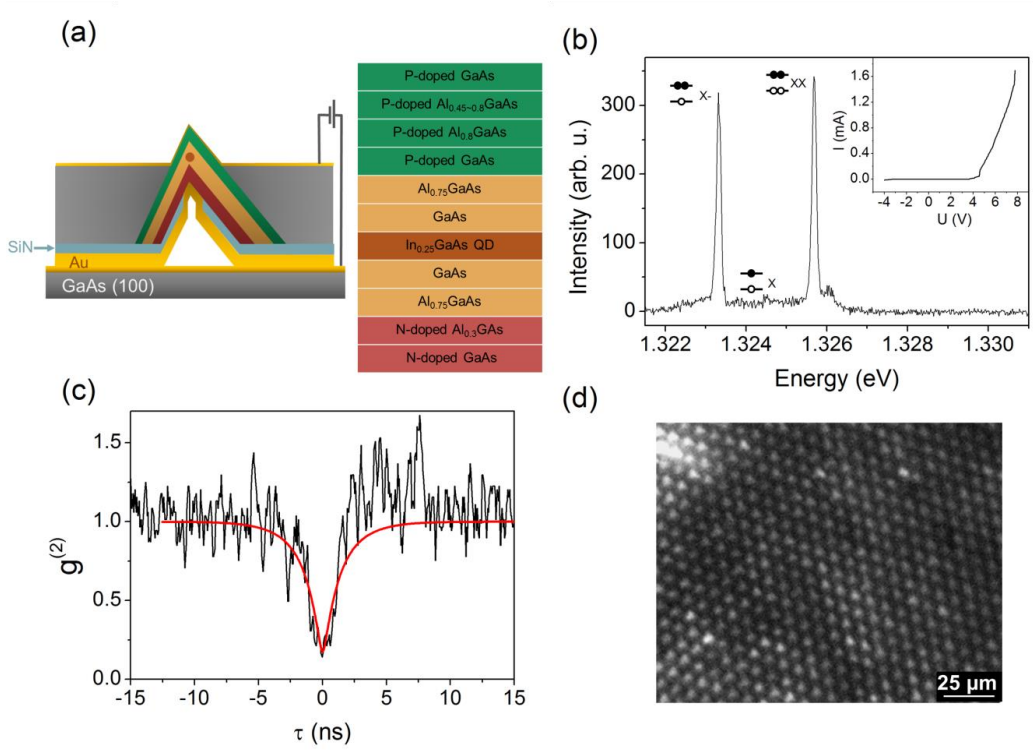


Fig.1: a) a sketch of a structure of a PQD-based LED; b) representative spectrum from an electrically injected PQD, showing a dominant X- behavior and an almost suppressed X and (inset) typical IV response of a PQD-based LED; c) autocorrelation for the X- transition from an electrically-driven PQD under DC bias excitation (black line) and fitting of the data using a $g^2(\tau)$ function convoluted with the response function for the measurement apparatus; d) CCD image of lit PQD-LEDs under DC bias excitation.

although forcing the carrier through the centre of the structure, towards the QD. It is also relevant to note that different QDs could show different turn-on voltages: this is mainly due to the spread in etching depth of the original GaAs substrate on the top of each pyramid, resulting from the back-etching process. Each pyramidal structure presents a slightly different open area on the N-and P-doped regions for contacting, therefore leading to a distribution of surface resistances, from which the difference in turn-on voltages.

The QDs were analyzed by low-temperature (10K) micro-electroluminescence spectroscopy using a 100x magnification objective with a numerical aperture of 0.8, allowing for the spatial filtering of the light coming from different PQDs (which had a spacing of 10 μm) simply by scanning on the sample surface by means of piezoelectric actuators. Although the turn-on voltage was slightly different for each individual PQD diode, this was typically around 6 V; voltage at which it was possible to detect excitonic transitions.

5.3. Results and discussion

Fig.1b shows a representative spectrum from an electrically injected PQD under DC excitation. We identify each transition as exciton (X), biexciton (XX) and a negatively charged exciton (X-; based on previous results [25] where negatively charged excitons and positively charged excitons were systematically identified also by employing a second wavelength excitation for the release of extra holes in the surrounding of the QD), which is typically the predominant transition in terms of intensity. In some cases the exciton was completely suppressed by the excess of negative charges [25]. When operating in DC, it was possible to obtain single-photons from the X- transition, for example. We chose this transition to test for single photon emission mostly as it was the brightest transition of the excitonic ensemble, typically showing at least 3 times

the exciton overall intensity, but also because the trion transition is ideally the more suited for single photon emission, not being subject to special selection rules [26]. Moreover, the X- transition is more suitable for the generation of indistinguishable photons, as it is not affected by a fine structure splitting and therefore more often studied for indistinguishability studies (see for example [27]).

A standard HBT setup was employed for autocorrelation measurement. One representative case is shown in Fig.1c. Upon the application of 6.8 V, the $g^2(0)$ autocorrelation function reaches 0.17, which has been fitted taking into account the detector response function (a Gaussian response with 400 ps FWHM).

In order to operate the device in pulsed excitation - and prove on demand generation of single photons - we applied a DC bias on the top of which we superimposed the AC pulses. From the I-V curve we can deduce the resistance of the device when the turn-on has been reached, which falls in the kΩ range. This high resistance causes a high impedance mismatch between the LEDs and the pulse generator (which has a standard 50 Ω output resistance). The mismatch could result in reflections of the signal at the device and re-excitation pulses. Since individual QDs had diverse turn-on voltages, different settings of the pulse generator (frequency, DC and AC voltages) resulted in different behaviors of the device in terms e.g. of intensity of the spectrum features and single-photon emission performance. For instance, an inefficient or insufficiently high excitation level leads to a low-intensity spectrum, while an excessive population of the QD would result in a quick re-excitation of the same transition. At different DC and AC voltage levels, the response of the whole apparatus and QD system had a different response also in terms of pulse reflections along the line, making it necessary to tune the excitation frequency as well. Therefore ad hoc settings had to be chosen for each individual QD. Nonetheless, in most of the cases it was possible to find a set of parameters for which the PQD could be operated in pulsed excitation in a good regime for single-photon emission.

Fig. 2 shows a representative case: in order to operate the device in pulsed excitation, we applied a DC bias of 0.85 V on the top of which we superimposed a pulse of 8.67 V and 1.425 ns pulse width with a frequency of 66 MHz. The autocorrelation from this type of excitation is presented in Fig.2b: $g^2(0)$ is 0.185±0.057. As it can be seen in the

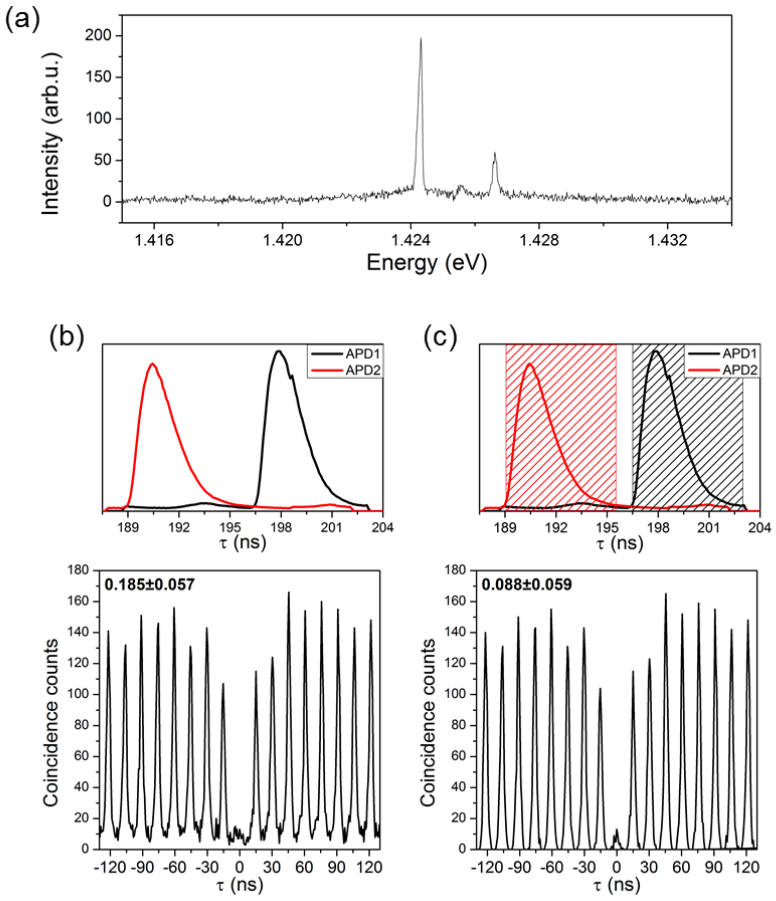


Fig.2: a) Emission dynamics of a PQD under pulsed electrical injection; b) to c) lifetime measurement for the two detectors employed (top) and autocorrelation measurement (bottom) in pulsed excitation selecting different time windows (highlighted in the top graph) within one excitation pulse period for the time gating filtering process: all detection events are selected in b), second-pulses events are discarded in c) by selecting a time window of 6.5 ns; the resulting $g^2(0)$ for each case is shown in the inset of the corresponding graph.

time-dependence in Fig.2, reflections along the line often caused a low intensity second pulse. A time-gating technique was then employed in order to discard such second pulsing event. In this case, the correlation curves were obtained by recording all photon detection events in a time tag mode, followed by a post-construction procedure of the correlation curve [28]. This method allowed testing correlations of photons from different time windows using the raw data obtained at exactly the same experimental conditions. Fig.2c shows the autocorrelation obtained by considering detection events falling only in a determined time window (*time gating*). With a 6.5 ns wide window, the $g^2(0)$ improves significantly to 0.088±0.059), which if corrected for noise levels and detectors time resolution, is effectively a very low value.

Finally, we would like to discuss briefly the different filtering approaches employed in this work and in our previous work on the electrical excitation of PQDs for entangled photon emission [19]. While in this paper we applied a standard time gating technique (as e.g. in [29]) which allows filtering the detection events based on the lifetimes to discard re-excitation events and "restore" the single photon quality, in our previous work [19] we applied a different approach. In [19] we selected a time-window from the correlation measurement itself rather than from the lifetimes, therefore filtering time events based on the direct time difference between the detection of biexciton and exciton related photons coming in sequence in the cascade. This other time-filtering technique allows selecting fast transitions between exciton and biexciton and, if a narrow enough time-window is selected, it discards biexciton re-excitation events, which is necessary but not sufficient to result in single-photon emission. Selecting photons based on the time separation of the biexciton and exciton means to discard background events coming from any type of source of contamination of the correlation and filter the photons which are part of an entangled pair even if they wouldn't be per se single photon events. We could think of this method as of a specific filter for the selection of biexciton-exciton detection

events correlated through a direct cascade. To provide an intuitive example, rapid re-excitation of biexciton might occur, followed by a recombination cascade which actually results in entangled photon pair emission, properly selected by the method employed in [19], although the biexciton second photon would degrade the single photon statistics (a similar argument might be employed for exciton re-excitation) and would be discarded in standard time-gating techniques like the one employed in this paper, depending on the selected time-window.

Although it might seem trivial, this was previously unreported for this specific case (and could effectively be useful for practical purposes), while, to some extent, has similarities to what is called, in down-conversion processes, photon heralding (see e.g. [30]). The successful application of this post-selection technique used in [19] means in principle that perfect single photon emission is not required to obtain high fidelity (>0.8) entangled photons. Our conclusion is that, although perfect entangled-photon emission is definitely limited by single photon pair quality, generally, high fidelity entanglement can be obtained from non-perfect single-photon emitting devices if the correct events are selected.

5.4. Conclusion

In conclusion, we showed the single photon emission performance of PQDs under both DC and pulsed electrical excitation, yielding respectively a $g^2(0)$ of 0.17 and 0.185. In pulsed excitation, the application of a simple time gating technique allowed to discard re-excitation events and obtain a $g^2(0)$ of 0.088, therefore proving that it is possible in principle to achieve a high quality single photon emission from our devices. Further improvements will be the subject of future research, and could be achieved either by employing even shorter pulses or improving the overall injection of the PQD, for example reducing the contact resistance or producing smaller pyramids.

5.5. Supplementary material: Sample structure

The results presented in this manuscript were obtained from two samples, which are referred to as Sample A and Sample B, whose structure is shown in Fig.S1. Sample A resulted in the best DC-injected single photon emission presented in the main text, while PQDs from sample B provided the best results in terms of pulsed excitation.



Sample A

Nominal thickness (nm)	Material	Dopants (cm^{-3})
70	GaAs	Undoped
10	GaAs	C: $5x10^{17}$
45	$Al_{0.45\sim0.8}GaAs$	
90	$Al_{0.8}GaAs$	
40	$Al_{0.55}GaAs$	
60	$Al_{0.7}GaAs$	Undoped
50	GaAs	
1.2	$In_{0.25}GaAs$	
30	GaAs	
50	$Al_{0.55}GaAs$	
35	$Al_{0.3}GaAs$	Si: $5x10^{17}$
10	GaAs	

Sample B

Nominal thickness (nm)	Material	Dopants (cm^{-3})
40	GaAs	C: $5x10^{17}$
45	$Al_{0.45\sim0.8}GaAs$	
90	$Al_{0.8}GaAs$	C: $1x10^{18}$
60	GaAs	
45	$Al_{0.75}GaAs$	Undoped
90	GaAs	
0.55	$In_{0.25}GaAs$	
60	GaAs	
45	$Al_{0.75}GaAs$	
30	$Al_{0.3}GAs$	Si: $1x10^{18}$
10	GaAs	

Fig.S1: Epitaxial structures relative to the PQD samples reported in the main text. All alloys' compositions, layers' thickness and doping concentration values are nominal.

The samples were grown by metalorganic vapour phase epitaxy (MOVPE) at a (thermocouple read) temperature of 730°C on (111)B-oriented GaAs substrates which were pre-patterned with 7.5 µm (Sample A) or 10 µm (Sample B) pitch pyramidal recesses.

In each of the structures, each layer fulfills a specific purpose:

- The initial GaAs layer was used as a buffer to minimize the influence of defect states (e.g. impurities, point defects), present on the as-etched pyramidal recesses, on the QD.
- A graded Al0.45→0.8Ga0.55→0.2As layer and an Al0.8Ga0.2As layer were the so-called etch-stop layers with high aluminum contents, meant to protect the inner layers from being chemically etched during the selective GaAs substrate removal (backetching).
- A p-doped GaAs layer can be optional (included in sample B and not in sample A); after the backetching it can be removed by means of HCl acid (30 s), allowing the exposure of the p-doped GaAs layer for the evaporation of the metallic (gold) top layer for better quality contact.
- The intrinsic Al0.75Ga0.25As/Al0.7Ga0.3As layer was included to form a Ga-rich vertical quantum wire formed due to alloy segregation, yielding an aluminum content < 0.3 in the center of the pyramid to allow the selective current injection.
- The intrinsic GaAs was the quantum dot confinement barrier. Based also on growth modeling simulations, the ~(111)B lateral profile on which the InGaAs QD layer was grown was around 70 nm. It can be noted that the lateral/vertical nominal thickness of the QD didn't have a noticeable effect (in the experiments we performed aside of the ones reported here) on the injection efficiency or single-photon performance, which was instead mostly affected by the structure surrounding the QD. It should also be noted that the GaAs self-limited profile drives the dot lateral size, and only changes marginally with the growth temperature, while the dot thickness is the only actual "free" parameter here.
- The n-doped region was then deposited, made of an AlGaAs layer followed by a GaAs capping layer to prevent oxidation.

References

[1] P. Kok, W. J. Munro, K. Nemoto, T. C. Ralph, J. P. Dowling, and G. J. Milburn, *Rev. Mod. Phys.*, vol. 79, no. 1, pp. 135–174, Jan. 2007.

[2] I. L. Chuang and D. Gottesman, *Nature*, vol. 402, no. 6760, pp. 390–393, Nov. 1999.

[3] P. Michler, A. Kiraz, C. Becher, W. V Schoenfeld, P. M. Petroff, L. Zhang, E. Hu, and A. Imamoglu, *Science*, vol. 290, no. 5500, pp. 2282–5, Dec. 2000.

[4] N. Somaschi, V. Giesz, L. De Santis, J. C. Loredo, M. P. Almeida, G. Hornecker, S. L. Portalupi, T. Grange, C. Antón, J. Demory, C. Gómez, I. Sagnes, N. D. Lanzillotti-Kimura, A. Lemaítre, A. Auffeves, A. G. White, L. Lanco, and P. Senellart, *Nat. Photonics*, vol. 10, no. 5, pp. 340–345, May 2016.

[5] L. Schweickert, K. D. Jöns, K. D. Zeuner, S. F. Covre da Silva, H. Huang, T. Lettner, M. Reindl, J. Zichi, R. Trotta, A. Rastelli, and V. Zwiller, *Appl. Phys. Lett.*, vol. 112, no. 9, p. 093106, Feb. 2018.

[6] C. Santori, D. Fattal, J. Vučković, G. S. Solomon, and Y. Yamamoto, *Nature*, vol. 419, no. 6907, pp. 594–597, Oct. 2002.

[7] H. Wang, Z.-C. Duan, Y.-H. Li, S. Chen, J.-P. Li, Y.-M. He, M.-C. Chen, Y. He, X. Ding, C.-Z. Peng, C. Schneider, M. Kamp, S. Höfling, C.-Y. Lu, and J.-W. Pan, *Phys. Rev. Lett.*, vol. 116, no. 21, p. 213601, May 2016.

[8] N. Akopian, N. H. Lindner, E. Poem, Y. Berlatzky, J. Avron, D. Gershoni, B. D. Gerardot, and P. M. Petroff, *Phys. Rev. Lett.*, vol. 96, no. 13, p. 130501, Apr. 2006.

[9] C. L. Salter, R. M. Stevenson, I. Farrer, C. A. Nicoll, D. A. Ritchie, and A. J. Shields, *Nature*, vol. 465, no. 7298, pp. 594–597, 2010.

[10] D. Huber, M. Reindl, Y. Huo, H. Huang, J. S. Wildmann, O. G. Schmidt, A. Rastelli, and R. Trotta, *Nat. Commun.*, vol. 8, p. 15506, May 2017.

[11] M. A. M. Versteegh, M. E. Reimer, A. A. van den Berg, G. Juska, V. Dimastrodonato, A. Gocalinska, E. Pelucchi, and V. Zwiller, *Phys. Rev. A*, vol. 92, no. 3, p. 033802, Sep. 2015.

[12] A. Boretti, L. Rosa, A. Mackie, and S. Castelletto, *Adv. Opt. Mater.*, vol. 3, no. 8, pp. 1012–1033, Aug. 2015.

[13] Z. Yuan, B. E. Kardynal, R. M. Stevenson, A. J. Shields, C. J. Lobo, K. Cooper, N. S. Beattie, D. A. Ritchie, and M. Pepper, *Science*, vol. 295, no. 5552, pp. 102–5, Jan. 2002.

[14] F. Hargart, C. A. Kessler, T. Schwarzbäck, E. Koroknay, S. Weidenfeld, M. Jetter, and P. Michler, *Appl. Phys. Lett.*, vol. 102, no. 1, p. 011126, Jan. 2013.

[15] J. Zhang, J. S. Wildmann, F. Ding, R. Trotta, Y. Huo, E. Zallo, D. Huber, A. Rastelli, and O. G. Schmidt, *Nat. Commun.*, vol. 6, p. 10067, Dec. 2015.

[16] W. Unrau, D. Quandt, J.-H. Schulze, T. Heindel, T. D. Germann, O. Hitzemann, A. Strittmatter, S. Reitzenstein, U. W. Pohl, and D. Bimberg, *Appl. Phys. Lett.*, vol. 101, no. 21, p. 211119, Nov. 2012.

[17] M. Mehta, D. Reuter, A. Melnikov, A. D. Wieck, S. Michaelis de Vasconcellos, T. Baumgarten, A. Zrenner, and C. Meier, *Phys. E Low-dimensional Syst. Nanostructures*, vol. 42, no. 10, pp. 2749–2752, Sep. 2010.

[18] M. H. Baier, C. Constantin, E. Pelucchi, and E. Kapon, *Appl. Phys. Lett.*, vol. 84,

no. 11, pp. 1967–1969, Mar. 2004.

[19] T. H. Chung, G. Juska, S. T. Moroni, A. Pescaglini, A. Gocalinska, and E. Pelucchi, *Nat. Photonics*, vol. 10, no. 12, pp. 782–787, Oct. 2016.

[20] E. Pelucchi, M. Baier, Y. Ducommun, S. Watanabe, and E. Kapon, *Phys. Status Solidi B-Basic Solid State Phys.*, vol. 238, no. 2, pp. 233–236, 2003.

[21] G. Juska, V. Dimastrodonato, L. O. Mereni, T. H. Chung, A. Gocalinska, E. Pelucchi, B. Van Hattem, M. Ediger, and P. Corfdir, *Phys. Rev. B*, vol. 89, no. 20, p. 205430, May 2014.

[22] L. O. Mereni, V. Dimastrodonato, R. J. Young, and E. Pelucchi, *Appl. Phys. Lett.*, vol. 94, no. 22, p. 223121, Jun. 2009.

[23] J. Zhang, F. Ding, E. Zallo, R. Trotta, B. Höfer, L. Han, S. Kumar, Y. Huo, A. Rastelli, and O. G. Schmidt, *Nano Lett.*, vol. 13, no. 12, pp. 5808–13, Jan. 2013.

[24] D. R. Lovell, T. Yamamoto, M. Inai, T. Takebe, and K. Kobayashi, *Jpn. J. Appl. Phys.*, vol. 31, no. Part 2, No. 7B, pp. L924–L927, Jul. 1992.

[25] G. Juska, E. Murray, V. Dimastrodonato, T. H. Chung, S. T. Moroni, A. Gocalinska, and E. Pelucchi, *J. Appl. Phys.*, vol. 117, no. 13, p. 134302, Apr. 2015.

[26] M. Reischle, G. J. Beirne, R. Roßbach, M. Jetter, and P. Michler, *Phys. Rev. Lett.*, vol. 101, no. 14, p. 146402, Oct. 2008.

[27] K. D. Jöns, P. Atkinson, M. Müller, M. Heldmaier, S. M. Ulrich, O. G. Schmidt, and P. Michler, *Nano Lett.*, vol. 13, no. 1, pp. 126–130, Jan. 2013.

[28] S. Felekyan, R. Kühnemuth, V. Kudryavtsev, C. Sandhagen, W. Becker, and C. A.

M. Seidel, *Rev. Sci. Instrum.*, vol. 76, no. 8, p. 083104, Aug. 2005.

[29] R. J. Young, R. M. Stevenson, A. J. Hudson, C. A. Nicoll, D. A. Ritchie, and A. J. Shields, *Phys. Rev. Lett.*, vol. 102, no. 3, p. 030406, Jan. 2009.

[30] T. B. Pittman, B. C. Jacobs, and J. D. Franson, *Opt. Commun.*, vol. 246, no. 4–6, pp. 545–550, Feb. 2005.

Chapter 6
Statistical study of stacked/coupled site-controlled pyramidal quantum dots and their excitonic properties

Chapter based on the published journal article:

Appl. Phys. Lett., vol. 111, no. 8, p. 083103 (2017)

Stefano T. Moroni, Tung-Hsun Chung, Gediminas Juska, Agnieszka Gocalinska and Emanuele Pelucchi

Tyndall National Institute, "Lee Maltings", University College Cork, Cork, Ireland

Abstract

We report on stacked multiple quantum dots (QDs) formed inside inverted pyramidal recesses, which allow for the precise positioning of the QDs themselves. Specifically we fabricated double QDs with varying inter-dot distance and ensembles with more than two nominally highly symmetric QDs. For each, the effect of the interaction between QDs is studied by characterizing a large number of QDs through photoluminescence spectroscopy. A clear red-shift of the emission energy is observed together with a change in the orientation of its polarization, suggesting an increasing interaction between the QDs. Finally we show how stacked QDs can help influencing the charging of the excitonic complexes.

In the last decade semiconductor quantum dots (QDs) have been having a key role in the field of quantum optics and quantum information. Many challenges have been overcome over the years as semiconductor QDs have been proven to emit on-demand single, identical and entangled photons upon optical and electrical excitation [1][2][3][4][5]. Moreover, the atomic-like nature of the excitonic transitions in semiconductor QDs allowed performing fundamental studies on the complexes forming in a single-QD as such (e.g. [6][7][8]) and opened the way for a wider number of possible technological alternatives in the quest for quantum information processing.

One of the unique features of semiconductor QDs is the possibility to fabricate two QDs at a small distance in order to obtain a coupled QD system. Several studies were carried out on this kind of systems where the coupling of the electronic levels was obtained with different approaches, e.g. by lateral coupling [9] or the application of an electric field in order to match the electronic conduction level of the excitons and prepare a molecular-like state delocalized over two QDs [10][11][12]. Nevertheless, most of the approaches to obtain coupled semiconductor QD systems are based on the vertical correlation of Stranski-Krastanov (SK) self-assembled QDs [10][13][14][15]. This methodology is, in general, intrinsically limited by a strong dot to dot "during growth" influence, delivering uneven dots and a broad statistical distribution of properties. Here, instead, we employ a different strategy to form stacked QDs, i.e. based on highly symmetric pyramidal site-controlled QDs [16]. Specifically, we took advantage of the uniformity and of the accurate control over the position of our pyramidal QD system to precisely stack two or more highly symmetric QDs on the top of each other. Remarkably, stacked coupling in technologically relevant site-controlled systems has been rarely addressed in the literature, with references [17] and [18] being the only cases known to us, both actually relying on "short" wire-like structures as QD systems as opposed to effectively self-assembled QDs.

Indeed, Pyramidal QDs are fabricated by performing MetalOrganic Vapour-Phase Epitaxy (MOVPE) over a GaAs substrate lithographically pre-patterned into an ordered array of pyramidal recesses. Inside each of the pyramids, an InGaAs QD layer is deposited between GaAs inner barriers and AlGaAs outer barriers. This QD family intrinsically delivers site-control and has been highlighted recently for its scalability potentiality when quantum technological approaches are to be considered. Actually, thanks to its intrinsic symmetry, this system has recently been proven to emit entangled photon pairs by means of both optical and electrical excitation [19][20]. In this work we filled the above-mentioned knowledge gap, we took advantage of a high level of control and reproducibility and addressed scalability issues by exploring the effects on QD formation and excitonic properties of various stacking recipes. This was done by collecting a large statistics on multiple-QD pyramids, characterizing InGaAs double-QD systems at different inter-dot barrier and higher number-QD pyramids, and strategically demonstrating a high level of control and tunability: an important characteristic for future exploitation as tailored quantum light sources [21].

We prepared a batch of four samples of pyramidal quantum dots composed of two stacked InGaAs QDs with the same nominal thickness (0.5 nm) and varying inter-dot GaAs barrier. The samples were grown on the same pre-patterned substrate to avoid any effect related to eventual small differences in the dimensions of the pyramidal recesses arising in separate substrates processing runs. All the samples were grown by MOVPE at 20mbar at a nominal temperature of 730 °C on a substrate patterned with 7.5µm pitch pyramidal recesses with growth conditions mimicking those reported elsewhere [22][23]. The different inter-dot barrier sizes were chosen to be 10 nm, 2 nm, 1 nm and 0.5 nm. The samples then underwent a conventional backetching procedure, consisting in the removal of the original substrate in order to turn the pyramids upside-down and reveal their tips [22][23]. All the samples were characterized by micro-photoluminescence spectroscopy at cryogenic temperature (~8 K).

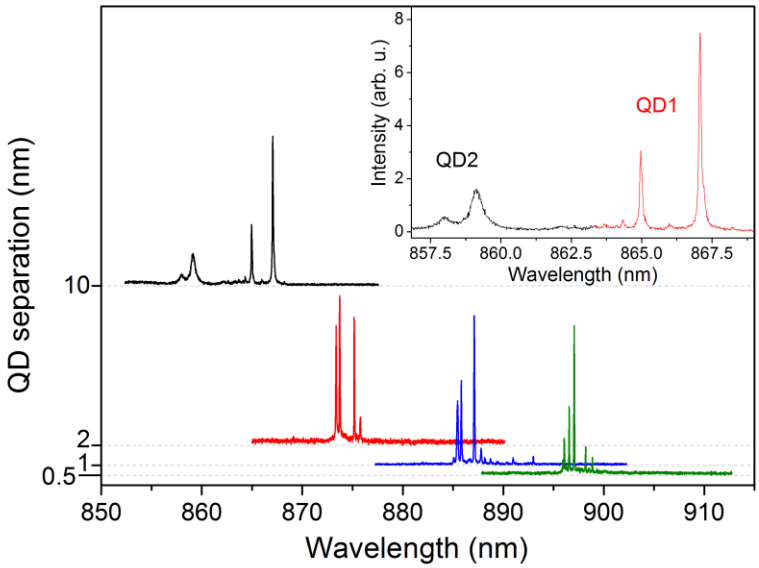


Fig.1: Representative QD spectrum for each of the samples with double dots grown with the same nominal thickness (0.5 nm for each of the two QD) and varying barrier between the QD (y axis). The red shift of the emission wavelength is evident as the separation between the dots is decreased; the insert shows a close-up on the spectrum for the 10 nm-barrier case where the emission of each independent QD is highlighted.

Before starting our discussion, it should be highlighted that, although the QDs are nominally identical in thickness, the PL spectrum of each of them can be slightly different in emission energies and varies around a given mean value: this is due to unavoidable monolayer fluctuations in the thicknesses of the individual QDs as well as of the inter-dot barrier arising during the growth. Moreover, the second QD layer is deposited on the top of a surface profile that is slightly different from the GaAs profile on which the first QD is grown; therefore there may be minor differences in the shape of the two QDs as well [24][25].

A representative QD spectrum for each sample is reported in Fig.1. At first glance it is possible to see how the emission wavelength is red-shifting as the separation between the dots is reduced. A more detailed look at the spectra reveals that in the case of 10 nm spacing (Fig.1) typically it was always possible to distinguish two

separate groups of emission peaks slightly (a few meV) shifted from each other, showing a similar pattern. Based on the comparison with previous data regarding single-dots [26], we were able to identify this peak pattern as the emission originated by the recombination of a negatively charged exciton and a biexciton for each of the two quantum dots. According to the picture we previously proposed in [26], the exciton recombination is completely hindered by a fast capture of one electron from the negatively charged surroundings, leading instead to what we identify as a negatively charged exciton transition. Interestingly, the 10 nm reference sample also systematically showed that the higher energy group of peaks has a broader linewidth than the more red-shifted one. We'll dedicate a more detailed description of this unexpected phenomenology in the following of our text and we concentrate, at this stage, our discussion on the other dot-separation samples.

Differently from the 10-nm-separation sample, the other three, which had an inter-dot barrier of 2 nm or lower, showed a single-QD-like emission pattern. By polarization-dependence, power dependence and cross-photon-correlation measurements (see supplementary material), for each sample we were able to identify only one transition associated to a single neutral exciton and one relative to a biexciton. A number of other (probably charged) transitions could be observed apart from neutral exciton and biexciton, but at the moment not enough information is available to fully describe their nature. Further studies (e.g. involving the application of an electric field) will help determining the origin and charging of these.

The change in behavior from two-QD-like to single-QD-like, together with the red-shift (a trivially expected behavior of dot coupling, but rarely reported with the here observed scale for SK dots for example; probably because SK processes deliver intrinsically non identical dots [27]) is suggesting that the stacked QDs are behaving like a single "molecular-like" QD rather than two independent single-QDs, even if it should not be considered per se as a full proof of an artificial molecule formation [18].

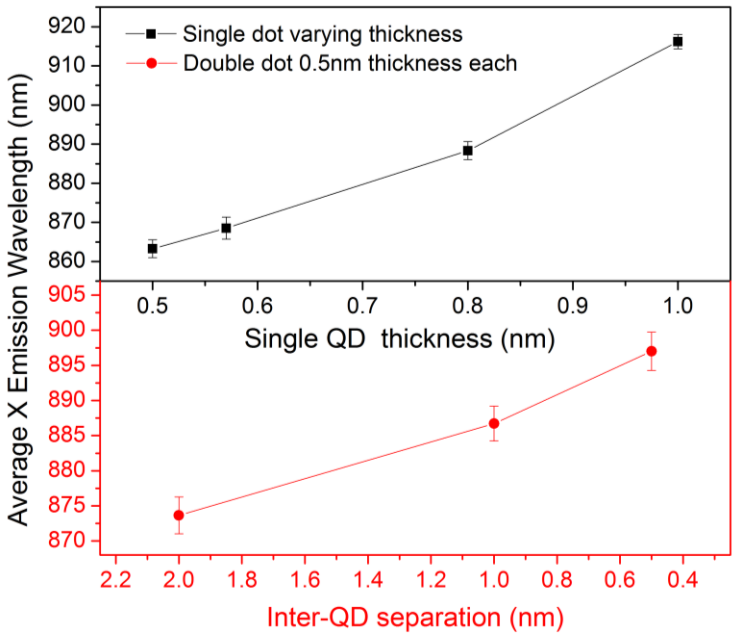


Fig.2: Average emission wavelength as a function of the inter-QD barrier in stacked double 0.5 nm thickness QDs and comparison with the single-QD emission wavelength dependence on the QD thickness. About 20 double-QDs for each sample were considered for the averaging. The error bar shows the sigma of the emission dispersion for the measured dots.

To have a better insight on the effects of the QD stacking, a large statistics was collected for these three samples (about 20 QDs per sample type), taking into account measurements for the emission energy, the binding energy of the biexciton and the fine structure splitting for the exciton levels, known to be relatively small in PQDs. Fig.2 shows the average exciton emission wavelength for double QDs with 0.5 nm thickness and varying barrier thicknesses together with that for a typical single-QD with varying QD thicknesses. The average emission wavelength for the double QD samples is closer to that of a single QD with 0.5 nm thickness when the two QDs are distant (taking into consideration the usual 3-4 meV dispersion of the system [20][23]), and it varies to larger values to become closer to that of a single 1 nm-thick QD as the barrier is reduced. The biexciton binding energy statistics is plotted in Fig.3a. While an anti-binding biexciton with an average binding energy of about -2

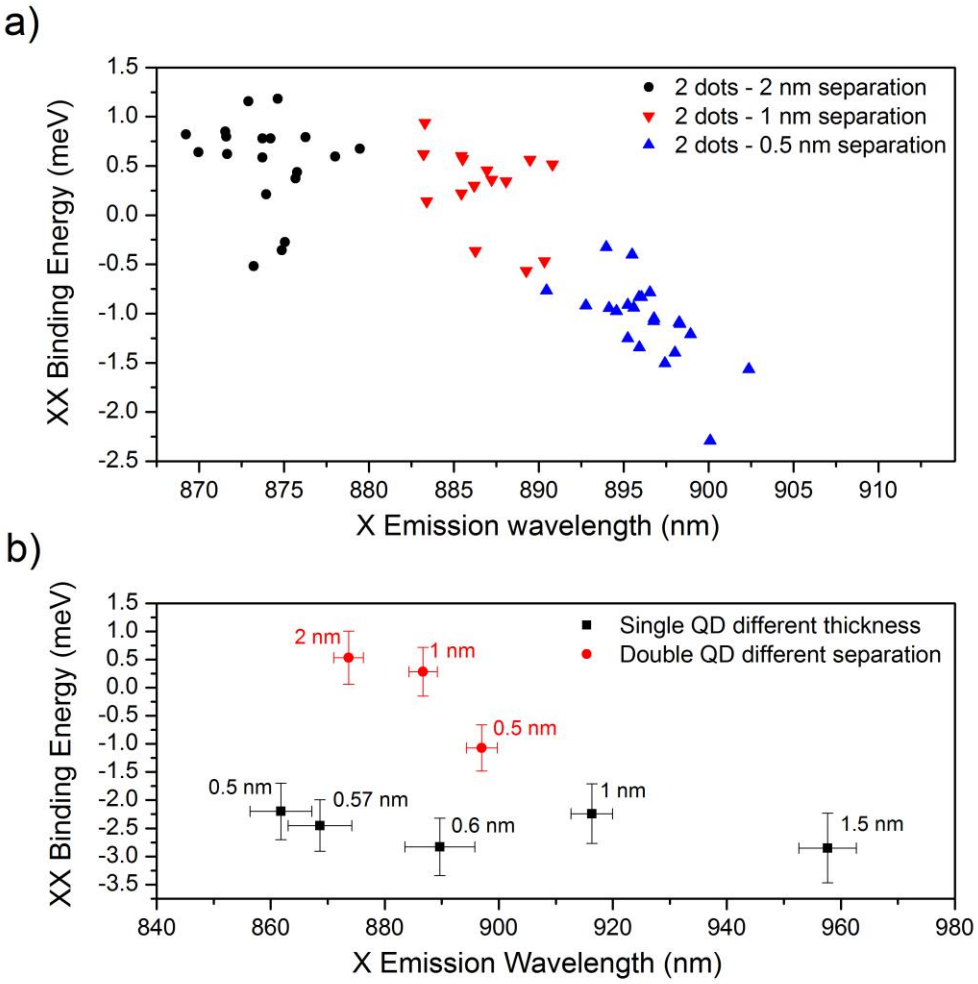


Fig.3: a) Statistics for the biexciton binding energy as a function of the exciton emission wavelength across the different double QD samples; the inset shows the corresponding average emission wavelength for each sample. b) biexciton binding energy vs average exciton emission wavelength for different QD samples; the black squares are relative to single QD samples with different QD thicknesses (specified in the black labels) while the red dots indicate double 0.5 nm thickness QD samples with different separation (specified in the red labels).

meV is the typical case for a single pyramidal QD, for the stacked QDs we see that as the QD barrier is thickened the binding energy decreases and becomes positive (and the biexciton changes to binding). We take this as another sign of the fact that the

two quantum dots are “communicating” and the charges composing the two electron-hole pairs are able to find an energetically favorable configuration (i.e. lower energy) when the QDs are kept at a larger distance rather than when they are very close to each other. It is clear from Fig.3a that a stronger correlation (statistically speaking) seems to have been established between the emission wavelength of the exciton and the binding energy of the biexciton as a function of inter-dot distance: the residual distribution can also be interpreted as an effect of the different influence (coupling) that one dot has on the other depending on (small) fluctuations in the thickness of the inter-dot barrier. Fig.3b is a comparison between the statistics obtained from the stacked-QDs with different barrier thickness (≤ 2 nm) and the regular single-QDs with different nominal thickness [26]: the switch in behaviour of the binding energy (never been observed as such in our single-QDs before) together with the difference in emission energy allows ruling out that the stacked-QDs with 2 nm, 1 nm and 0.5 nm separation could be in reality an elongated single-QD with 3 nm, 2 nm and 1.5 nm thickness respectively.

To improve our insight into the system, two more samples were grown with a different number of QDs: one with three 0.5nm-thick QDs and two 1nm-thick barriers in between and another sample with four 0.5 nm-thick QDs and 1nm-thick inter-QD barriers. A representative spectrum for each of the samples having one to four QDs and the same QD thickness (0.5nm) is presented in Fig.4. In each case a single-QD-like spectrum was measured. For each one it was possible to distinguish unambiguously the emission from the biexciton and exciton recombination cascade. The addition of a QD, again, causes the spectrum to red-shift and alters the binding energy of the biexciton bringing it to positive values. Cross-sectional polarization-dependence measurements ([6][28][29][30]) (i.e. measuring a cleaved facet of the sample, and not from the top) showed, surprisingly to some extent, that the polarization of the emission is oriented in the growth plane in the single-dot case and as the number of QDs is increased the luminescence starts showing a component oriented along the

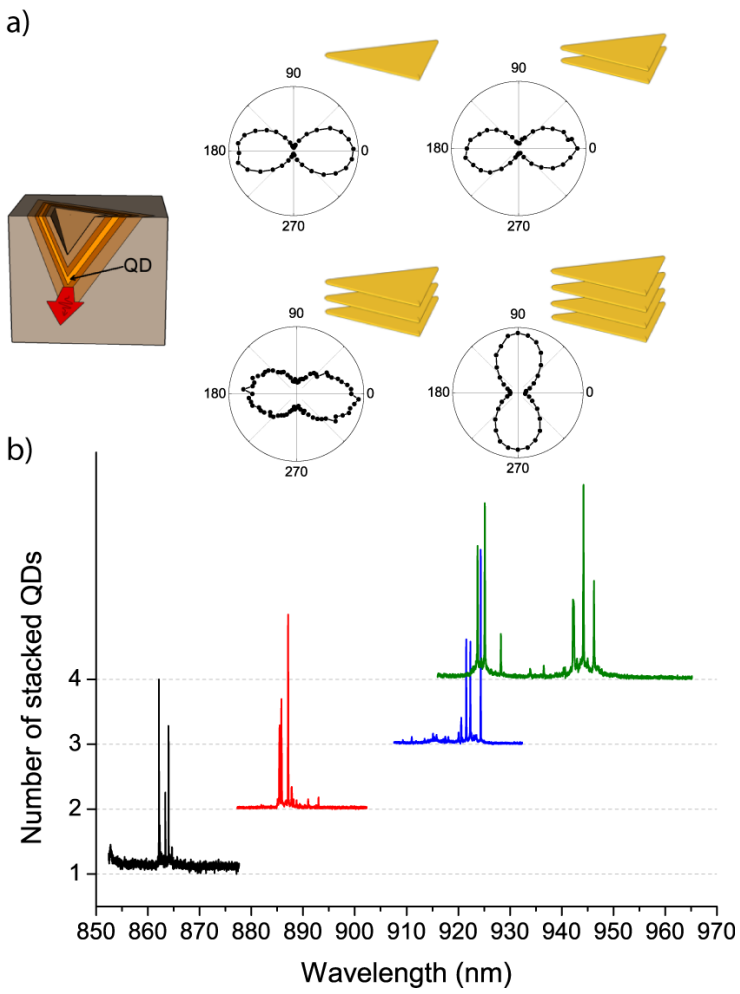


Fig.4: Evolution of the a) cross-sectional polarization dependence and b) typical spectra when the number of stacked QDs is increased; the QDs for these samples had the same nominal thickness of 0.5 nm and the same inter-dot barrier for the adjacent QDs of 1 nm.

growth direction, becoming mainly aligned along the stacked QD axis in the case of four QDs (Fig.4), also a sign of electronic hybridization.

Interestingly, in the sample with four QDs, the increasing interaction between the dots also brings to the appearance of a set of higher energy transitions arising at higher excitation power. Systematic cross-correlations between these transitions and the lower energy ones lead to bunching in a number of cases, indicating that these transitions are related through a recombination cascade (see supplementary

material). Although the pattern in the cascade and the relation between each peak is difficult to interpret and has not been fully understood yet, we might argue that these elements are perhaps hints of an even increasing "molecular" coupling between the QDs in the ensemble, including the possible appearance of "anti-bonding"- like states (which obviously are as today merely a possibility/speculation).

Before ending our letter, we want to finally discuss a different effect which is seen when QDs are stacked with a larger inter-dot barrier of 10 nm, as briefly mentioned earlier. The general behavior of the stacked double QD system in this case is that of two independent QDs, the one at higher energies showing always broader lines than the one at lower energies. To understand the source of this effect, we grew another sample with three QDs of *different thicknesses* and the same nominal inter-QD barrier of 10 nm, as reproduced schematically in Fig.5: the top and bottom QDs had a thickness of 0.45 nm while the central one was 0.6 nm thick. This allowed understanding which of the QDs in the ensemble (i.e. which one in growth order) has the best linewidth: as it is shown in the spectrum of Fig.5, the emission from the

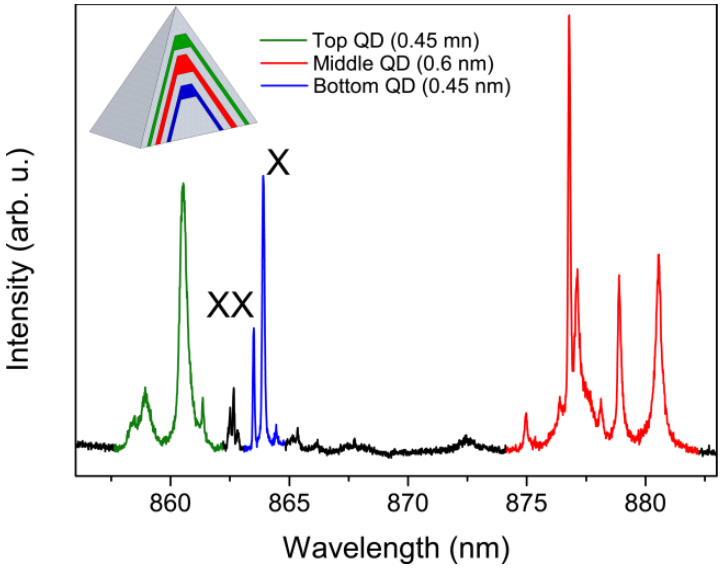


Fig.5: Top: scheme of the triple-QD sample with 10 nm inter-dot barrier and varying QD thickness; Bottom: typical spectrum for the same sample; the emission from each of the QDs in the ensemble is marked with the corresponding color.

central dot can be easily distinguished as it is the lowest energy feature, while it can be a little more tricky to understand which of the other two dots the remaining emission belongs to.

It is well known that during the MOVPE growth of InGaAs on GaAs the lateral profile of the pyramidal recess tends to become larger [31]. Therefore we can speculate that the third grown QD (the bottom one, after the backetching process) will have a larger lateral profile, and, being grown at the same nominal thickness as the top one, it will actually result in being thicker. We conclude that most probably the top QD (i.e. the last grown one), which is closer to the surface after the backetching, is the one with broader lines (on a larger statistics of measured QD spectra, it shows an average value of 800± 400 μeV) while the bottom one shows the best linewidth (110± 30 μeV), the middle one having an intermediate broadening of the emission peaks (400±190 μeV). While the source of this systematic effect is not clear, we speculate that it could be related to the influence of the sample surface (which in all the samples presented here is only about 100nm away from the top dot) on the charge feeding of the QD. This is in agreement to the general trend observed in single (pyramidal) QDs where the presence of a negatively charged exciton leads to broader lines.

In conclusion, we investigated the effect that the stacking and interaction of two or more pyramidal highly symmetric quantum dots have on their optical properties. A consistent red-shift of the emission in identical stacked QDs and a change in the biexciton behavior were observed and interpreted as a sign of coupling between the QDs; this hypothesis was also validated by the evidence of a change in the polarization direction of the photoluminescence emission in higher-number stacked-QDs. Finally, we showed that the inclusion of an extra QD at a larger inter-dot separation from the first one can allow to systematically obtaining a better linewidth in above-bandgap excitation schemes. Our study also shows that the stacking of QDs can be an additional “tuning knob” to control the emission energy, biexciton binding

energy, polarization and linewidth of our pyramidal QDs. Finally, more analysis will be carried out to prove and understand the nature of the coupling between the QDs and to confirm the appearance of anti-bonding states for multiple QWD coupling.

Supplementary material

Example of determination of exciton and biexciton in samples with 2 stacked QDs

For each sample of stacked QDs with different inter-dot barrier, we performed polarization-dependence, power dependence and cross-photon-correlation measurements. The combination of these measurements allows identifying exciton and biexciton transitions in a QD sample with a good degree of confidence. We report as a reference an example of a stacked-QD pair with 2 nm inter-dot barrier. As it can be seen in Fig.6 b) the power dependence presents a super-linear dependence of the intensity of the biexciton on the excitation power, while in the case of exciton it is sub-linear; in Fig.6 c) the polarization dependence of the exciton-biexciton energy difference can be used to calculate the fine structure splitting (FSS), which is a characteristic of an exciton non-degenerate level and allows distinguishing exciton and biexciton from a charged complex; finally, cross-correlation between these two transitions (Fig.6 d)) showed a strong bunching, suggesting that they are bound by a direct recombination cascade.

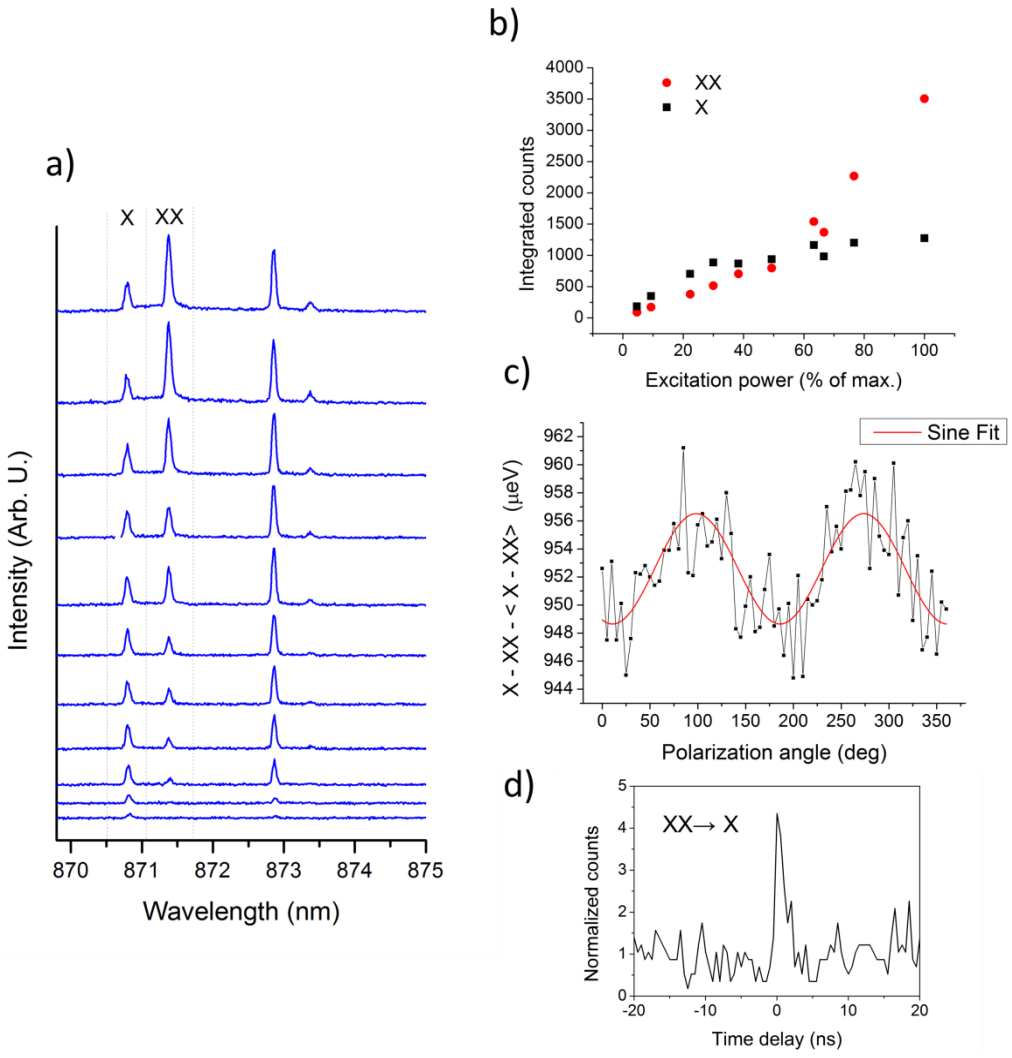


Fig.6: a) evolution of the spectrum of 2 stacked QDs with an inter-dot barrier of 2 nm as the excitation power is increased; the peaks identified with exciton and biexciton transitions are indicated; b) power dependence of exciton and biexciton showing sub-linear evolution of the exciton and super-linear evolution of the biexciton; c) polarization dependence of the difference in energy between exciton and biexciton, presenting typical fine-structure-splitting; d) cross-correlation measurement between biexciton and exciton; the strong bunching is typical of a direct cascade.

These three measurements were performed for each QD. If all of the three measurements resulted in the expected behavior for exciton and biexciton, the QD

was included in the statistics for emission energy and binding energy, otherwise it was discarded.

Characterization of 4 stacked QDs samples through cross-correlation

We report the results of cross-correlation measurements in a single 4 stacked QDs ensemble as a representative case. The typical spectrum for this sample is reported in Fig.7, where each main transition is labeled with a number for clarity. First it is important to remark that the 3 main transitions at higher energy appear at higher excitation power. It wasn't possible to clearly identify any couple of transition showing all the characteristics of an exciton-biexciton pair as for the 2-QDs samples. Nonetheless we tried to establish the relationship between the transitions in terms of recombination order and dynamical evolution. From Fig.8, where we reported all the possible cross-correlations between the high-energy and the low-energy transitions, it can be seen that each of the high-energy transitions exhibits bunching with a low-energy transition. Specifically we identify a cascade between 4 and 3, 5 and 2, 6 and 3. As it is obviously not possible that both transition 4 and 6 directly recombine to the

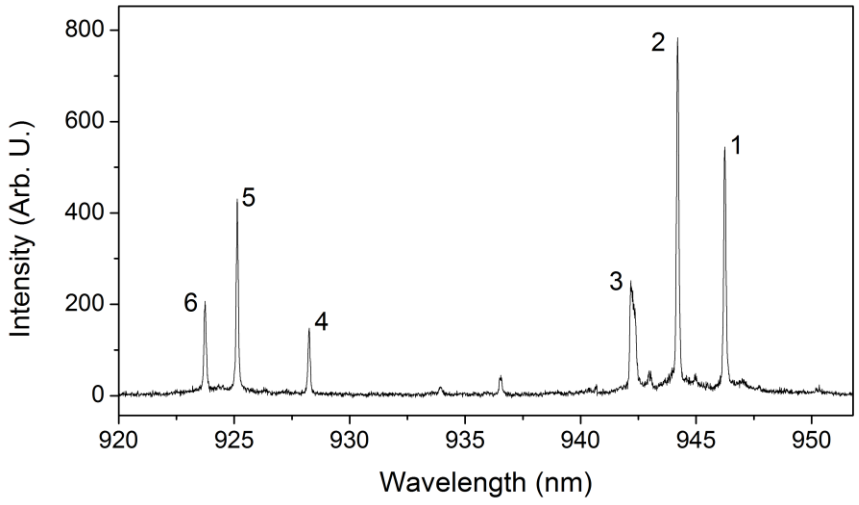


Fig.7: Typical spectrum for a 4-stacked-QD ensemble; transitions are labelled in order to allow easy referencing in the text.

same level, it must be that either one of the two cases is an indirect transition, or a somehow more complex phenomenology (unclear at this stage).

The bunching between the two different groups, though, is clearly demonstrating that these come from the same QD-ensemble structure. Given the high energy gap of these two groups of transitions and that the higher energy ones are appearing only at higher excitation powers, we propose/speculate these might be related to an equivalent of “antibonding” states in a QD molecule like structure.

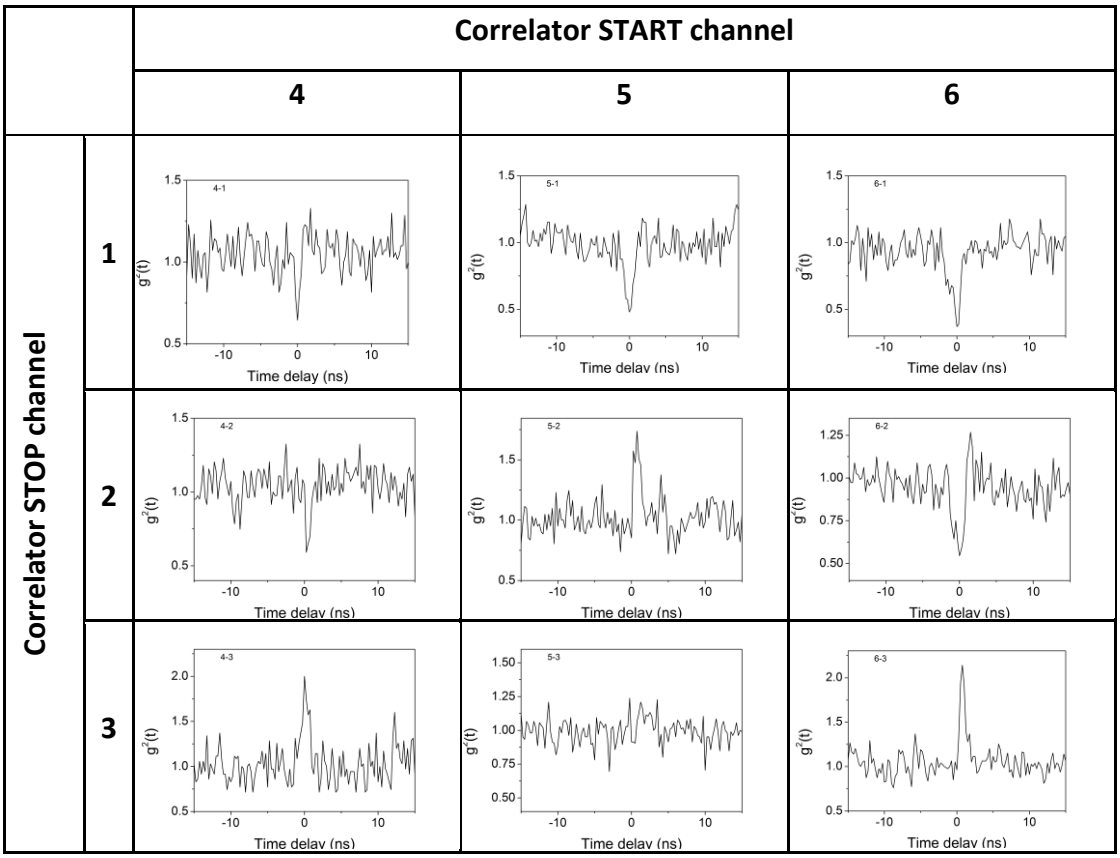


Fig.8: Photon cross-correlation results for each possible combination where one of the high energy transitions is triggering the start of the correlator and one of the lower energy transitions is triggering the stop; columns are labeled with the starting transition, rows with the one that stops.

References

[1] P. Michler, A. Kiraz, C. Becher, W. V Schoenfeld, P. M. Petroff, L. Zhang, E. Hu, and A. Imamoglu, *Science*, vol. 290, no. 5500, pp. 2282–5, Dec. 2000.

[2] C. Santori, D. Fattal, J. Vučković, G. S. Solomon, and Y. Yamamoto, *Nature*, vol. 419, no. 6907, pp. 594–597, Oct. 2002.

[3] N. Akopian, N. H. Lindner, E. Poem, Y. Berlatzky, J. Avron, D. Gershoni, B. D. Gerardot, and P. M. Petroff, *Phys. Rev. Lett.*, vol. 96, no. 13, p. 130501, Apr. 2006.

[4] Z. Yuan, B. E. Kardynal, R. M. Stevenson, A. J. Shields, C. J. Lobo, K. Cooper, N. S. Beattie, D. A. Ritchie, and M. Pepper, *Science*, vol. 295, no. 5552, pp. 102–5, Jan. 2002.

[5] C. L. Salter, R. M. Stevenson, I. Farrer, C. A. Nicoll, D. A. Ritchie, and A. J. Shields, *Nature*, vol. 465, no. 7298, pp. 594–597, 2010.

[6] Y. H. Huo, B. J. Witek, S. Kumar, J. R. Cardenas, J. X. Zhang, N. Akopian, R. Singh, E. Zallo, R. Grifone, D. Kriegner, R. Trotta, F. Ding, J. Stangl, V. Zwiller, G. Bester, A. Rastelli, and O. G. Schmidt, *Nat Phys*, vol. 10, no. 1, pp. 46–51, Jan. 2014.

[7] V. Jovanov, S. Kapfinger, M. Bichler, G. Abstreiter, and J. J. Finley, *Phys. Rev. B*, vol. 84, no. 23, p. 235321, Dec. 2011.

[8] T. Warming, E. Siebert, A. Schliwa, E. Stock, R. Zimmermann, and D. Bimberg, *Phys. Rev. B*, vol. 79, no. 12, p. 125316, Mar. 2009.

[9] G. J. Beirne, C. Hermannstädter, L. Wang, A. Rastelli, O. G. Schmidt, and P. Michler, *Phys. Rev. Lett.*, vol. 96, no. 13, p. 137401, Apr. 2006.

[10] H. J. Krenner, M. Sabathil, E. C. Clark, A. Kress, D. Schuh, M. Bichler, G. Abstreiter, and J. J. Finley, *Phys. Rev. Lett.*, vol. 94, no. 5, p. 057402, Feb. 2005.

[11] G. Ortner, M. Bayer, Y. Lyanda-Geller, T. L. Reinecke, A. Kress, J. P. Reithmaier, and A.

Forchel, *Phys. Rev. Lett.*, vol. 94, no. 15, p. 157401, Apr. 2005.

[12] E. A. Stinaff, M. Scheibner, A. S. Bracker, I. V Ponomarev, V. L. Korenev, M. E. Ware, M. F. Doty, T. L. Reinecke, and D. Gammon, *Science*, vol. 311, no. 5761, pp. 636–9, Feb. 2006.

[13] Q. Xie, A. Madhukar, P. Chen, and N. P. Kobayashi, *Phys. Rev. Lett.*, vol. 75, no. 13, pp. 2542–2545, Sep. 1995.

[14] G. Ortner, M. Schwab, P. Borri, W. Langbein, U. Woggon, M. Bayer, S. Fafard, Z. Wasilewski, P. Hawrylak, Y. B. Lyanda-Geller, T. L. Reinecke, and A. Forchel, *Phys. E Low-dimensional Syst. Nanostructures*, vol. 25, no. 2–3, pp. 249–260, Nov. 2004.

[15] A. J. Bennett, M. A. Pooley, R. M. Stevenson, M. B. Ward, R. B. Patel, A. B. de la Giroday, N. Sköld, I. Farrer, C. A. Nicoll, D. A. Ritchie, and A. J. Shields, *Nat. Phys.*, vol. 6, no. 12, pp. 947–950, Dec. 2010.

[16] M. A. Dupertuis, K. F. Karlsson, D. Y. Oberli, E. Pelucchi, A. Rudra, P. O. Holtz, and E. Kapon, *Phys. Rev. Lett.*, vol. 107, no. 12, p. 127403, Sep. 2011.

[17] M. Khoshnegar, T. Huber, A. Predojević, D. Dalacu, M. Prilmüller, J. Lapointe, X. Wu, P. Tamarat, B. Lounis, P. Poole, G. Weihs, and H. Majedi, p. 34, Oct. 2015.

[18] Q. Zhu, K. F. Karlsson, M. Byszewski, A. Rudra, E. Pelucchi, Z. He, and E. Kapon, *Small*, vol. 5, no. 3, pp. 329–335, Feb. 2009.

[19] G. Juska, V. Dimastrodonato, L. O. Mereni, A. Gocalinska, and E. Pelucchi, *Nat. Photonics*, vol. 7, no. 7, pp. 527–531, May 2013.

[20] T. H. Chung, G. Juska, S. T. Moroni, A. Pescaglini, A. Gocalinska, and E. Pelucchi, *Nat. Photonics*, vol. 10, no. 12, pp. 782–787, Oct. 2016.

[21] S. E. Economou, N. Lindner, and T. Rudolph, *Phys. Rev. Lett.*, vol. 105, no. 9, p. 093601, Aug. 2010.

[22] M. H. Baier, E. Pelucchi, E. Kapon, S. Varoutsis, M. Gallart, I. Robert-Philip, and I. Abram, *Appl. Phys. Lett.*, vol. 84, no. 5, pp. 648–650, Feb. 2004.

[23] L. O. Mereni, V. Dimastrodonato, R. J. Young, and E. Pelucchi, *Appl. Phys. Lett.*, vol. 94, no. 22, p. 223121, Jun. 2009.

[24] V. Dimastrodonato, E. Pelucchi, and D. D. Vvedensky, *Phys. Rev. Lett.*, vol. 108, no. 25, p. 256102, Jun. 2012.

[25] S. T. Moroni, V. Dimastrodonato, T.-H. Chung, G. Juska, A. Gocalinska, D. D. Vvedensky, and E. Pelucchi, *J. Appl. Phys.*, vol. 117, no. 16, p. 164313, Apr. 2015.

[26] G. Juska, E. Murray, V. Dimastrodonato, T. H. Chung, S. T. Moroni, A. Gocalinska, and E. Pelucchi, *J. Appl. Phys.*, vol. 117, no. 13, p. 134302, Apr. 2015.

[27] G. Bester, J. Shumway, and A. Zunger, *Phys. Rev. Lett.*, vol. 93, no. 4, p. 047401, Jul. 2004.

[28] G. Juska, V. Dimastrodonato, L. O. Mereni, T. H. Chung, A. Gocalinska, E. Pelucchi, B. Van Hattem, M. Ediger, and P. Corfdir, *Phys. Rev. B*, vol. 89, no. 20, p. 205430, May 2014.

[29] K. F. Karlsson, V. Troncale, D. Y. Oberli, A. Malko, E. Pelucchi, A. Rudra, and E. Kapon, *Appl. Phys. Lett.*, vol. 89, no. 25, p. 251113, Dec. 2006.

[30] R. M. Stevenson, R. J. Young, P. See, C. E. Norman, A. J. Shields, P. Atkinson, and D. A. Ritchie, *Appl. Phys. Lett.*, vol. 87, no. 13, p. 133120, Sep. 2005.

[31] E. Pelucchi, V. Dimastrodonato, A. Rudra, K. Leifer, E. Kapon, L. Bethke, P. A. Zestanakis, and D. D. Vvedensky, *Phys. Rev. B*, vol. 83, no. 20, p. 205409, May 2011.

Chapter 7
Vanishing biexciton binding energy from stacked, MOVPE grown, site-controlled pyramidal quantum dots for twin photon generation

Chapter based on the published journal article:

J. Cryst. Growth, vol. 506, pp. 36–39, (2019)

S. T. Moroni, S. Varo, G. Juska, T. H. Chung, A. Gocalinska, E. Pelucchi

Tyndall National Institute, "Lee Maltings", University College Cork, Cork, Ireland

Abstract

We characterized stacked double-pyramidal quantum dots which showed biexciton binding energies close to zero by means of photoluminescence and cross-correlation measurements. It was possible to obtain a sequence of two photons with (nearly) the same energy from the biexciton-exciton-ground state cascade, as corroborated by a basic rate-equation model. This type of two-photon emission is both of relevance for fundamental quantum information theory studies as well as for more exotic applicative fields such as quantum biology.

7.1. Introduction

Semiconductor quantum dot (QD)-based light sources are capable of delivering quantum light of various nature and are intensively studied for both fundamental and technological purposes. For instance, state of the art single QDs are being developed pursuing pure single photon emission [1][2][3], generation of highly indistinguishable photons[4][5], production of entangled photon pairs with high fidelity[6][7][8], and also exploitation of time-bin entanglement ([9] and references therein). All these are relevant for applications in quantum information and computation implementations based on photonics [10][11], or with a strong photonics presence. Among the spectrum of conceivable non-classical light, “twin” photons (i.e. identical photons pairs, with the same energy) represent an interesting possibility. Applications have been proposed in the field of quantum information itself as well as in other more “exotic” areas, such as quantum biology [12].

It is well known that this type of two-photon state can be generated by means of spontaneous parametric down conversion, relying on probabilistic emission rather than on a truly quantum mechanical “on-demand” scheme. Moreover, only a few cases are reported in the literature, where twin photon generation was achieved on an “integrated” platform. It is in fact possible to produce twin photons from a semiconductor parametric-down-conversion-based integrated system [13], although with strong compromises on efficiency. More recently, III-V semiconductor QDs were employed to this purpose, where the two photons generated through the biexciton-exciton-ground state cascade can have the same energy when the biexciton binding energy is zero[14]. As we will show in the following, generation of two photons with the same energy is possible by the excitation of pyramidal quantum dot (PQD) stacked systems by employing alternative epitaxial growth strategies from those already proposed, despite benefitting from remaining in the same III-V family which

has already delivered high quality results when quantum-light is to be considered ([1][6][8]).

Engineering the surface of a growth substrate for the fabrication of QDs can be extremely beneficial to develop technological alternatives and to advance quantum optics/technologies. For instance, although state of the art self-assembled QDs were widely employed to reach milestones in this field (as per the above mentioned references), control over the position together with the overall structural properties of the emitters can only be achieved using selective-area growth and/or other pre-patterning strategies. All, not necessarily in the same material system obviously (see e.g. [15][16][17] which could also potentially obtain similar results), including exploring dots in nanowires for example (e.g. [18][19]), i.e. a rather different approach from conventional self assembled dots. In this context the PQD system is an outstanding example of how metalorganic vapour-phase epitaxy (MOVPE) can be

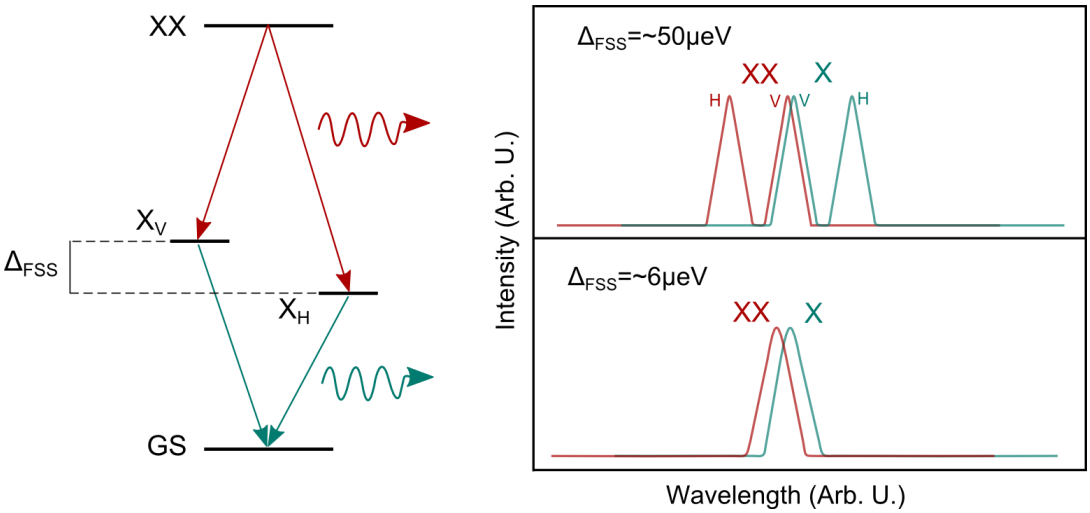


Fig.1: On the left: general schematic representation of Fine-Structure-Splitting (FSS) in the biexciton-exciton-ground state of a QD; on the right: schematic representation of the spectra of biexciton (red) and exciton (green) transitions for QDs with relatively small biexciton binding energy and significant FSS (top) as in [14], and for QDs with vanishing biexciton binding energy and small FSS (bottom) as in our stacked PQDs.

employed to reach high control over the structural and optical properties of QDs, and how this has been indeed possible thanks to deep understanding of the growth processes [20][21]. PQDs have been proved to allow high density of entangled photon emitters by both optical [22] and electrical excitation [23]. But one of the unique capabilities offered by the PQD system is that of systematically stacking two or more QDs on the top of each other, maintaining near identical structures, and allowing for the tuning of their optical properties, among which the biexciton binding energy, as we have recently showed [24].

Compared to the only other case of QD-based twin photon generation we are aware of presented in the literature [14], PQDs present two advantages: the first is technological, as PQDs allow for precise positioning of the source, an important requirement for practical implementations. The second bears a more fundamental aspect. In fact, in ref.[14] the authors exploited the natural asymmetry of their QD system, delivering a split in the exciton and biexciton states (normally referred to as fine structure splitting, see Fig 1 where Ref. [14] and our approach are compared) to cancel out the relative binding energies. Therefore they selected only one polarization, filtering 50% of the events of photon generation. This is not (at least ideally) the case we're presenting, where all the photons are potentially contributing.

7.2. Experimental

PQDs are fabricated starting from a patterned (111)B-oriented GaAs substrate (in which tetragonal recesses are obtained), on which MOVPE is performed depositing InGaAs dots with GaAs barriers, as for example discussed in ref [25] and [26]. The growth process is the interesting result of the competition between precursors decomposition rate anisotropies, and adatom diffusion and preferential attachment at concave recesses (also referred to in the literature as capillarity processes) [27][28]. More details on the fabrication procedure of the stacked system can also be

found in ref. [24]. Samples also undergo a “back-etching” process to turn the pyramids pointing up by removing the original growth substrate, allowing an enhanced light extraction. The optical characterization of the samples presented in this paper was performed by photoluminescence and photon correlation spectroscopy using a standard HBT setup. All measurements were performed at 10K in a non-resonant excitation scheme, as described elsewhere [22].

7.3. Results and discussion

We previously reported on the effect of stacking PQDs in the same pyramidal structure [24]: as the distance between nominally identical QDs (i.e. with the same thickness) was reduced, a previously unreported regime was entered of only single dot “like” emission. Also a red-shift of the emission was systematically reported as a function of reducing inter-dot layer thickness, together with an overall change in the binding energy of the biexciton (normally, and here, defined as the energy difference between exciton and biexciton transitions). For instance it was possible to gradually go from samples with anti-bonding biexciton (binding energy<0) to samples with bonding biexciton (binding energy>0) by simply varying the distance between the dots. We pause here a second, to stress the relevance and unique control demonstrated by these results. Indeed the peculiarity of the MOVPE III-V growth process utilized here [20][29] allows what is a uniquely demonstrated control over uniformity and dot reproducibility [30], which should be ascribed to the distinctive MOVPE processes involved in a concave environment (i.e. decomposition rate anisotropy and specific adatom diffusion/capillarity processes/anisotropies).

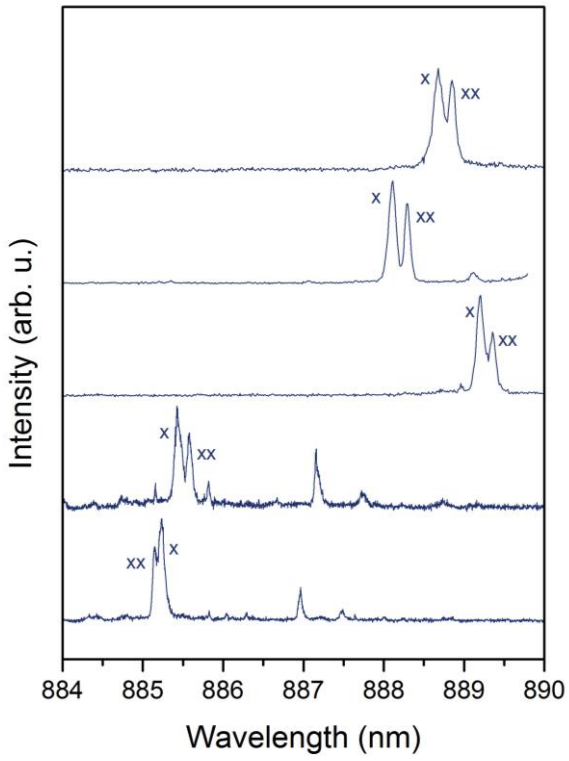


Fig.2: A collection of spectra from the same sample with 2 QDs with 1nm inter-dot barrier showing little or vanishing biexciton binding energy. Exciton and biexciton are marked with the labels “X” and “XX” respectively in each spectrum.

The sample with inter-dot barrier of 1 nm resulted in a distribution of binding energies with an average of 0.2823 ± 0.43254 meV, interestingly allowing to easily find quantum dots with nearly zero biexciton binding energy by “scanning” the QD ensemble/sample.

We concentrated our characterization on the QDs with nearly-zero biexciton binding energy from the 1 nm inter-dot barrier sample. Although a complete overlap between exciton and biexciton transitions was statistically hard to find (and eventually even harder to recognize as two superimposed transitions by simply observing the spectrum), it was possible to find PQDs where significant overlap between the two excitonic transitions could be observed. We note also that, on single PQDs, a similar zero binding energy was also reported in the past, but no

experimental optical correlation verification actually performed [31]. Also it should be said that spectral wandering resulted in average linewidths of exciton and biexciton of respectively 172μeV and 119μeV. Fig.2 shows a collection of spectra from this sample where the biexciton binding energy was small and exciton and biexciton were showing a significant spectral overlap. We stress that it is easy to locate quantum dots showing this characteristics on the sample under analysis. Moreover, we need to specify at this point that the large overlap between the exciton and biexciton spectra is also due to the relatively large linewidths of the peaks. The origin of the spectral wandering is to be found in the non-resonant excitation technique employed, causing therefore the small FSS to be hidden. In case of resonant or quasi-resonant excitation of the QD we would expect the linewidth to sensibly decrease and partially reduce the overlap between the transitions, also revealing the small FSS. We note that this can/could be corrected in a second step by employing tuning strategies, such as the application of piezoelectric stress [32].

We consider here as representative/significant example the spectrum of a QD presented in Fig.3a: in this case it was possible to spectrally separate photons from each transition with our spectrometer while still having a significant overlap between the exciton and biexciton (which were identified using power dependence and cross-correlation, following criterions described in [24]). Fig.3b shows the cross-correlation experiment between biexciton and exciton, performed by selecting the “outer” part of each peak with respect to the overlap, having set-up a resolution of our spectrometer of about 0.2nm. This resulted in a typical bunching, with a $g^2(t)$ up to 6, also demonstrating the biexciton-exciton cascade.

We also performed autocorrelations energetically filtering only photons relative to the spectral overlap of the two transitions; Fig.3c shows the autocorrelation measurement for the selected QD. A symmetric $g^2(t)$ was collected, showing a pronounced bunching at zero delay time and a slight anti-bunching at a few nanoseconds delay. We recognize this as a signature of the emission of two

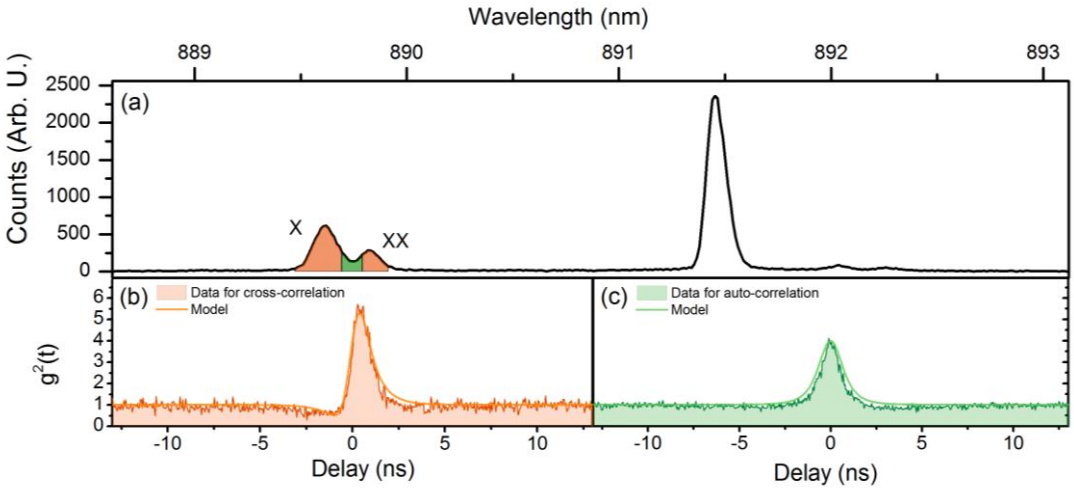


Fig.3: a) A representative spectrum for a typical PQD with 2 QDs at 1nm inter-dot barrier; exciton and biexciton are labeled with X and XX respectively (while the brighter peak at longer wavelengths is relative to a negatively charged exciton[25]) Auto-correlation for the photons in the spectral overlap between the two excitonic transitions (schematically highlighted with the green color in a)) showing a significant bunching and a symmetric shape, as found in similar cases in literature for twin photons [14]. c) Cross-correlation between biexciton (start channel of the correlator) and exciton (stop channel), highlighted with the same color in a), showing strong bunching, confirming the cascade between the two transitions.

subsequent photons in the selected energy window, as reported previously in the literature [14]. Indeed, the total $g^2(t)$ is given by the sum between the four possible cross-correlation collection events (exciton autocorrelation, biexciton autocorrelation, and the two cross-correlations between exciton and biexciton with reversed order), when either exciton or biexciton are collected at each of the two photodetectors.

We employed a simple rate-equation model to reconstruct the total $g^2(t)$ starting from the measured lifetimes for exciton and biexciton transition: by approximating the system to a 3 level cascade (biexciton-exciton-ground state) for simplicity, we computed each of the $g^2(t)$ functions for exciton autocorrelation, biexciton autocorrelation, exciton and biexciton cross-correlation (in both orders), also taking

into consideration the characteristic response of the measurement apparatus. The only free parameter being the capture rate for an electron-hole pair, we fitted the cross-correlation data and plotted the total $g^2(t)$ autocorrelation for the photons coming from the overlap. Fig.2 shows the fitted data (continuous curve) overlapping the data with good approximation. Although the calculated values for the $g^2(0)$ are in good agreement with the experiment, the full simulated curve slightly deviates from the experiment, suggesting that part of the recombination dynamics (e.g. charged complexes, low-intensity slow lifetimes components) would have to be included in a more complete model. We also note that in order to achieve this fit it was necessary to assume a measured "bad" single-photon emission from both exciton and biexciton, expressed as a "bad" $g^2(0)$ in the corresponding autocorrelations (bad meaning an autocorrelation $g^2(0)$ bigger than 0.5), as typically observed on this sample, probably due to fast re-excitation events.

While in this experiment only part of the photons emitted through the biexciton cascade are falling in the overlapping spectral window, our result act as conceptual proof-of-concept, especially in view of the fact that it should be possible, in the future, to use methods that allow a small tuning of the binding energy, in order to achieve a perfect overlap between the transitions for each of the quantum dots. For example in this contest, the application of a stress to the whole pyramidal structure by means of piezoelectric devices [33].

In conclusion, we showed that MOVPE growth processes combined with patterning of the substrate allow for the seeding and site-control of PQDs with a double-QD structure, presenting single dot like spectra and also allowing the formation of biexcitons with quasi-zero binding energy when proper dot dimensions are carefully chosen/engineered. Photon statistics for the photons coming from the spectral overlap between exciton and biexciton corresponds to that expected for two consecutive photons with the same energy. The reduction of the residual binding energy by means of tuning strategies combined with resonant excitation techniques

would easily allow, for example, to have a larger amount of photons with the same energy, while resonant pumping techniques should also allow for indistinguishable photons [8] and an "ideal" twin-photons generation.

Supplementary material

Rate equation model

We employed a three-level rate equation model to describe the temporal evolution of the excitonic complexes in the PQD. The set of equations can be written as:

$$\frac{d\vec{p}(t)}{dt} = \begin{bmatrix} -1/t_{eh} & 1/\tau_X & 0 \\ 1/t_{eh} & -1/t_{eh} - 1/\tau_X & 1/\tau_{XX} \\ 0 & 1/t_{eh} & -1/\tau_{XX} \end{bmatrix} \begin{pmatrix} p_0(t) \\ p_X(t) \\ p_{XX}(t) \end{pmatrix}$$

where $\vec{p}(t) = (p_0(t),\ p_X(t),\ p_{XX}(t))$ is the time-dependent occupation probability for each level (biexciton (XX), exciton (X) and ground state (0)), t_{eh} is the capture time for one electron-hole pair, $\tau_X$and τ_{XX} are exciton and biexciton lifetimes respectively. Once the initial conditions are set for a transition to happen at time $t = 0$, one can compute the autocorrelation function $g^2(t)$ for that specific transition [34]. For exciton decay we have the initial condition $\vec{p}(0) = (1,0,0)$, for biexciton decay $\vec{p}(0) = (0,1,0)$.Tthe $g_i^2(t)$ for the i-th transition is expressed as $g_i^2(t) = p_i(|t|)/p_i(\infty)$. Cross-correlation is given by $g_{X-XX}^2(t) = p_X(t)/p_X(\infty)$ and $\vec{p}(0) = (0,1,0)$ for $t > 0$, $g_{X-XX}^2(t) = p_{XX}(-t)/p_{XX}(\infty)$ and $\vec{p}(0) = (1,0,0)$ for $t < 0$. The solution for each correlation function is convoluted with the total response function of the detection setup (a Gaussian with 400ps FWHM).

In our simulation τ_X and τ_{XX} were fixed, their values estimated from direct measurement, while t_{eh} was the only free parameter, which was varied to fit the cross-correlation function $g_{X-XX}^2(t)$. Having these parameters, all the possible g^2

functions could be plotted. A linear combination of these resulted in the graph of Fig.3c.

References

[1] P. Michler, A. Kiraz, C. Becher, W. V Schoenfeld, P. M. Petroff, L. Zhang, E. Hu, and A. Imamoglu, *Science*, vol. 290, no. 5500, pp. 2282–5, Dec. 2000.

[2] N. Somaschi, V. Giesz, L. De Santis, J. C. Loredo, M. P. Almeida, G. Hornecker, S. L. Portalupi, T. Grange, C. Antón, J. Demory, C. Gómez, I. Sagnes, N. D. Lanzillotti-Kimura, A. Lemaítre, A. Auffeves, A. G. White, L. Lanco, and P. Senellart, *Nat. Photonics*, vol. 10, no. 5, pp. 340–345, May 2016.

[3] L. Schweickert, K. D. Jöns, K. D. Zeuner, S. F. Covre da Silva, H. Huang, T. Lettner, M. Reindl, J. Zichi, R. Trotta, A. Rastelli, and V. Zwiller, *Appl. Phys. Lett.*, vol. 112, no. 9, p. 093106, Feb. 2018.

[4] C. Santori, D. Fattal, J. Vučković, G. S. Solomon, and Y. Yamamoto, *Nature*, vol. 419, no. 6907, pp. 594–597, Oct. 2002.

[5] H. Wang, Z.-C. Duan, Y.-H. Li, S. Chen, J.-P. Li, Y.-M. He, M.-C. Chen, Y. He, X. Ding, C.-Z. Peng, C. Schneider, M. Kamp, S. Höfling, C.-Y. Lu, and J.-W. Pan, *Phys. Rev. Lett.*, vol. 116, no. 21, p. 213601, May 2016.

[6] N. Akopian, N. H. Lindner, E. Poem, Y. Berlatzky, J. Avron, D. Gershoni, B. D. Gerardot, and P. M. Petroff, *Phys. Rev. Lett.*, vol. 96, no. 13, p. 130501, Apr. 2006.

[7] C. L. Salter, R. M. Stevenson, I. Farrer, C. A. Nicoll, D. A. Ritchie, and A. J. Shields, *Nature*, vol. 465, no. 7298, pp. 594–597, 2010.

[8] D. Huber, M. Reindl, Y. Huo, H. Huang, J. S. Wildmann, O. G. Schmidt, A. Rastelli, and R. Trotta, *Nat. Commun.*, vol. 8, p. 15506, May 2017.

[9] M. A. M. Versteegh, M. E. Reimer, A. A. van den Berg, G. Juska, V. Dimastrodonato, A. Gocalinska, E. Pelucchi, and V. Zwiller, *Phys. Rev. A*, vol. 92, no. 3, p. 033802, Sep. 2015.

[10] P. Kok, W. J. Munro, K. Nemoto, T. C. Ralph, J. P. Dowling, and G. J. Milburn, *Rev. Mod. Phys.*, vol. 79, no. 1, pp. 135–174, Jan. 2007.

[11] I. L. Chuang and D. Gottesman, *Nature*, vol. 402, no. 6760, pp. 390–393, Nov. 1999.

[12] N. Sim, M. F. Cheng, D. Bessarab, C. M. Jones, and L. A. Krivitsky, *Phys. Rev. Lett.*, vol. 109, no. 11, p. 113601, Sep. 2012.

[13] R. Horn, P. Abolghasem, B. J. Bijlani, D. Kang, A. S. Helmy, and G. Weihs, *Phys. Rev. Lett.*, vol. 108, no. 15, p. 153605, Apr. 2012.

[14] T. Heindel, A. Thoma, M. von Helversen, M. Schmidt, A. Schlehahn, M. Gschrey, P. Schnauber, J. H. Schulze, A. Strittmatter, J. Beyer, S. Rodt, A. Carmele, A. Knorr, and S. Reitzenstein, *Nat. Commun.*, vol. 8, p. 14870, Apr. 2017.

[15] A. Winden, M. Mikulics, T. Stoica, M. von der Ahe, G. Mussler, A. Haab, D. Grützmacher, and H. Hardtdegen, *J. Cryst. Growth*, vol. 370, pp. 336–341, May 2013.

[16] A. Winden, M. Mikulics, D. Grützmacher, and H. Hardtdegen, *Nanotechnology*, vol. 24, no. 40, p. 405302, Oct. 2013.

[17] J. Skiba-Szymanska, A. Jamil, I. Farrer, M. B. Ward, C. A. Nicoll, D. J. P. Ellis, J. P. Griffiths, D. Anderson, G. A. C. Jones, D. A. Ritchie, and A. J. Shields, *Nanotechnology*, vol. 22, no. 6, p. 065302, Feb. 2011.

[18] M. E. Reimer, G. Bulgarini, N. Akopian, M. Hocevar, M. B. Bavinck, M. A.

Verheijen, E. P. A. M. Bakkers, L. P. Kouwenhoven, and V. Zwiller, *Nat. Commun.*, vol. 3, no. 1, p. 737, Jan. 2012.

[19] M. Khoshnegar, T. Huber, A. Predojević, D. Dalacu, M. Prilmüller, J. Lapointe, X. Wu, P. Tamarat, B. Lounis, P. Poole, G. Weihs, and H. Majedi, *Nat. Commun.*, vol. 8, p. 15716, Jun. 2017.

[20] E. Pelucchi, V. Dimastrodonato, A. Rudra, K. Leifer, E. Kapon, L. Bethke, P. A. Zestanakis, and D. D. Vvedensky, *Phys. Rev. B*, vol. 83, no. 20, p. 205409, May 2011.

[21] V. Dimastrodonato, E. Pelucchi, P. A. Zestanakis, and D. D. Vvedensky, *Phys. Rev. B*, vol. 87, no. 20, p. 205422, May 2013.

[22] G. Juska, V. Dimastrodonato, L. O. Mereni, A. Gocalinska, and E. Pelucchi, *Nat. Photonics*, vol. 7, no. 7, pp. 527–531, May 2013.

[23] T. H. Chung, G. Juska, S. T. Moroni, A. Pescaglini, A. Gocalinska, and E. Pelucchi, *Nat. Photonics*, vol. 10, no. 12, pp. 782–787, Oct. 2016.

[24] S. T. Moroni, T. H. Chung, G. Juska, A. Gocalinska, and E. Pelucchi, *Appl. Phys. Lett.*, vol. 111, no. 8, p. 083103, Aug. 2017.

[25] G. Juska, E. Murray, V. Dimastrodonato, T. H. Chung, S. T. Moroni, A. Gocalinska, and E. Pelucchi, *J. Appl. Phys.*, vol. 117, no. 13, p. 134302, Apr. 2015.

[26] G. Juska, V. Dimastrodonato, L. O. Mereni, T. H. Chung, A. Gocalinska, E. Pelucchi, B. Van Hattem, M. Ediger, and P. Corfdir, *Phys. Rev. B*, vol. 89, no. 20, p. 205430, May 2014.

[27] V. Dimastrodonato, E. Pelucchi, and D. D. Vvedensky, *Phys. Rev. Lett.*, vol. 108,

no. 25, p. 256102, Jun. 2012.

[28] E. Pelucchi, S. T. Moroni, V. Dimastrodonato, and D. D. Vvedensky, *J. Mater. Sci. Mater. Electron.*, vol. 29, no. 2, pp. 952–967, Jan. 2018.

[29] S. T. Moroni, V. Dimastrodonato, T.-H. Chung, G. Juska, A. Gocalinska, D. D. Vvedensky, and E. Pelucchi, *J. Appl. Phys.*, vol. 117, no. 16, p. 164313, Apr. 2015.

[30] K. Leifer, E. Pelucchi, S. Watanabe, F. Michelini, B. Dwir, and E. Kapon, *Appl. Phys. Lett.*, vol. 91, no. 8, p. 081106, Aug. 2007.

[31] C. Jarlov, P. Gallo, M. Calic, B. Dwir, A. Rudra, and E. Kapon, *Appl. Phys. Lett.*, vol. 101, no. 19, p. 191101, Nov. 2012.

[32] R. Trotta, J. Martín-Sánchez, J. S. Wildmann, G. Piredda, M. Reindl, C. Schimpf, E. Zallo, S. Stroj, J. Edlinger, and A. Rastelli, *Nat. Commun.*, vol. 7, p. 10375, Jan. 2016.

[33] F. Ding, R. Singh, J. D. Plumhof, T. Zander, V. Křápek, Y. H. Chen, M. Benyoucef, V. Zwiller, K. Dörr, G. Bester, A. Rastelli, and O. G. Schmidt, *Phys. Rev. Lett.*, vol. 104, no. 6, p. 067405, Feb. 2010.

[34] D. V Regelman, U. Mizrahi, D. Gershoni, E. Ehrenfreund, W. V Schoenfeld, and P. M. Petroff, *Phys. Rev. Lett.*, vol. 87, no. 25, p. 257401, Dec. 2001.

Chapter 8
On the tuning of the optical properties and integration of pyramidal quantum dots

In this chapter some important "partial" results obtained during the course of my PhD research will be presented. On one side the tuning of the optical properties of PQDs was obtained upon application of a piezoelectric strain to a membrane containing the QDs. Secondly, it will be shown how it is possible to manipulate PQDs by means of alternative processing methods.

8.1. Application of piezoelectric stress to PQDs

The tuning of the emission energy of a QD allows to have photons in resonance (or out of resonance) with other QDs, atom transitions for quantum memory, resonant excitation lasers, etc. and is therefore of paramount importance for many applications. Moreover, other properties as well could be tuned by an external field to improve the quality of QD-generated photons, for instance FSS tuning would allow restoring entangled photon emission from asymmetric QDs.

Among the several methods which can be employed to tune the optical properties of a QD [1], piezoelectric stress is one of the most appealing, as no engineering of the QD membrane structure itself is needed and basically, at least in principle, any kind of membrane can be strained by simply bonding it onto a piezoelectric cell to transfer the stress from the piezo to the membrane. This has been extensively applied to self-assembled quantum dots, allowing the achievement of several results: tuning of the

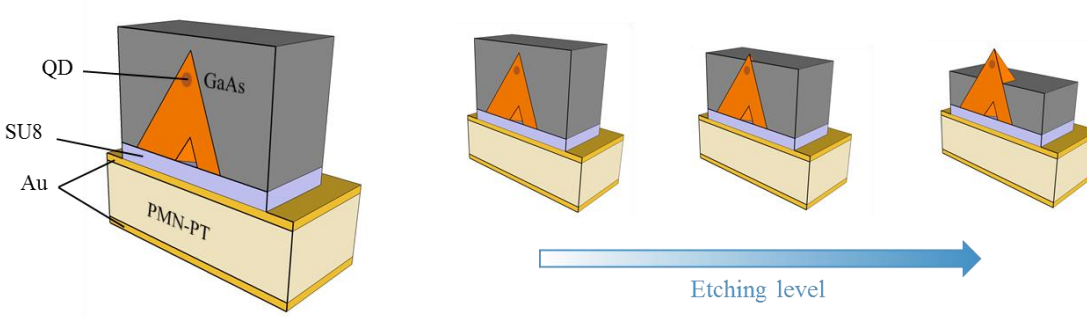


Fig.1: on the left, cross-sectional sketch of a PQD-on-piezoelectric device (showing one single pyramid for simplicity); on the right, different levels of etching leading to different final conditions in terms of pyramidal structure exposure from the original GaAs substrate; the optimal condition for granting both light extraction and strain transfer is the intermediate one.

emission energy in a wide range [2] and also for electrically pumped devices [3], universal recovery of entanglement in QDs affected by FSS by means of the combined application of stress and electric field [4] and by means of the combination of stresses along different directions [5]. The effect of the stress on the QDs bonded onto it depends on the nature of the stress itself: if a purely biaxial stress is applied to the membrane, the only effect will be a renormalization of the effective energy gap of the semiconductor composing the QD, without modifying the symmetry of the system. If an anisotropic biaxial (or uniaxial) stress is applied, instead, together with the shift in emission energy, a change in the FSS and polarization orientation of the non-degenerate excitonic levels is observed [5][6]. In this second case, the extent to which the FSS can be tuned depends on the reciprocal alignment of the anisotropy of the stress and the asymmetry of the QD [4].

8.1.1 Fabrication of piezoelectric tunable PQDs

We followed the procedures adopted e.g. in [6] to bond a QD membrane onto a PMN-PT piezoelectric cell. The choice of this material (rather than a more commonly employed PZT piezoelectric) was due to the high piezoelectricity this material shows.

Also, SU8 was employed as a bonding medium because of its high Young modulus (5kPa) and the possibility of spin-coating a thin (down to 500nm) uniform layer on the piezo substrate to ensure an optimal parallelism between it and the membrane.
Applying this technique to PQDs involves a certain level of extra complexity given by the non-planar nature of the structure[1]. As it was already described in Chapter 2, a different bonding technique from the "classic" Au-Sn reflow had to be employed to fabricate this kind of device. A single-crystal PMN-PT (100)-oriented cell, polished and evaporated on both sides with Cr-Au as electrodes, was spin-coated with SU8-2 and bonded using flip-chip techniques (Fig.1) as outlined in Chapter 2. After the bonding, conventional back-etching is employed. It is necessary to remark that particular care has to be taken in this step. In fact, on one hand the tip of the pyramid has to be exposed from the original substrate in order to allow efficient extraction of light out of the pyramidal structure, on the other, excessive etching levels result in a decreased efficiency of stress transfer onto the PQD, as this won't be surrounded by solid material. An intermediate situation, where the tip is exposed and the QD is still surrounded by GaAs, allows for both the efficient transfer of the strain and the efficient extraction of light from the PQDs (Fig.1).

8.1.2 Tuning of the emission of PQDs

The piezo-bonded sample was introduced into the cryostat for 10K micro-PL measurements. The two sides of the piezo cell were previously contacted (by means of silverpaint) with two insulated cables, led out of the cryostat using a feedthrough. A high-voltage DC power supply was employed to apply up to 1kV across the cell. Before the cooling, the piezoelectric cell needs to be "poled": this operation is performed by slowly (5V per sec) ramping up the applied voltage to about 150V at

[1] The production of this kind of device was done in cooperation with A. Rastelli and R. Trotta (JKU, Linz, Austria and Università La Sapienza, Rome, Italy, respectively), who originally developed the technique.

room temperature, which orients the dipoles inside the piezo along the electric field perpendicularly to the two planar electrodes. This operation is not possible at low temperature, as the dipoles would be more stiff and resist the orienting. Once the dipoles are oriented, applying a further voltage in the same verse results in a tensile strain across the cell (therefore a compressive strain in the plane of the membrane, according to the strain tensor of PMN-PT), while a voltage in the opposite direction with respect to that applied for the poling, results in a compressive vertical strain (therefore an in-plane tensile stress applied to the membrane).

Upon cooldown it was possible to measure a systematic shift of the emission energy in a maximum range of 2meV for each QD. The effect of the stress on the FSS, instead, varied from dot to dot. This reflected the fact that for each PQD the asymmetry is different, while the stress is the same. Only those PQDs for which the orientation of the asymmetry was aligned properly could be tuned. We can see an example of this in Fig.2: the FSS of QD1 could be tuned upon the application of a tensile stress down to a minimum value. The ability of tuning the FSS is already a signature of the anisotropy of the stress applied (anisotropy which takes place because of slight imperfections in the bonding process, as a slight tilt, imperfect mechanical thinning, etc.), but the limit in our tuning capability reflects the misalignment between this anisotropy and the asymmetry of the PQD. If we consider QD3, instead, we can notice that the FSS could be tuned down to almost zero for an applied field of 250V. Cross-correlation measurements allow us to prove that the stress has an effect on the two-photon state emitted through the biexciton-exciton-ground state recombination cascade. Cross-correlations were performed in linear, diagonal, and circular basis, according to the method used e.g. in [7], from which the fidelity to the maximally entangled state was estimated. The restoral of the entanglement upon the application of the stress was proven as fidelity went from below 0.5 (the classical limit) to about 0.75.

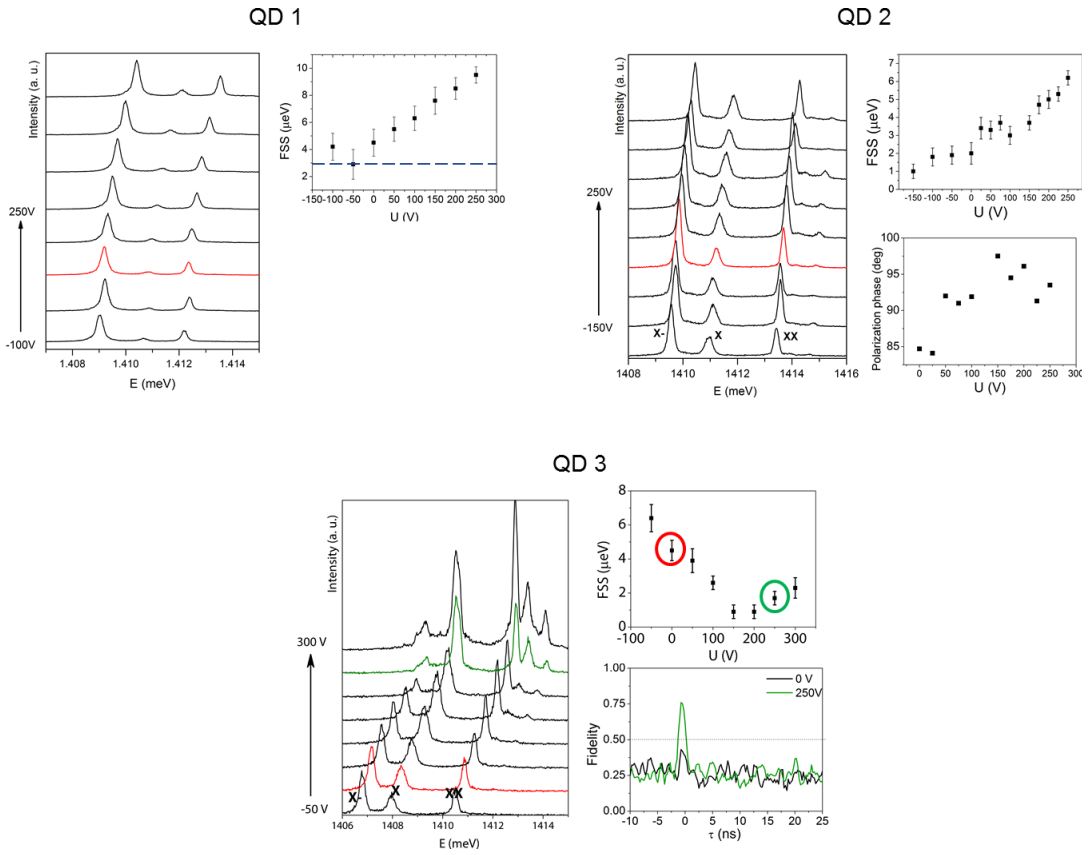


Fig.2: Spectra and result of the tuning of the optical properties for 3 different PQDs; the QDs show a maximum range of tuning of about 2meV; QD1 shows a minimum value for the FSS of about 3μeV; QD2 presents a large range of tuning for the polarization phase, while the FSS minimum reachable value falls out of the maximum applicable bias; QD3 instead shows a minimum value of the FSS that approaches 0, in fact, cross-correlation measurements allowed to estimate that the Fidelity to the expected entangled state is improved from below the classical limit (0.5) to almost 0.75.

8.2. Manipulation and integration of PQDs by “lift-off”

As an alternative to “standard” backetching processes, a liftoff technique was developed which allows a faster processing and a more uniform result and opens the way for new alternatives for integration.

The technique consists in the insertion of an AlAs sacrificial layer before the barrier and QD layer in the structure of the PQD at the epitaxy step. Selective etching of AlAs over GaAs (Fig.3a) and low-Al content AlGaAs can be obtained by chemical etching in Hydrofluoric acid (HF). If the thickness of the AlAs layer and the exposure time to HF are tuned properly, conditions can be achieved for which the pyramidal structure is freestanding but kept in the original growth site by means of van der Waals forces. For instance, an AlAs layer with a nominal thickness of 70nm can be completely etched in 1 min of exposure to HF for PQDs with an inter-pyramidal pitch of 10um. Fig.3b shows one early attempt of this procedure, where a sample with an AlAs sacrificial layer (and AlGaAs barriers) was exposed to HF for minutes: some pyramids are freestanding and dangling freely on the ridge of the patterned area, while some are still inside their growth site.

After the chemical etching, a support for transferring the PQD is needed which can hold the pyramids into place and allow the lift-off in an orderly fashion. Kapton tape is a valid substrate in this sense, as it can be easily applied to the as-etched substrate and subsequently lifted-off retaining typically more than 90% of the pyramids in the central region of the substrate. The advantage of using a few-micron-thick kapton tape is that it can be immediately placed in the cryostat for PL measurements with very good thermal performance in terms of heat transfer. Pyramids on Kapton can be seen in Fig.3d, while Fig.3c shows a typical spectrum of PQDs on Kapton tape cooled down to about 10k.

Different “sticky” substrates can be used to transfer the PQDs, e.g. Polydimethylsiloxane (PDMS), which could be employed as a versatile transferring medium. Remarkably, the lift-off technique is particularly suited to transfer pyramids on the core of an optical fiber.

First attempts were made for transferring PQDs on a multimode fiber. An initial approach involved encapsulating the tip of the fiber in PDMS and placing it perpendicularly to the surface of the HF-exposed substrate: a number of pyramids could be taken up and rested on the core of the fiber, even though the result was quite inhomogeneous. A further attempt instead was performed by means of UV-sensitive glue (Norland 31). In this case the fiber was dipped into the UV sensitive epoxy and again pressed vertically on the substrate; an UV LED (400nm) was shined on the other end of the fiber and allowed the curing of the glue only on its core (Fig.4a). The result is shown in Fig.4b, where an ordered array of pyramids could be

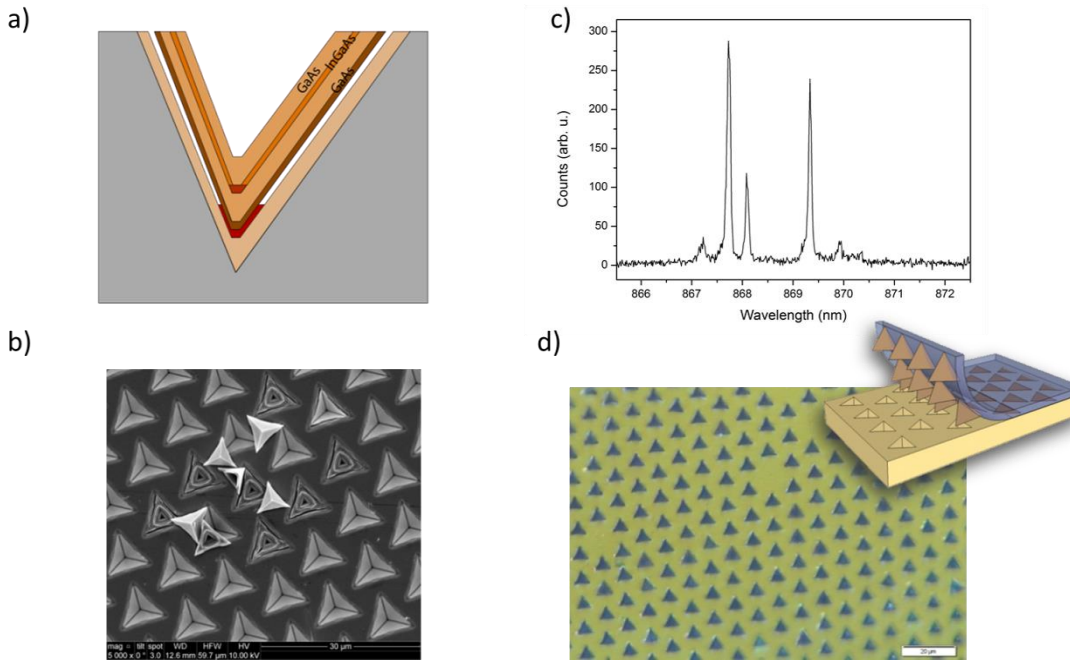


Fig.3: Depiction of the lift-off technique for PQDs: a) schematic representation of the sacrificial AlAs layer and of the effect of HF; b) early attempt of lift-off, where most of the PQDs were released and were lying on the surface of the sample, while some were still kept in the growth site (most probably by means of van der Waals forces); c) PL spectrum of PQDs lifted-off by means of Kapton tape; d) optical image of an array of PQDs after lift-off and schematic representation of the lift-off procedure.

transferred onto the fiber. The end of the fiber with the PQDs was then placed into the cryostat, the other end led out through a vacuum-safe feedthrough. Exciting the PQDs by means of a 45° tilted mirror placed in front of the fiber end inside the cryostat allowed first of all to measure the PL in a confocal configuration (i.e. from the same end that was excited, through the same objective used for excitation, Fig.4c) to ensure that the PQDs could actually be cooled down to the needed temperature of 10k. But most importantly it was possible to measure the light emitted directly through the fiber: although the intensity was about 5 times lower than in a typical confocal configuration (most probably reflecting mode matching issues), it was possible to perform autocorrelation on the X- transition of one of the PQDs, which resulted in single-photon emission signature (Fig.4d). More work in this direction is planned, to address single mode fiber matching etc.

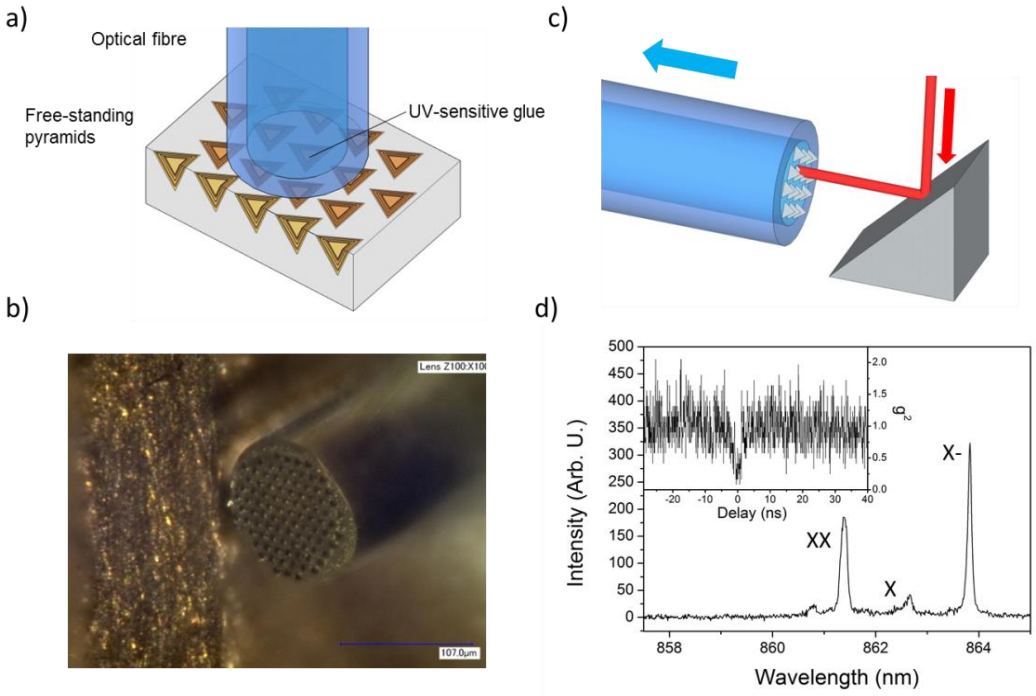


Fig.4: a) schematic representation of the operation of "catching" PQDs on a multimode fiber; b) optical image of an array of PQDs on the core of the multimode fiber, glued by means of UV-sensitive glue; c) schematic representation of the excitation scheme employed to collect the light emitted by the PQDs through the fiber; d) spectrum of one of the PQDs on the multimode fiber (measured through it) and (inset) autocorrelation for the X- (negatively charged exciton) transition, showing the signature of single photon emission.

References

[1] J. D. Plumhof, R. Trotta, A. Rastelli, and O. G. Schmidt, Nanoscale Res. Lett., vol. 7, no. 1, p. 336, 2012.

[2] S. Kumar, R. Trotta, E. Zallo, J. D. Plumhof, P. Atkinson, A. Rastelli, O. G. Schmidt, and) E Zallo, Appl. Phys. Lett. Appl. Phys. Lett, vol. 99, no. 101, 2011.

[3] J. Zhang, F. Ding, E. Zallo, R. Trotta, B. Höfer, L. Han, S. Kumar, Y. Huo, A. Rastelli, and O. G. Schmidt, Nano Lett., vol. 13, no. 12, pp. 5808–13, Jan. 2013.

[4] R. Trotta, E. Zallo, C. Ortix, P. Atkinson, J. D. Plumhof, J. Van Den Brink, A. Rastelli, and O. G. Schmidt, Phys. Rev. Lett., vol. 109, no. 14, p. 147401, Oct. 2012.

[5] R. Trotta, J. Martín-Sánchez, J. S. Wildmann, G. Piredda, M. Reindl, C. Schimpf, E. Zallo, S. Stroj, J. Edlinger, and A. Rastelli, Nat. Commun., vol. 7, p. 10375, Jan. 2016.

[6] J. Martín-Sánchez, R. Trotta, A. Mariscal, R. Serna, G. Piredda, S. Stroj, J. Edlinger, C. Schimpf, J. Aberl, T. Lettner, J. Wildmann, H. Huang, X. Yuan, D. Ziss, J. Stangl, and A. Rastelli, Semicond. Sci. Technol., vol. 33, no. 1, p. 013001, Jan. 2018.

[7] T. H. Chung, G. Juska, S. T. Moroni, A. Pescaglini, A. Gocalinska, and E. Pelucchi, Nat. Photonics, vol. 10, no. 12, pp. 782–787, Oct. 2016.

Conclusion and outlook

This work was based on the study of pyramidal quantum dots (PQDs) as a site-controlled versatile source of quantum light. The MOVPE process employed for the fabrication of this system was investigated from a theoretical point of view, based on a previously developed growth model: the modeling was extended to the simulation of previously not included InGaAs layers over non-planar substrates (specifically V-grooved substrates and substrates patterned with inverted pyramidal recesses), which is the optically active layer in PQDs. After the kinetic parameters were determined by the study of experimental data from the literature, they were used in the same set of reaction-diffusion equations to simulate the epitaxy in the conditions applied in the fabrication of PQDs. The (qualitative) agreement with the experimental data provided new insight in the physical phenomena leading to segregation and profile evolution, allowing the understanding of an odd behavior observed in the optical properties of PQDs. Moreover, SEM analysis allowed moving forward new hypothesis on the actual geometry of the PQD, which might be employed to further develop the current MOVPE model.

A novel LED device based on a real site-controlled system was fabricated. The non-planar nature of the PQDs required further processing engineering of the structure of the PQDs to allow for the selective contacting of the PIN non-planar device, while MOVPE engineering was necessary to form a vertical quantum wire allowing selective carrier injection through the center of the pyramid into the QD itself. Low temperature optical characterization of the devices through cross-correlation of biexciton and exciton transitions showed the emission of polarization entangled photon pairs from more than one PQD in a small region of the sample. Importantly, the quality of the entanglement after post processing time-window selection techniques was high, enough to prove the violation of Bell inequalities and therefore

prove the actual quantum nature of the emitted radiation. Single photon emission was also studied upon electrical injection. Although technical limitations, among which impedance mismatch, didn't allow a quick carrier population relaxation time, a time-gating technique was employed to obtain a single photon emission with a $g^2(0)$ as low as 0.088. The comparison between this time-gating technique and the time-window selection previously employed to filter entangled photon pairs from the same device provided previously unreported insight about the methods for filtering a "good" single photon emission and a "good" entangled photon emission. PQD-based LED therefore are a promising candidate as an integrable on-demand electrically driven source of non-classical light, given the necessity of performance improvement especially for what concerns the electrically injected pulse itself.

Stacked PQDs in a pyramidal recess were studied as possible candidates for the formation of QD-molecule-like structures. An extensive statistical study was carried out to characterize double PQDs with different QD-separation. A clear trend was observed in the emission energy and the biexciton binding energy, but most importantly in the change in behavior from 2 independent QD-like to a single QD-like, denoting a certain form of coupling between the QD pair. More-than-two QDs systems were characterized as well, resulting in further red-shifting of the emission together with more complex transitions signature compared to single or double QDs. Interestingly, the optical behavior of these multiple-QD structures changed as the number of QDs were augmented, showing an increasingly vertically polarized spectrum. Also, placing QDs at a certain distance inside the pyramid, resulted in a change in the "charging" character of the single QDs in the ensemble, importantly allowing to systematically obtain more positively charged QDs and better linewidths. Finally our attention concentrated on the case of double QDs with vanishing biexciton binding energy, which were featuring the emission of "twin" photons from the biexciton-exciton-ground state cascade, revealed by a characteristic cross-correlation behavior. The multiple-QD system will require further study on a theoretical level to

fully understand the physical reason behind the change in the spectral properties, but also to be employed in practical application, e.g. the generation of quantum cluster states.

Further improvements of the PQDs were put into practice although still at an early stage. PQDs were bonded onto monolithic piezoelectric devices which allowed the application of a stress to the PQD structure, therefore tuning the optical properties. Upon the application of an anisotropic biaxial stress, both the emission energy and the fine structure splitting (affecting the quality of entangled photon emission) could be tuned in a range of 2 meV and a few μeV respectively, the second range notably allowing tuning FSS down to vanishing values and restoring therefore entangled photon emission. This paves the way for the realization of more complex strategies for the full independent control of all the optical properties of PQDs: emission energy, polarization orientation and FSS magnitude, to perform universal restoral of entangled photon emission for every PQD, as it was reported recently by applying 3 independent stresses to self-assembled QDs.

Finally, a new processing technique was developed to “lift-off” the whole pyramidal structure from the original growth site and to allow its manipulation on supportive or functional substrates. Besides the possibility of quickly processing samples using this technique and immediately characterizing the PQDs (differently from the “classical” backetching processing), this allowed to easily transfer the PQDs onto a multimode optical fiber by means of UV-sensitive glue. Single-photon emission signature was observed by performing the auto-correlation of photons directly coupled to the fiber. Certainly, fabrication strategies need to be further developed to realize integration of PQDs onto functional substrates, such as integrated waveguides and optical circuits.

In conclusion the fabrication of PQDs has been studied and developed, leading to the production of electrically injected PQDs, stacked PQDs and piezoelectric-based tunable PQDs devices. In the future, resonant or quasi-resonant pumping techniques will be employed in order to improve the optical properties upon optical excitation to

improve the limiting factors of this non-classical light source as well as to advance in our physical understanding of the PQD system. This, together with the extremely interesting possibilities offered by the PQDs in terms of site-control and integrability demonstrated e.g. by the unique possibility of transferring ordered arrays of PQDs onto different substrates, will most likely make PQDs one of the few promising quantum light sources for a technological development for the field of quantum information.

Acknowledgements

I would like to thank sincerely everyone I met on my journey through my PhD in Ireland. First of all my parents and my family for believing in me and allowing for whatever choice I ever made, even if it took me far away, and my girlfriend Andrea for greatly supporting me in the last year.

I am infinitely grateful to Dr. Emanuele Pelucchi for allowing all this to happen and for the immense work he has done in guiding and helping me, but also for his example of passion for physics and science, which is of exceptional inspiration for many. Thanks to Dr. Gediminas Juska for teaching me most of what I learnt during these years, for the massive amount of time he dedicated to me and for his patience and support.

Among my group mates, with whom I shared frustration and success, I would like to thank particularly Enrica Mura and Dr. Tung-Hsun Chung (Mau) for being not only valid and caring colleagues but also great friends. I thank Dr. Agnieszka Gocalinska and Dr. Kevin Thomas for the assistance and time dedicated to me. I would like also to acknowledge all the help and good memories from colleagues who are not in Tyndall anymore: Eoin Murray, Francesco Azzarello, Dr. Andrea Pescaglini and Dr. Eleonora Secco.

I wish good luck to the new people in the group who – I'm sure – will do an amazing job in carrying on the research: Simone Varo and Iman Ranjbar. Thank you for sharing the last year of my time in Tyndall.

I am thankful for all the people I met in Tyndall who were of great help and assistance even outside the EPN group, in particular Dr. Aidan Quinn and Prof. Eoin O'Reilly for the guidance through the years, but also everyone who provided essential insight for the fabrication, especially Krimo for the help in the Training Fab.

Finally I would like to thank the huge amount of friends in Cork who, in a way or another has been supporting me over the years.